Magnetic and magnetoelastic properties of M-substituted cobalt ferrites (M=Mn, Cr, Ga, Ge)

by

Sang-Hoon Song

A dissertation submitted to the graduate faculty

in partial fulfillment of the requirements for the degree of

DOCTOR OF PHILOSOPHY

Major: Materials Science and Engineering

Program of Study Committee:
David C. Jiles, Major Professor
Nicola Bowler
Vitalij K. Pecharsky
Bruce R. Thompson
Robert J. Weber

Iowa State University

Ames, Iowa

2007

ProQuest Information and Learning Company
300 North Zeeb Road
P.O. Box 1346
Ann Arbor, MI 48106-1346

TABLE OF CONTENTS

ABSTRACT

Magnetic and magnetoelastic properties of a series of M-substituted cobalt ferrites, $CoM_xFe_{2-x}O_4$ (M=Mn, Cr, Ga; x=0.0 to 0.8) and Ge-substituted cobalt ferrites $Co_{1+x}Ge_xFe_{2-2x}O_4$ (x=0.0 to 0.6) have been investigated. The Curie temperature T_C and hysteresis properties were found to vary with substitution content x, which indicates that exchange and anisotropy energies changed as a result of substitution of those cations for Fe. The maximum magnitude of magnetostriction decreased monotonically with increase in substitution contents x over the range x=0.0 to 0.8. However, the rate in change of magnetostriction with applied magnetic field ($d\lambda/dH$) showed a maximum value of 5.7×10^{-9} $A^{-1}m$ at x = 0.1 Ge sample, which is the highest value among recently reported cobalt ferrite based materials. The slope of magnetostriction with applied field $d\lambda/dH$ is one of the most important properties for stress sensor applications because it determines the sensitivity of magnetic induction to stress ($dB/d\sigma$). The results of Ga- and Ge-substituted cobalt ferrite were compared with those of Mn- and Cr-substituted cobalt ferrites, and it was found that the effect of the substituted contents x on magnetic and magnetoelastic properties was dependent on the ionic distribution between two possible interstice sites within the spinel structure: Mn^{3+} and Cr^{3+} prefer the octahedral sites, whereas Ga^{3+} and Ge^{4+} prefer the tetrahedral sites. Temperature dependence of the absolute magnitude of the magnetic anisotropy constant $|K_1|$ of Ga-substituted cobalt ferrites $CoGa_xFe_{2-x}O_4$ (x=0.0 to 0.8) was investigated based on the law of approach to saturation and the results were compared with those of magnetostriction measured at the same temperatures. Based on the results, it was considered that there was a change in sign of K_1 around 200 K for Ga-substituted cobalt ferrites. Comparison of the results between Ga- and Ge-substituted cobalt ferrites showed that substitution of Ge^{4+} ions for Fe made more pronounced effects on magnetic and magnetoelastic properties at room temperature than that of Ga^{3+} ions. Especially the enhanced value in $d\lambda/dH$ by Ge-substitution suggests that adjusting Ge content substituted into cobalt ferrite can be a promising route for controlling critical magnetic properties of the material for practical sensor applications.

INTRODUCTION

In this study, the magnetic and magnetoelastic properties of some partially substituted cobalt ferrite materials ($CoMn_xFe_{2-x}O_4$, $CoCr_xFe_{2-x}O_4$, $CoGa_xFe_{2-x}O_4$, $Co_{1+x}Ge_xFe_{2-2x}O_4$; $x = 0.0 - 0.8$) have been investigated. The main objective of this study was to increase the sensitivity of magnetostriction to applied magnetic field ($d\lambda/dH$), which is a critical issue in magnetomechanical sensor applications, and eventually to understand the mechanisms of how the magnetoelastic behaviors are inter-related with magnetic exchange interaction and magnetic anisotropy, both of which are expected to be adjusted by the substitutions of some cations in the cobalt ferrite based materials.

The crystal structure of cobalt ferrite is cubic spinel structure, whose unit cell contains 8 Co^{2+}, 16 Fe^{3+}, and 32 O^{2-} ions, the chemical formula being $CoFe_2O_4$. The oxygen ions form close-packed face centered cubic structure, which makes 64 tetrahedral and 32 octahedral lattice sites per unit cell. Co and Fe ions may occupy one of these two kinds of lattice sites and the magnetic properties vary with the distribution of cations. Especially, compared with other type of ferrite materials, high magnitudes of magnetic anisotropy and magnetostriction observed for cobalt ferrite were known to be caused by the Co^{2+} ions located in the octahedral sites (Table I and II) [1]. With respect to this, substitution of some cations for Co or Fe ions in the cobalt ferrite spinel structure was expected to show some interesting change in magnetic properties depending on the composition because both the magnetic exchange interaction and the anisotropy should be changed by cation substitution. For exchange interaction, which originates from the indirect coupling through oxygen ions in spinel structure, according to the Heisenberg exchange interaction energy (see section 2.1.1) the magnitude and sign are determined by the magnetic moments of the cations and their relative distance and angle, all of which can be adjusted by cation substitution. For magnetic anisotropy, which is determined by orbital magnetic moments, and their interactions with spin magnetic moments (spin-orbit coupling) and lattice (orbit-lattice interaction), ionic distribution in the lattice should be a major factor that determines the anisotropy. Therefore the magnetoelastic properties, which should be closely inter-related with exchange interaction and magnetic anisotropy, are also expected to change as a result of cation substitution.

Substitution of transition elements for Fe^{3+} ions in magnetite (Fe_3O_4) has been tried for a long time. Barth and Posniak [2] first proposed the inverse spinel structure in ferrites in 1932, in which half of the trivalent ions occupy the tetrahedral sites and the remaining trivalent ions plus the divalent ions occupy the octahedral sites whereas all the trivalent ions occupy octahedral sites in normal spinel structure. Since then the magnetic structures of various ferrites have been discovered; Zn and Cd ferrites were identified to have normal spinel structure, whereas Mn, Fe, Co, Mg, Cu, and Ni ferrites have inverse spinel structure [3]. Developments in various techniques, such as neutron diffraction and ferromagnetic resonance spectroscopy, have made it possible to measure various physical properties for each ferrite. It has been found that cobalt ferrite has high magnetic anisotropy and magnetostriction compared with other types of ferrites (Table I and II). However, cobalt ferrite did not receive much attention in the early days of ferrites applications because magnetostriction was found to have adverse effects on the normal functions of ferrites when they were used for transformers or inductors, which were the major applications of ferrites at that time. So the earlier research on ferrites was usually directed towards on developing materials with high permeability and therefore low magnetostriction.

Table I. Magnetic anisotropy constants K_1 and K_2 for selected materials [1].

	(T=4.2 K)		(RT)	
	K_1	K_2	K_1	K_2
3d Metals				
Fe	5.2×10^{5}	-1.8×10^{5}	4.8×10^{5}	-1.0×10^{5}
Co^u	7.0×10^{6}	1.8×10^{6}	4.1×10^{6}	1.5×10^{6}
Ni	-12×10^{5}	3.0×10^{5}	-4.5×10^{4}	-2.3×10^{4}
$Ni_{80}Fe_{20}$			-3×10^{3}	
$Fe_{50}Co_{50}$			[b]-1.5×10^{5}	
4f Metals				
Gd^u	-1.2×10^{6}	8.0×10^{5}	1.3×10^{5}	
Tb^u	-5.65×10^{8}	-4.6×10^{7}		
Dy^u	-5.5×10^{8}	-5.4×10^{7}		
Er^u	1.2×10^{8}	-3.9×10^{7}		
Spinel Ferrites				
Fe_3O_4	-2×10^{5}		-0.9×10^{5}	
$NiFe_2O_4$	-1.2×10^{5}		-0.7×10^{5}	
$MnFe_2O_4$	$\approx -4\times10^{5}$	$\approx -3\times10^{5}$	-3×10^{4}	
$CoFe_2O_4$	10^{7}		2.6×10^{6}	
Garnets				
YIG	-2.5×10^{4}		1×10^{4}	
GdIG	-2.3×10^{5}			
Hard Magnets				
$BaO_6\cdot Fe_2O_3{}^u$	4.4×10^{6}		3.2×10^{6}	
Sm^uCo_5	7×10^{7}		$1.1\text{-}2.0\times10^{8}$	
Nd^uCo_5	-4.0×10^{8}		1.5×10^{8}	
$Fe_{14}Nd_2B^u$	-1.25×10^{8}[c]		5×10^{7}	
$Sm_2Co_{17}{}^u$			3.2×10^{7}	
$TbFe_2$			-7.6×10^{7}	

[a] Uniaxial materials are designated with a superscript u and their values K_{u1} and K_{u2} are listed under K_1 and K_2 respectively.

[b] Disordered; $K_1 \approx 0$ for ordered phase

[c] Net moment canted about 30° from [001] toward [110]

Table II. Magnetostriction constants λ_{100} and λ_{111} ($\times 10^{6}$) for selected materials [1].

	T=4.2 K		Room Temperature		
	$\lambda_{100}(\lambda^{\gamma,2})$	$\lambda_{111}(\lambda^{\varepsilon,2})$	$\lambda_{100}(\lambda^{\gamma,2})$	$\lambda_{111}(\lambda^{\varepsilon,2})$	Polycrystalλ_S
			3d Metals		
BCC-Fe	26	-30	21	-21	-7
HCP-Co^{u}	^{b}-150	^{b}45	^{b}-140	^{b}50	^{b}-62
FCC-Ni	-60	-35	-46	-24	-34
BCC-FeCo			140	30	
$^{a}Fe_{80}B_{20}$	48				32
$^{a}Fe_{40}Ni_{40}B_{20}$					14
$^{a}Co_{80}B_{20}$					-4
			4f Metals/Alloys		
Gd^{u}	^{b}-175	^{b}105	^{b}-10	0	
Tb^{u}		b8700		b30	
$TbFe_2$		4400		2600	1753
$Tb_{0.3}Dy_{0.7}Fe_2$				1600	1200
			Spinel Ferrites		
Fe_3O_4	0	50	-15	56	40
$MnFe_2O_4$^{u}			^{b}-54	^{b}10	
$CoFe_2O_4$			-670	120	-110
			Garnets		
YIG	-0.6	-2.5	-1.4	-1.6	-2
			Hard Magnets		
$Fe_{14}Nd_2B$^{u}					
$BaO_6 \cdot Fe_3O_4$^{u}			^{b}13		

[a]Some polycrystalline room-temperature values are also listed. The prefix [a] designates an amorphous material. [b]For uniaxial materials (superscript u) where $\lambda_{100}(\lambda^{\gamma,2})$ or $\lambda_{111}(\lambda^{\varepsilon,2})$ was reported.

In the early 1970's, rare earth based giant magnetostrictive materials, such as $SmFe_2$, $TbFe_2$, $DyFe_2$, were developed (λ_S= ~2000 ppm) and these highly magnetostrictive materials were considered for various applications, such as actuators and sensors [4]. For the sensor applications, however, it was found that their high magnetic anisotropy ($K > 10^6$ J/m^3) caused low sensitivity to stress which restricted their usage in magnetomechanical sensor applications. With respect to this, one of the major concerns with rare earth based magnetostrictive materials was reducing the magnetic anisotropy. A major technological breakthrough was achieved by a development of Terfenol-D ($Tb_{0.3}Fe_{0.7}Fe_2$) material which has low magnetocrystalline anisotropy combined with high magnetostriction. However, low anisotropy with high magnetostriction could be obtained in the samples fabricated by directional solidification along <112> direction, which required a high cost fabrication process. The easy axes of Terfenol-D are <111> directions, however, directional solidification along <111> directions has not been successful. In addition, oxidation of rare earth alloys was problematic for applications. For these reasons, finding substitutes for this material has recently been carried out and several promising results have been reported on cobalt ferrite based materials [5-10]

Cobalt ferrite based composites have high magnetostriction λ, high sensitivity of magnetic induction to applied stress $dB/d\sigma$, are chemically very stable and generally of low cost. These factors make these materials attractive for use in magnetoelastic sensors [5, 6]. Chen *et al* have recently reported the superiority in sensitivity of magnetostriction to applied magnetic field ($d\lambda/dH$) of cobalt ferrite composite over Terfenol-D composite (Fig.1.). However, to enable practical applications a family of materials was needed, in which the magnetoelastic response, magnetic properties, and their temperature dependences could be tailored by a well defined "control variable" such as chemical composition or ionic distribution between tetrahedral and octahedral sites. When it comes to the ionic distribution, Fig.2 summarizes the calculated and observed site preference energies for various cations in some binary spinel ferrites [11]. However, the preference of each cation between tetrahedral and octahedral sites are not easy to predict because there are various factors involved in site selection, such as cation size, crystalline electric field, valence, etc. Moreover, it has been reported that the order of site preference determined based on the results of binary spinels was not applicable to ternary or higher cation spinels [12]. Regarding this aspect, it therefore becomes an interesting subject to investigate how the site preference changes from binary to ternary spinel ferrites.

Based on data shown in Fig. 2, a series of Mn-and Cr-substituted cobalt ferrite $CoMn_xFe_{2-x}O_4$, $CoCr_xFe_{2-x}O_4$, (where x=0.0 to 0.8) samples were recently studied to investigate the effect of their octahedral site occupancy on the magnetic and magnetoelastic properties [7-10]. The results showed that substitution of Mn or Cr for Fe in cobalt ferrite reduced the Curie temperature, and that the effect was more pronounced for Cr than Mn. Substitution of either element caused the maximum magnetostriction to decrease and the rate of change was higher in Cr-series. The maximum strain derivative $(d\lambda/dH)_{max}$, however, was higher for both series than that for pure cobalt ferrite. From the results of Mössbauer spectroscopy measurements it was interpreted that Cr has an even stronger octahedral site preference than Mn, which caused more of the Co ions to be forced to occupy tetrahedral sites [8, 10].

In the present study, a family of Ga- and Ge-substituted cobalt ferrite $CoGa_xFe_{2-x}O_4$ (where x=0.2 to 0.8), $Co_{1+x}Ge_xFe_{2-2x}O_4$ (where x=0.1 to 0.6) samples have been investigated. Ga^{3+} and Ge^{4+} were expected to prefer the tetrahedral sites [11, 12]. Therefore the results were expected to be different from those of Mn- and Cr-substituted cobalt ferrites. Systematic measurements of magnetic and magnetoelastic properties for each composition were performed under various conditions and the results were compared with those of Mn- and Cr-substituted cobalt ferrites. More significant changes in magnetic and magnetoelastic properties caused by Ga- and Ge-substitutions were observed than those by Mn- or Cr-substitutions, which was analyzed in terms of the change in anisotropy and exchange energy.

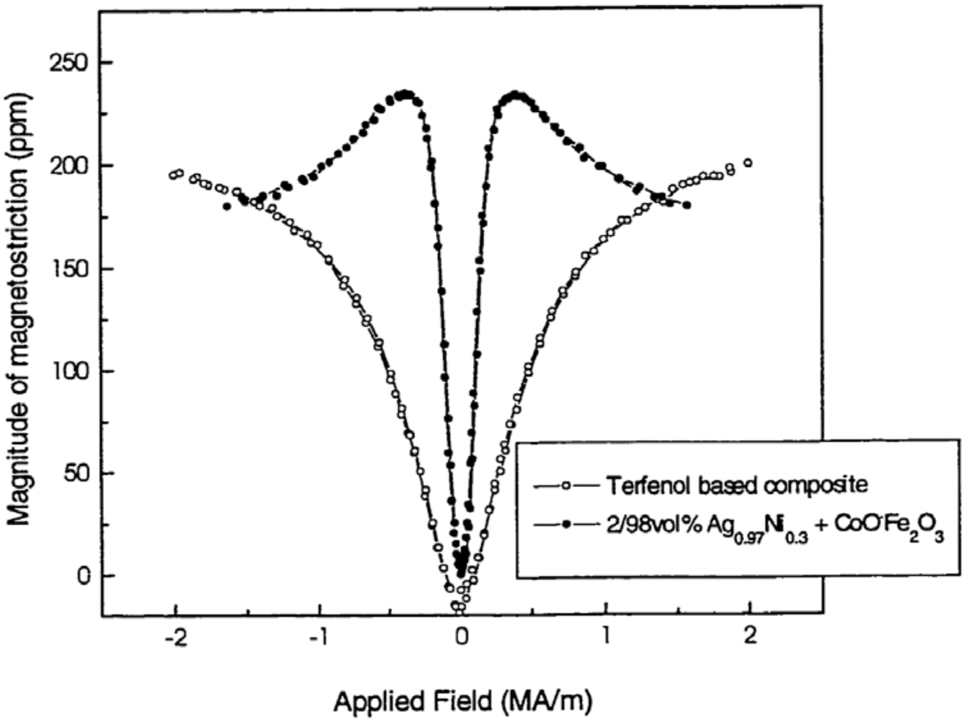

Fig. 1. Comparison of magnetostrictions of Co-ferrite composite and Terfenol composite [5].

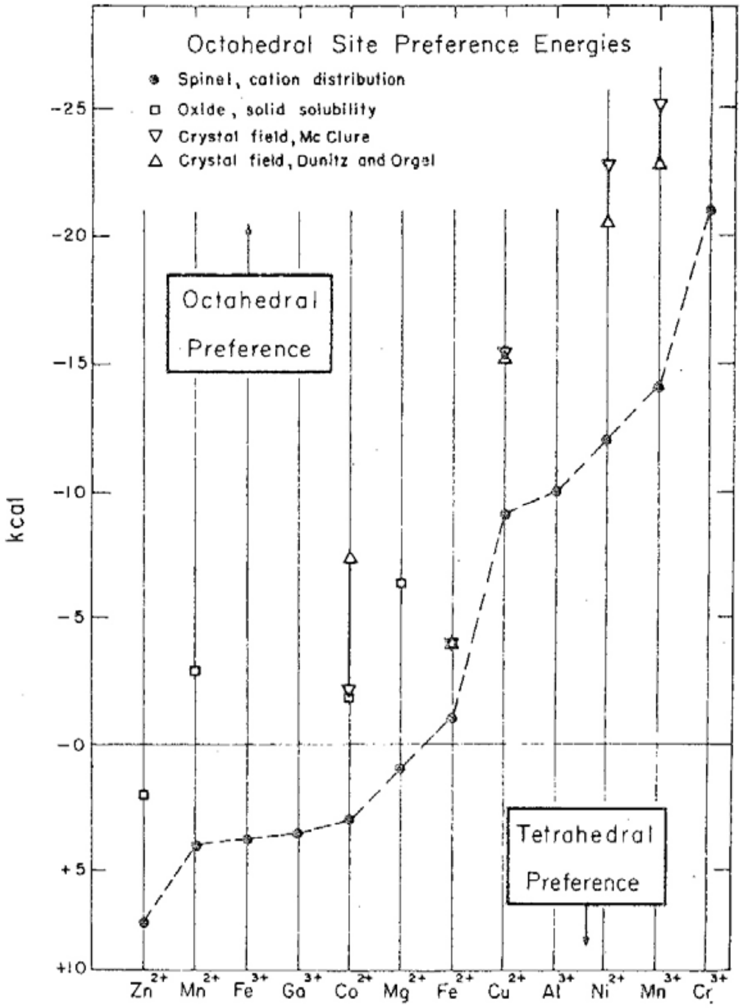

Fig. 2. Empirical site preference energies for some divalent and trivalent ions in the spinel structure [11].

2. BACKGROUND

2.1 Fundamentals of magnetism

2.1.1 Ordered magnetic structures

Just like periodicity in arrangement of atoms constituting a crystal structure, there can be ordering of magnetic moments to make a magnetic structure. Common forms of magnetic ordering include ferromagnetism, ferrimagnetism, antiferromagnetism and helimagnetism. The fundamental cause of order in magnetic structures is exchange interaction among magnetic moments, which tends to maintain the ordering against the thermal disturbance. Thus at the magnetic phase the material undergoes a transition at a critical temperature above which the ordering in magnetic moments is broken so that the material becomes paramagnetic. It is well known that the exchange interaction varies with distance between magnetic moments, therefore the atomic arrangements of magnetic elements in a crystal structure are closely related with the alignment of magnetic moments. With respect to this, the periodic unit in a magnetic structure is sometimes called the "magnetic lattice". The Heisenberg exchange interaction energy [14] is generally used to describe the magnetic ordering among magnetic moments within a domain, in which the first nearest neighbor exchange energy of a magnetic element, i, interacting with its j nearest neighbors is given by,

$$\mathrm{E}_{\mathrm{ex}} = -2\gamma_{\mathrm{NN}} \sum_{\mathrm{i,j}} \mathrm{J}_{\mathrm{i}} \cdot \mathrm{J}_{\mathrm{j}} \tag{1}$$

where γ_{NN} is the exchange interaction coefficient between nearest neighbors, and J_i, J_j are total angular momentum at ith and jth sites.

When the exchange interaction constant γ_{NN} is positive the magnetic moments tend to align parallel, thus the material shows ferromagnetic ordering. On the other hand, when γ_{NN} is negative, the magnetic moments align antiparallel to each other so that the material shows antiferromagnetic $\left(\sum m = 0\right)$ or ferrimagnetic ordering $\left(\sum m > 0\right)$.

Some kinds of materials show helimagnetism in which the magnetic moments within the same plane align parallel within the plane, however, those in successive planes align at an inclined angle.

2.1.2 Molecular field theory

In 1905 Langevin [15] developed a theory of paramagnetism by using statistical thermodynamics to explain the magnetic behavior. In this theory he treated the magnetic response of independent molecular magnets to a magnetic field following the Maxwell-Boltzmann statistics, however, the calculated classical magnetostatic field was too weak to explain the magnetic ordering, from which he concluded that there must be another strong magnetic interaction among magnetic elements. This idea was formulated by Weiss [16] when he introduced the concept of a large “molecular field” to describe the temperature dependence of magnetic saturation below Curie temperature. In this so called “Weiss molecular field theory”, he extended the Langevin theory of paramagetism by adding the strong internal coupling field acting on the site of one magnetic moment produced by the interaction with its the neighboring moments, so that the cooperative behavior of magnetic moments resisting the thermal fluctuation effect could be explained. Later, the nature of this internal field was treated in a microscopic way and identified by Heisenberg to be due to the quantum mechanical pairwise interaction between spins on different sites.

2.1.3 Langevin and Brillouin functions

The magnetic potential energy U of an atomic magnetic moment m is

$$\mathrm{U} = -\mu_0 \mathrm{mH}\cos\theta \tag{2}$$

where θ is the angle between the magnetic moment ($\overline{\mathrm{m}}$) and applied magnetic field ($\overline{\mathrm{H}}$). By applying the Maxwell-Boltzmann distribution function the number (N_θ) of atomic moments pointing inclined θ angle with respect to magnetic field can be expressed as

$$N_\theta = N\frac{\exp^{-\mu_0 mH\cos\theta/kT}}{\sum_\theta \exp^{-\mu_0 mH\cos\theta/kT}} \tag{3}$$

where N is the total number of atomic moments.

Then the total magnetization (M) along the field direction can be given by

$$\begin{aligned} M &= \sum_\theta m\cos\theta\cdot N\frac{\exp^{-\mu_0 mH\cos\theta/kT}}{\sum_\theta \exp^{-\mu_0 mH\cos\theta/kT}} \\ &= N\frac{\sum_\theta m\cos\theta\exp^{-\mu_0 mH\cos\theta/kT}}{\sum_\theta \exp^{-\mu_0 mH\cos\theta/kT}} \\ &= N\frac{\int m\cos\theta\left[\exp^{-\mu_0 mH\cos\theta/kT}\right]d\Omega}{\int \exp^{-\mu_0 mH\cos\theta/kT}\,d\Omega} \end{aligned} \tag{4}$$

where dΩ=sinθdθdφ.

By substituting $s=-\mu_0 mH/k_BT$ and x=cosθ the equation (4) becomes

$$\begin{aligned} M &= Nm\frac{\int_{-1}^{1}\exp^{sx}\,x\,dx}{\int_{-1}^{1}\exp^{sx}\,dx} \\ &= Nm\frac{\partial}{\partial s}\ln\left[\int_{-1}^{1}\exp^{sx}\,dx\right] \\ &= Nm\frac{\partial}{\partial s}\ln\left[\frac{e^{s}-e^{-s}}{s}\right] \\ &= Nm\left(\frac{e^{s}+e^{-s}}{e^{s}-e^{-s}}-\frac{1}{s}\right) \\ &= Nm\left(\coth s-\frac{1}{s}\right)=NmL(s) \end{aligned} \tag{5}$$

The actual magnetic moment m can be determined from the total angular momentum of the isolated atom which should be obtained by vector sum of the orbital and spin angular momenta of electrons given by,

$$m = g\sqrt{J(J+1)}\,\mu_B \tag{6}$$

where μ_B is the Bohr magneton and g is the Landé-splitting factor which is equal to

$$g = 1+\frac{J(J+1)+S(S+1)-L(L+1)}{2J(J+1)} \tag{7}$$

in which S, L, J are the spin, orbital, and total angular moment quantum numbers respectively.

If this quantized component of magnetic moment in the field direction $m=gJ\mu_B$ replaces the classical term mcosθ, then the total magnetization along the field direction can be derived by summations of magnetic moments over discrete angles (–J … +J). The resultant expression for the total magnetization is the so called Brillouin function [17] which is given by,

$$M = NgJ\mu_B B_J\left(\frac{gJ\mu_B\mu_0 H}{k_B T}\right)$$

where (8)

$$B_J(x) = \left(\frac{2J+1}{2J}\right)\coth\left[\frac{(2J+1)x}{2J}\right] - \left(\frac{1}{2J}\right)\coth\left(\frac{x}{2J}\right)$$

Using this equation the temperature dependence of spontaneous magnetization within a domain can be calculated. Substituting the Weiss molecular field $H_{app}+\alpha M$ (where H_{app} and α are the applied magnetic field and the molecular field coefficient respectively) for the effective magnetic field H and applying high temperature limitation ($x \ll 1$) results in the famous Curie-Weiss law;

$$\text{when } x \langle\langle 1 \quad \text{where} \quad x = \frac{gJ\mu_B\mu_0(H+\alpha M)}{k_B T}$$

$$\coth x \approx \frac{1}{x} + \frac{x}{3} \qquad (9)$$

therefore,

$$\begin{aligned} M &= NgJ\mu_B\left[\left(\frac{2J+1}{2J}\right)\left\{\frac{2J}{(2J+1)x} + \frac{(2J+1)x}{6J}\right\} - \frac{1}{2J}\left\{\frac{2J}{x} + \frac{x}{6J}\right\}\right] \\ &= NgJ\mu_B\left[\frac{J(J+1)}{3J^2}x\right] \\ &= \frac{Ng^2 J(J+1)\mu_B^2\mu_0(H+\alpha M)}{3k_B T} \end{aligned}$$

$$\chi = \frac{M}{H} = \frac{N\mu_0 g^2\mu_B^2 J(J+1)}{3k_B T - \alpha N\mu_0 g^2\mu_B^2 J(J+1)} \qquad (10)$$

$$\text{where} \quad T_C = \frac{\alpha N\mu_0 g^2\mu_B^2 J(J+1)}{3k_B T}$$

2.1.4 Curie temperature determination

In practice, in order to determine the ordering temperature at which spontaneous magnetization occurs, it is necessary to make the sample single domain and to align all magnetic moments along the applied field during the measurement. This sometimes requires huge fields and the saturation magnetization does not vanish just above the ordering temperature due to the short-range ordering of the moments. One of the simplest methods to determine Curie temperature T_C from the magnetization vs temperature curve is linear extrapolation from the region of maximum slope (usually this region corresponds to the inflection point of the magnetization curve) down to the temperature axis. This is appropriate for soft magnets with low anisotropy field H_k. When it comes to hard magnets with high anisotropy field, however, high magnitude of applied magnetic field may influence the shape of M vs T curve especially in the vicinity of the Curie temperature, and that, in some cases, it is impossible to saturate the sample. In these cases, it would be useful if we can identify the location of T_C from the magnetization curve M(H, T) even in very weak applied magnetic field. With respect to this, the method of “Arrott plots” [18] is one of the most frequently used methods satisfying these conditions.

2.1.4.1 Arrott plots

Under assumption that M is very small, the magnetic contribution to the free energy in the presence of a magnetic field H can be expressed by the Landau expansion,

$$G(M) = \frac{a}{2}M^2 + \frac{b}{4}M^4 + \cdots - \mu_0 MH \tag{11}$$

where a and b are positive functions of temperature.

The equilibrium magnetization can be given by the free energy minimum condition as follows,

$$\frac{dG(M)}{dM} = aM + bM^3 + \cdots - \mu_0 H = 0 \tag{12}$$

By neglecting the higher orders terms in M the equation is simplified to be

$$M^2 = \frac{\mu_0}{b}\frac{H}{M} - \frac{a}{b} \tag{13}$$

For local moments, the coefficient a is given by

$$a = \frac{\mu_0}{C}(T - T_C), \tag{14}$$

whereas for itinerant magnets, it can be expressed as

$$a \propto T^2 - T_C^2. \tag{15}$$

Therefore the equation (13) can be written as

$$M^2 = -C(T^n - T_C^n) + \frac{\mu_0}{b}\frac{H}{M} \tag{16}$$

where C is a constant and n=1 for local moments and 2 for itinerant magnets [1].

Based on this equation, various plots of M^2 versus H/M can be made using experimental data giving straight lines obtained at various temperatures. Among these plots one specific line for $T=T_C$ should intercept the axes at $M^2=0$.

Even though the method of “Arrott plots” is one of the most frequently used methods in determining Curie temperature, there still remains a uncertainty in the validity of the use of Landau expansion applying for various kinds of magnetic materials. There is also a question over the applicability of the mean field (“Weiss molecular field”) approach, which can work well in specific cases but is not completely general in its validity.

2.1.5 Exchange interaction and molecular field theory

Magnetic “domain” is a volume within which there exists a directional alignment of magnetic moments parallel (ferromagnetism), antiparallel (antiferromagnetism or ferrimagnetism), or with a specific angle (helimagnetism). The fundamental reason for this directional alignment is the exchange interaction among magnetic moments, which is difficult to explain in terms of classical physics. When it comes to the empirical treatment of exchange interaction, one of the methods to measure the strength of the exchange interaction is the analysis of temperature dependence of the saturation magnetization or the Curie temperature. Qualitatively, it seems obvious that ordering temperature is indicative of a measure of the strength of the exchange interaction. For quantitative analysis, however, various variables need to be considered such as the range of exchange interaction on each magnetic moment. A number of approximations have been suggested for this purpose [19-23], however, the basic concept is based on the “Heisenberg model”, of which exchange interaction energy can be interrelated with empirically measurable quantities, such as magnetization or Curie temperature T_C as follows,

$$E^{i}_{ex} = -2\gamma_{i,j}\sum_{j} J_i \cdot J_j = -2\mu_0 H^{i}_{eff} \cdot m_i = 3k_B T_C \text{ (for isotropic materials)} \quad (17)$$

; $\gamma_{i,j}$ = the exchange interaction constant between magnetic moments in i and j sites

J_i, J_j = total angular momentum at i and j sites respectively

H_{eff}^{i} = molecular field acting on the magnetic moment at i site

k_B=Boltzmann constant.

2.1.6 Magnetic anisotropy

The magnetic anisotropy represents the preference of the magnetic moments to lie in a particular direction in a sample. In other words, the total magnetic energy of a material at equilibrium state is a function of direction. There are various possible origins to cause the magnetization to have directional preference, such as sample shape, crystal symmetry, stress, or directed atomic pair ordering. Sometimes magnetic anisotropy can be classified variously as shape anisotropy, magnetocrystalline anisotropy, stress anisotropy, or induced anisotropy based on these physical origins. Of these, only magnetocrystalline anisotropy is an intrinsic property of the material.

2.1.6.1 Magnetic anisotropy energy

Akulov [24] showed that the dependence of internal energy on the direction of spontaneous magnetization can be expressed in terms of an expansion involving even powers of direction cosines of magnetization relative to the crystal axes.

For the simplest case of uniaxial magnetic anisotropy, the internal energy can be expressed by expanding in a series of powers of $\sin^2\theta$:

$$E_a = K_{u1}\sin^2\theta + K_{u2}\sin^4\theta + K_{u3}\sin^6\theta\cdots \quad (18)$$

where θ is the angle between the c-axis and the magnetization vector, and K_{un} are the anisotropy constants.

Generally the order of magnitude of the number of terms involved in this polynomial very rapidly decreases when their power increases, thus a one constant approximation is possible as follows;

$$E_a = K_{u1} \sin^2 \theta . \tag{19}$$

According to this equation the shape of the energy surface is dependent on the sign of K_{u1}; when $K_{u1} > 0$, an oblate spheroid in which the lowest energy is located along the c axis ($\theta=n\pi$), whereas, when $K_{u1} < 0$, a prolate spheroid extended along the c axis having minimum energy in the x-y plane ($\theta=n+ \pi /2$).

In the case of cubic anisotropy when the other higher-order terms are negligibly small compared to the K_1 term a one-constant anisotropy equation can also be approximated from the series of polynomials

$$\begin{aligned} E_a &= K_1(\cos^2\theta_1 \cos^2\theta_2 + \cos^2\theta_2 \cos^2\theta_3 + \cos^2\theta_3 \cos^2\theta_1) + K_2(\cos^2\theta_1 \cos^2\theta_2 \cos^2\theta_3) \\ &+ K_3(\cos^2\theta_1 \cos^2\theta_2 + \cos^2\theta_2 \cos^2\theta_3 + \cos^2\theta_3 \cos^2\theta_1)^2 \cdots \end{aligned}$$

to be

$$E_a = K_1(\cos^2\theta_1 \cos^2\theta_2 + \cos^2\theta_2 \cos^2\theta_3 + \cos^2\theta_3 \cos^2\theta_1) \tag{20}$$

where θ_1, θ_2, θ_3 are the angles between magnetization vector and the three cubic axes (x, y, z) respectively.

Based on this one-constant anisotropy equation, <100> directions become the easy axes when K_1 is positive, while <111> directions become the easy axes when K_1 is negative.

2.1.6.2 Law of approach to saturation

For crystalline ferromagnetic materials, where the spontaneous magnetization is oriented along the easy axis due to the anisotropy energy, the rotation of the magnetization under applied magnetic field can be examined by finding the equilibrium angle of magnetization with respect to the applied field (H) where the total energy becomes a minimum;

$$\frac{dE_{tot}}{d\theta} = 0 \text{ and } \frac{d^2E_{tot}}{d\theta^2} > 0. \tag{21}$$

where θ is the angle between magnetization and the applied magnetic field (H).

Assuming that the total magnetic energy is only the sum of anisotropy energy (E_{an}) and Zeeman energy (E_{Zeeman}), the total energy can be expressed as

$$\begin{aligned} E_{tot} &= E_{an} + E_{Zeeman} \\ &= K_1(\cos^2\theta_1\cos^2\theta_2 + \cos^2\theta_2\cos^2\theta_3 + \cos^2\theta_3\cos^2\theta_1) + M\cdot\mu_0 H. \end{aligned} \tag{22}$$

The equilibrium angle θ can be obtained from the equation

$$\frac{dE_{tot}}{d\theta} = 0 = \frac{dE_{an}}{d\theta} - \mu_0 M_S H \sin\theta. \tag{23}$$

If θ is very small, the equation becomes

$$\left(\frac{dE_{an}}{d\theta}\right)_{\theta=0} - \mu_0 M_S H\theta = 0. \tag{24}$$

Therefore, θ can be obtained by

$$\theta = \frac{\left(\frac{dE_{an}}{d\theta}\right)_{\theta=0}}{\mu_0 M_S H} . \tag{25}$$

Since the component of magnetization in the direction of the applied magnetic field (H) is given by

$$M = M_S \cos\theta . \tag{26}$$

In the high field region the magnetization approaches saturation. Provided the effects of defects and localized inhomogeneities are sufficiently small, the magnetization in the high field region can be expressed as

$$M = M_S \cos\theta = M_S\left(1 - \frac{\theta^2}{2} + \cdots\right). \tag{27}$$

Therefore substituting equation (25) for small θ in equation (27) results in,

$$M = M_S(1 - \frac{\left(\frac{(dE_{an}/d\theta)_{\theta=0}}{\mu_0 M_S H}\right)^2}{2} + \cdots) . \tag{28}$$

For cubic anisotropy, since the magnetization rotates along the maximum gradient of the anisotropy energy in the vicinity of H,

$$\left[\left(\frac{dE_{an}}{d\theta}\right)_{\theta=0}\right]^2 = \left|\text{grad } E_{an}\right|^2 = \left(\frac{\partial E_{an}}{\partial\theta}\right)^2 + \frac{1}{\sin^2\theta}\left(\frac{\partial E_{an}}{\partial\varphi}\right)^2 \tag{29}$$

where (θ, φ) are the polar coordinates of the magnetization at equilibrium state under applied magnetic field (H).

By using the relationships of

$$\cos\theta_1 = \sin\theta\cos\varphi, \quad \cos\theta_2 = \sin\theta\sin\varphi, \quad \cos\theta_3 = \cos\theta \tag{30}$$

and

$$\begin{aligned}
\frac{\partial E_{an}}{\partial\theta} &= \left(\frac{\partial E_{an}}{\partial\cos\theta_1}\right)\frac{\partial\cos\theta_1}{\partial\theta} + \left(\frac{\partial E_{an}}{\partial\cos\theta_2}\right)\frac{\partial\cos\theta_2}{\partial\theta} + \left(\frac{\partial E_{an}}{\partial\cos\theta_3}\right)\frac{\partial\cos\theta_3}{\partial\theta} \\
\frac{1}{\sin\theta}\frac{\partial E_{an}}{\partial\varphi} &= \left(\frac{\partial E_{an}}{\partial\cos\theta_1}\right)\frac{\partial\cos\theta_1}{\sin\theta\,\partial\varphi} + \left(\frac{\partial E_{an}}{\partial\cos\theta_2}\right)\frac{\partial\cos\theta_2}{\sin\theta\,\partial\varphi} + \left(\frac{\partial E_{an}}{\partial\cos\theta_3}\right)\frac{\partial\cos\theta_3}{\sin\theta\,\partial\varphi}
\end{aligned} \tag{31}$$

the equation (29) becomes

$$\begin{aligned}
\left|\text{grad } E_{an}\right|^2 = &\left(\frac{\partial E_{an}}{\partial\cos\theta_1}\right)^2 + \left(\frac{\partial E_{an}}{\partial\cos\theta_2}\right)^2 + \left(\frac{\partial E_{an}}{\partial\cos\theta_3}\right)^2 \\
&- \left\{\left(\frac{\partial E_{an}}{\partial\cos\theta_1}\right)\cos\theta_1 + \left(\frac{\partial E_{an}}{\partial\cos\theta_2}\right)\cos\theta_2 + \left(\frac{\partial E_{an}}{\partial\cos\theta_3}\right)\cos\theta_3\right\}^2
\end{aligned} \tag{32}$$

Let each term be replaced by the relationships of

$$\begin{aligned}
\frac{\partial E_{an}}{\partial\cos\theta_1} &= 2K_1\cos\theta_1\left(1-\cos^2\theta_1\right) \\
\frac{\partial E_{an}}{\partial\cos\theta_2} &= 2K_1\cos\theta_2\left(1-\cos^2\theta_2\right) \\
\frac{\partial E_{an}}{\partial\cos\theta_3} &= 2K_1\cos\theta_3\left(1-\cos^2\theta_3\right)
\end{aligned} \tag{33}$$

then the equation can be simplified to be

$$\begin{aligned}
\left|\text{grad } E_{an}\right|^2 = 4K_1^2\{&(\cos^6\theta_1 + \cos^6\theta_2 + \cos^6\theta_3) \\
&-(\cos^8\theta_1 + \cos^8\theta_2 + \cos^8\theta_3) \\
&-2(\cos^4\theta_1\cos^4\theta_2 + \cos^4\theta_2\cos^4\theta_3 + \cos^4\theta_3\cos^4\theta_1)\}.
\end{aligned} \tag{34}$$

For a randomly oriented polycrystalline sample, the average value of each term inside the parenthesis can be calculated to be

$$\left|\text{grad } E_{an}\right|^2 = 4K_1^2\left\{\frac{3}{7}-\frac{3}{9}-2\frac{3}{105}\right\} = \frac{16}{105}K_1^2 \tag{35}$$

Substituting this equation (35) in equation (28) results in

$$\begin{aligned} M &= M_S(1-\frac{\left(\frac{\left(dE_{an}/d\theta\right)_{\theta=0}}{\mu_0 M_S H}\right)^2}{2}-\cdots) \\ &= M_S\left[1-\frac{8}{105}\frac{K_1^2}{\left(\mu_0 M_S H\right)^2}-\cdots\right] \end{aligned} \tag{36}$$

This resultant equation shows the relationship between magnetization and the anisotropy constant K_1 of the polycrystalline samples with cubic symmetry, however, this formula is only applicable under an assumption that the grains in the polycrystalline material have no texture in orientation and would not interact magnetically with each other.

2.1.7 Magnetostriction

Magnetostriction is the change in dimension of a solid that accompanies the change in magnetic state. Conversely, the magnetic structure of the material may vary with the mechanical state.

For materials with ordered magnetic structures, magnetostriction can be classified into spontaneous magnetostriction and field induced magnetostriction. The former is accompanied by the formation of domains below the ordering temperature, whereas the latter arises from the reorientation of domains. The field induced magnetostriction was first discovered by Joule in 1842 thus sometimes being called as Joule magnetostriction or anisotropic magnetostriction.

Magnetostriction is usually expressed as λ, the fractional change in length l

$$\lambda = \frac{\Delta l}{l} \tag{37}$$

to make a distinction from the mechanical strain ε. The response of λ to applied magnetic field can be either positive or negative depending on the material. A schematic diagram illustrating the various magnetostriction modes is shown in Fig. 3.

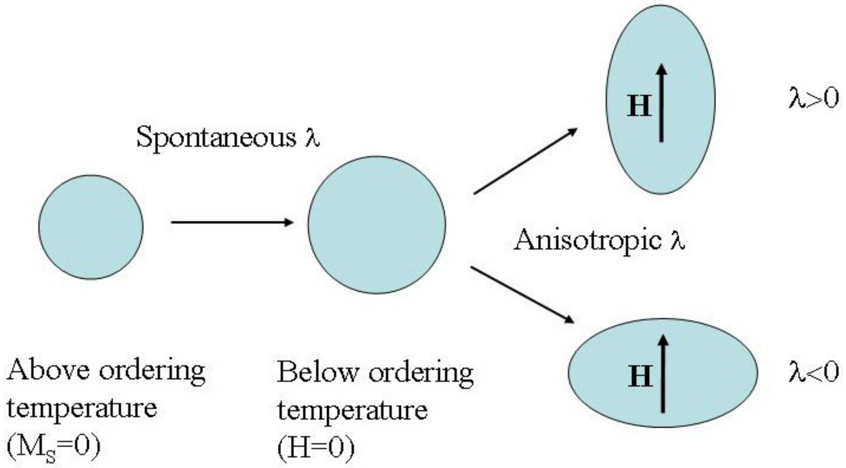

Fig. 3. Schematic diagram illustrating the various magnetostriction modes

The magnetostrictive strain at saturation relative to the length in the demagnetized state is called saturation magnetostriction λ_s, which corresponds to the difference in strain of between the right ellipsoid and middle sphere in Fig. 3. For the purpose of comparison among materials, λ_s is usually used as a characteristic value of magnetostrictive properties because it is an intrinsic property of the material.

For isotropic materials or for randomly oriented polycrystals, if volume conservation is assumed, the magnetostriction can be expressed as a function of θ by,

$$\lambda(\theta) = \frac{3}{2}\lambda_s\left(\cos^2\theta - \frac{1}{3}\right) \tag{38}$$

where θ is the angle between the measurement direction and the magnetization direction.

For the measurement of λ_s, the magnetostriction parallel to the applied field direction $\lambda_{//}$, and the magnetostriction perpendicular to the field direction $\lambda_\perp$, are measured and the difference is taken as follows,

$$\begin{aligned}
\lambda_{//} &= \lambda(0) = \frac{3}{2}\lambda_s\left(\cos^2 0 - \frac{1}{3}\right) = \lambda_s \\
\lambda_\perp &= \lambda(90^o) = \frac{3}{2}\lambda_s\left(\cos^2 90^o - \frac{1}{3}\right) = -\frac{\lambda_s}{2} \\
\frac{2}{3}(\lambda_{//} - \lambda_\perp) &= \frac{2}{3}\left(\lambda_s + \frac{\lambda_s}{2}\right) = \lambda_s.
\end{aligned} \tag{39}$$

Fig. 4 shows the magnetostriction curve from the demagnetized state. For isotropic samples, which is given by Fig. 4 (a), $\lambda_{//} = -2\lambda_\perp$ because the demagnetized state is isotropic. In the cases of Fig. 4 (b) and (c), however, the shapes of magnetostriction curves of $\lambda_{//}$ and $\lambda_\perp$ are entirely dependent on the preferred magnetization direction in the demagnetized state, on which various external factors, such as stress, can make an effect.

For these reasons, saturation magnetostriction $\left(\lambda_s = \frac{2}{3}(\lambda_{//} - \lambda_\perp)\right)$ is usually taken in order to eliminate the uncertain effect of the initial state.

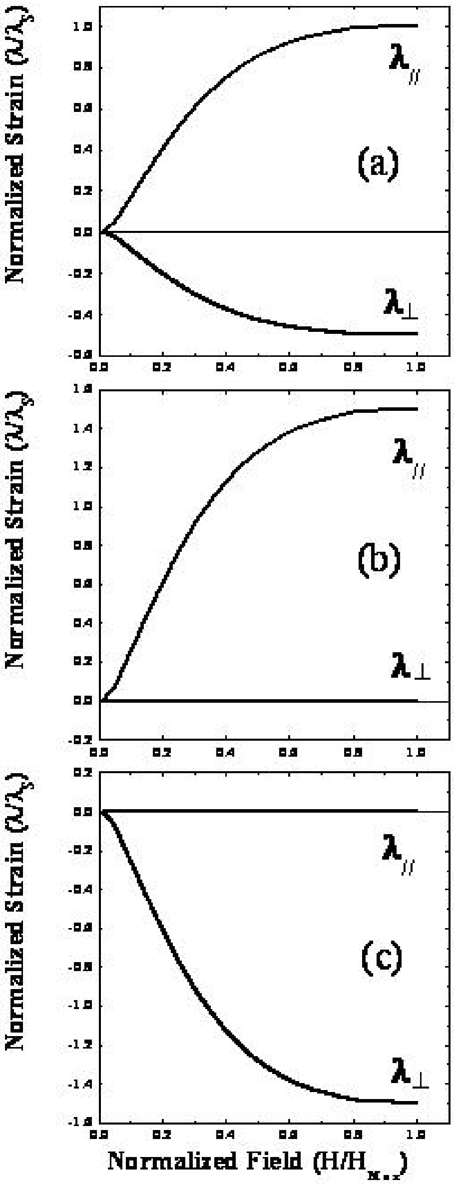

Fig. 4. Schematic diagram illustrating the parallel and perpendicular magnetostriction curves from the various demagnetized states of (a) isotropy (b) easy axis parallel to the measurement direction (c) easy axis perpendicular to the measurement direction**.**

2.1.7.1 Cubic materials

The generalized version of the equation for saturation magnetostriction of single crystal cubic materials is given by [25]

$$\begin{aligned}\lambda_s = \frac{3}{2}\lambda_{100}\left(\alpha_1^2\beta_1^2 + \alpha_2^2\beta_2^2 + \alpha_3^2\beta_3^2 - \frac{1}{3}\right) \\ + 3\lambda_{111}\left(\alpha_1\alpha_2\beta_1\beta_2 + \alpha_2\alpha_3\beta_2\beta_3 + \alpha_3\alpha_1\beta_3\beta_1\right)\end{aligned} \tag{40}$$

where λ_{100} and λ_{111} are the saturation magnetostrictions measured along the <100> and <111> directions respectively, and (α_1, α_2, α_3) and (β_1, β_2, β_3) are the direction cosines of the magnetization and strain measurement directions respectively, with respect to the cubic crystal axes.

Under the assumption that the saturation magnetization is parallel to the applied magnetic field and strain measurement direction, and by replacing (β_1, β_2, β_3) with (α_1, α_2, α_3), the above expression reduces to

$$\lambda_s = \lambda_{100} + 3(\lambda_{111} - \lambda_{100})\left(\alpha_1^2\alpha_2^2 + \alpha_2^2\alpha_3^2 + \alpha_3^2\alpha_1^2\right). \tag{41}$$

For polycrystalline cubic materials with randomly oriented crystallites the following formula can be considered a good approximation [26]:

$$\lambda_s = c\lambda_{100} + (1-c)\lambda_{111}, \quad c = \frac{2}{5} - \frac{1}{8}\ln r_a, \quad r_a = \frac{2c_{44}}{c_{11} - c_{44}} \tag{42}$$

where c is a coefficient that can be calculated by averaging the deformation in each crystallite over different crystal orientations, and r_a is a measure of elastic anisotropy of the cubic material.

A simpler expression with c=2/5 can be obtained when r_a=1, which is valid for materials with isotropic elastic properties.

2.2 Ferrite

2.2.1 Spinels

The spinel ferrites are a large group of oxides which possess the structure of the natural spinel $MgAl_2O_4$. More than 140 oxides and 80 sulphides have been systematically studied [27].

Fig. 5 and 6 show the unit cell and its projection on the base plane of the cubic spinel structure, in which two types of subcells alternate in a three-dimensional array so that each fully repeating unit cell requires eight subcells. Two kinds of subcells are indicated, one of which is a tetrahedral site in the body center (green) and the other one of which is an octahedral site (red). Each A atom in a tetrahedral site has 12 nearest B atoms and each B atom in an octahedral site has 6 nearest A atoms, which is shown in Fig. 7. In the case when both A and B atoms are magnetic elements, there is an exchange interaction between A and B atoms and the number of nearest neighbor exchange interactions for each site should be also different for each site. This difference in number of exchange interactions, depending on the crystallographic position of each magnetic element, may give physically important meaning for interpreting the magnetic properties of this material because exchange interactions among magnetic elements are the fundamental reason for magnetic ordering of magnetic materials. For this reason, the magnetic properties of cubic spinel ferrites are known to be strongly related to the cation distribution between tetrahedral and octahedral sites. The general chemical formula of spinel structure is given by

$$\left(\overrightarrow{A_X B_{1-X}}\right) O \cdot [\overleftarrow{A_{1-X} B_{1+X}}] O_3 \qquad (43)$$

where cations inside the parenthesis “( )” are indicated to be in tetrahedral sites and those inside the bracket “[ ]” are in octahedral sites. x varies from 0 to 1 depending on the materials; When x=1 the material is called normal spinel. When x=0 the material is called inverse spinel. When 0<x<1 the material is called mixed spinel.

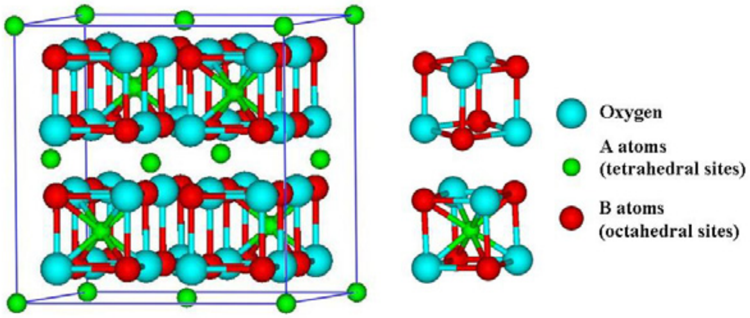

Fig. 5. Unit cell of cubic spinel crystal structure of AB_2O_4

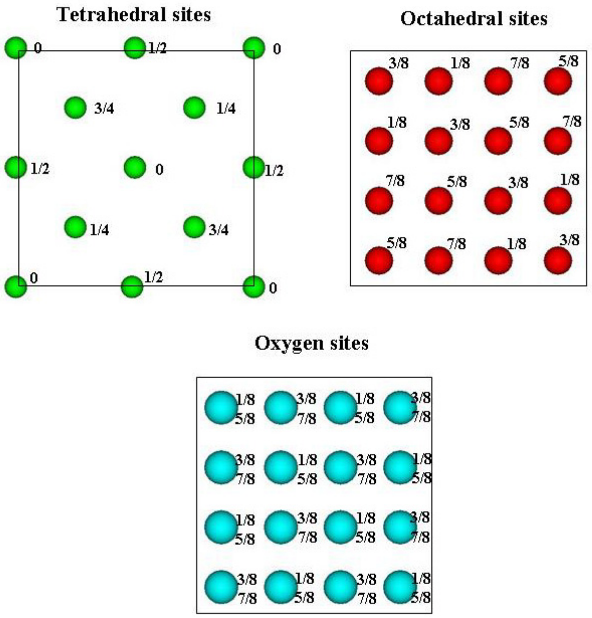

Fig. 6. Projection of the spinel ionic positions on to a cube face, for a perfect system where the oxygen parameter u=3/8. Numbers give the ion positions perpendicular to a cube face as a fraction of the cube edge.

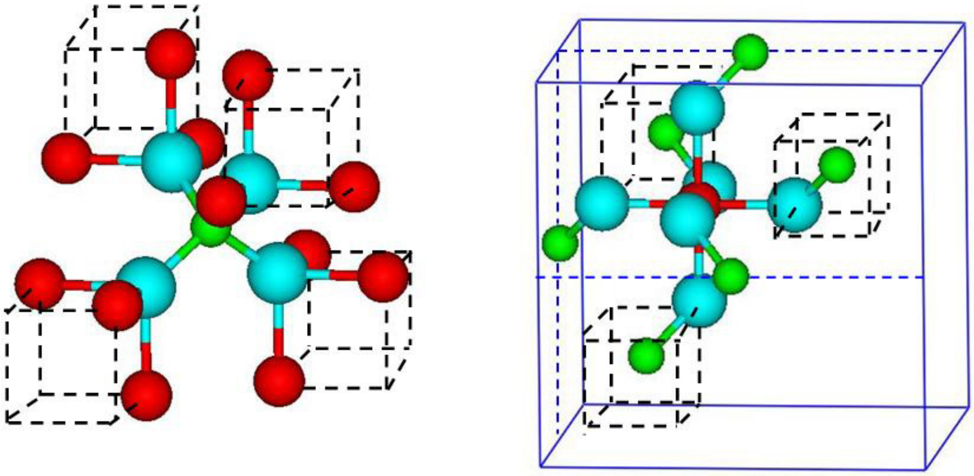

Tetrahedral site (A site)
; 12 nearest A atoms

Octahedral site (B site)
; 6 nearest A atoms

(a) (b)

Fig. 7. Schematic diagram illustrating the local atomic arrangements for (a) tetrahedral site and (b) octahedral site in spinel structure.

2.2.2 Magnetic moments of inverse spinels

Once the cations' distribution between tetrahedral and octahedral sites is identified we can predict the magnetic moments of the formula unit. Because the thermal disturbance of the magnetic moments will lower the net magnetic moment, the theoretical values of magnetic moments are generally referred to the value at absolute zero or 0 K. For practical application to experimentally measured data the saturated magnetic moment is usually determined by extrapolation to 0 K of the measured data at very low temperatures.

In the general chemical formula unit of spinel ferrite expressed in (43), the magnetic moments of cations in tetrahedral sites are oppositely directed to those in octahedral sites.

If M_A and M_B are the magnetic moments of A and B ions then the saturation magnetic moment per formula unit at 0 K can be calculated by

$$\mathrm{M} = \left[(1-\mathrm{X})\mathrm{M}_{\mathrm{A}} + (1+\mathrm{X})\mathrm{M}_{\mathrm{B}}\right] - \left\{\mathrm{X}\mathrm{M}_{\mathrm{A}} + (1-\mathrm{X})\mathrm{M}_{\mathrm{B}}\right\}. \tag{44}$$

In the case of cobalt ferrite, if it has a completely inverse spinel structure, the formula unit is

$$\left(\overrightarrow{\mathrm{Fe}^{3+}}\right)\mathrm{O}\cdot[\overleftarrow{\mathrm{Co}^{2+}\mathrm{Fe}^{3+}}]\mathrm{O}_3. \tag{45}$$

The spin magnetic moments for Fe^{3+} and Co^{2+} are 5 μ_B and 3 μ_B respectively. Based on these values the magnetic moments per formula unit of cobalt ferrite can be calculated as follows,

$$\begin{aligned} \mathrm{M} &= \left[(5+3)-5\right]\mu_{\mathrm{B}} \\ &= 3\mu_{\mathrm{B}}. \end{aligned} \tag{46}$$

However, the experimentally measured values of cobalt ferrites have been reported to be ~3.94 μ_B [28, 29], which is due to a contribution from the orbital magnetic moment of cobalt ion Co^{2+} remaining unquenched by the crystalline field. Specific details regarding orbital magnetic moment will be discussed at the following sections. Experimental results indicate that cobalt ferrite is neither fully normal spinel nor fully inverse spinel [30, 31], because the cobalt atoms are distributed among both the A sites and the B sites. Moreover, the directions of the magnetic moments in A and B sites may not be completely antiparallel, in other words, they may be canted [32]. Therefore calculation of the saturation magnetic moment of cobalt ferrite needs to be performed after taking these factors into consideration.

2.2.3 Single ion anisotropy

For cubic spinel ferrites, as previously mentioned, there are two kinds of interstitial sites inside the close-packed oxygen lattice. The tetrahedral sites are surrounded by four nearest neighbor O^{2-} ions, and the octahedral sites are surrounded by six O^{2-} ions. The sizes of all of the metal ions in the third and fourth periods in the periodic table, which are of interest at this study, are small enough to occupy these lattice sites. Cobalt ferrite has the composition $Co^{2+}Fe^{3+}{}_2O_4$, and in its inverse spinel form one Fe^{3+} would occupy the tetrahedral site, while the other Fe^{3+} and the Co^{2+} would occupy the two octahedral sites. Strictly speaking, the site occupation for Fe^{3+} and Co^{2+} ions is known to vary with fabrication processes [30, 31], however, for simplicity an inverse spinel structure of cobalt ferrite is assumed here. Generally, the energy levels of d-electrons which are degenerate in the free ion state are split into doubly degenerate dγ levels (d_{x2-y2}, d_{z2}) and triply degenerate dε levels (d_{xy}, d_{yz}, d_{xz}) when they are located in a cubic crystal field of octahedral symmetry (Fig. 8). This energy shift is due to the electrostatic interaction between the differently shaped electron clouds of d orbitals in metal ions and that of p orbitals of neighboring oxygen atoms. More specifically, the dγ wave function stretches along a cubic axis on which the nearest neighbor O^{2-} ion is located, so that because of the Coulomb interaction between the negatively charged electron and the O^{2-} ion, the energy level of dγ is increased; while the dε wave function stretches between two cubic axes and avoids the O^{2-} ions, so that the Coulomb energy is relatively small and the energy of the dε level is lowered. In addition to this, the second nearest neighbor metal ions surrounding an octahedral site are arranged symmetrically about the trigonal axis, so that they produce a trigonal field which causes the three dε states to recombine to form three new orbitals compatible with trigonal symmetry. In consequence, the triply degenerate dε levels are split into an isolated lower single level, which corresponds to the wave function being concentrated along the trigonal axis and the doubly degenerate higher levels which correspond to the wave functions stretching perpendicular to the trigonal axis. The schematic diagram for the energy level splitting of 3d electrons inside cubic lattice is shown in Fig. 9.

According to Hund's rule, five electrons out of seven in the Co^{2+} ion in an octahedral site fill up the + spin levels, while the remaining two electrons occupy the – spin levels; this high spin state is valid only when the stabilization energy of Hund's rule is greater than that of crystal field splitting, which is generally valid in the case of 3d ions [33]. The last electron which occupies one of the doubly degenerate levels can alternate between the two possible wave functions, thus realizing a circulating orbit. The orbital magnetic moment L interacts with the total spin moment S of the Co^{2+}, which is the so called "spin-orbit" coupling, the general form being given by

$$w = k\, L \cdot S \tag{47}$$

where k is the spin orbit coupling coefficient.

Since the number of electrons in a Co^{2+} ion is more than half the number required for a filled shell, L is parallel to S (by Hund's rule), and $k < 0$. When, therefore, S has a positive component parallel to the trigonal axis, L points in the + direction of this axis. When S is rotated so that it has a negative component, L is reversed. Therefore the interaction energy in this case is given by

$$W=kLS|\cos\theta| \tag{48}$$

where θ is the angle between L and S directions.

In cubic crystals there are four <111> axes. If Co^{2+} ions are distributed equally on octahedral sites with different <111> axes, the anisotropy energy produced by equation (48) becomes

$$E_a = \frac{1}{4}NkLS\left(\left|\cos\theta_1\right| + \left|\cos\theta_2\right| + \left|\cos\theta_3\right| + \left|\cos\theta_4\right|\right) \tag{49}$$

where θ_1, θ_2, θ_3, and θ_4 are the angles between S and the four <111> axes and N is the number of Co^{2+} ions.

By Fourier expansion, $|\cos\theta|$ is reduced to

$$\begin{aligned} \left|\cos\theta_1\right| &= \frac{\pi}{3}\cos 2\theta - \frac{\pi}{15}\cos 4\theta + \cdots \\ &= \frac{\pi}{3}(2\cos^2\theta - 1) - \frac{\pi}{15}(8\cos^4\theta - 8\cos^2\theta + 1) + \cdots \\ &= \frac{18\pi}{15}\cos^2\theta - \frac{8\pi}{15}\cos^4\theta + \cdots \end{aligned} \tag{50}$$

Therefore equation (49) becomes

$$\begin{aligned} E_a &= \frac{1}{4}NkLS[\frac{18\pi}{15}\{(\alpha_1^2+\alpha_2^2+\alpha_3^2)^2 + (\alpha_1^2+\alpha_2^2-\alpha_3^2)^2 + (\alpha_1^2-\alpha_2^2+\alpha_3^2)^2 + (-\alpha_1^2+\alpha_2^2+\alpha_3^2)^2\} \\ &\quad - \frac{18\pi}{135}\{(\alpha_1^2+\alpha_2^2+\alpha_3^2)^4 + (\alpha_1^2+\alpha_2^2-\alpha_3^2)^4 + (\alpha_1^2-\alpha_2^2+\alpha_3^2)^4 + (-\alpha_1^2+\alpha_2^2+\alpha_3^2)^4\}] \\ &= -\frac{32\pi}{135}NkLS(\alpha_1^2\alpha_2^2 + \alpha_2^2\alpha_3^2 + \alpha_3^2\alpha_1^2) \end{aligned} \tag{51}$$

Since $k < 0$ (by Hund's rule), the anisotropy constant in equation (51) is positive. This explains the fact that while many ferrites have negative K_1, but the addition of Co tends to make K_1 positive. In the case of metal ions other than Co^{2+}, the orbital moment L is induced through the LS coupling, and this induced L gives rise to magnetic anisotropy through the LS coupling.

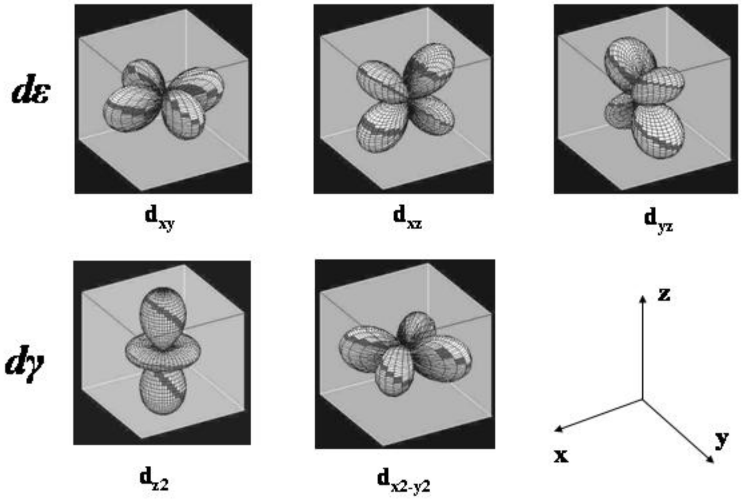

Fig. 8. The dε and dγ wave functions of 3d electrons.

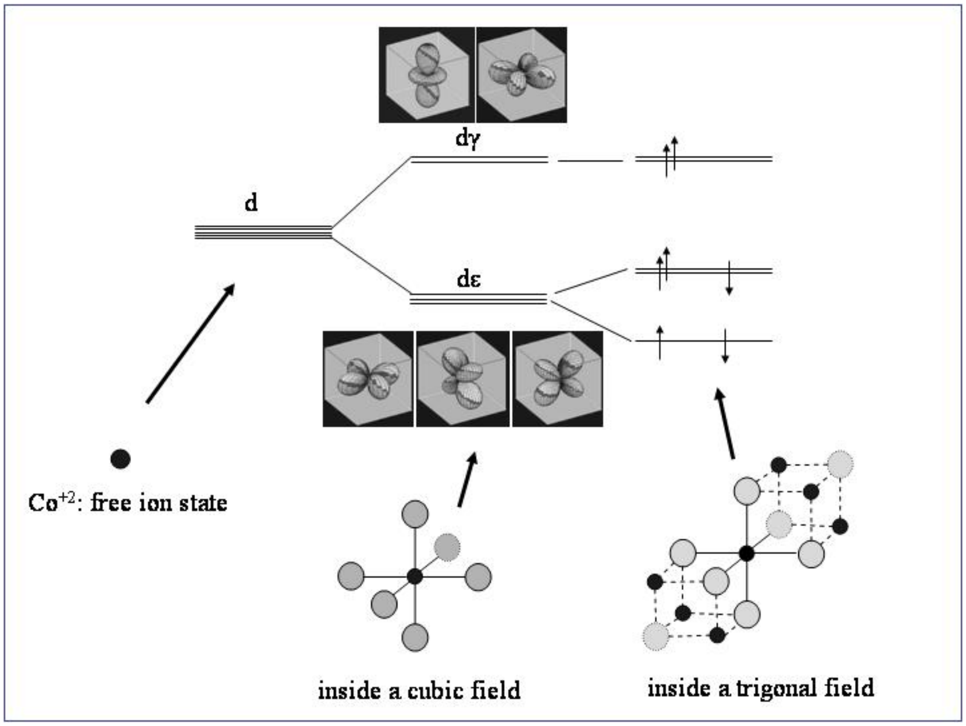

Fig. 9. Schematic diagram illustrating the splitting of energy levels of 3d electrons by crystalline fields with different symmetry.

2.2.4 Two sublattice magnetizations

Neel [34] postulated the two separate sublattice model as an explanation of ferrimagnetism (and antiferromagnetism). In this model it was assumed that each sublattice possesses its own spontaneous magnetization so that the total magnetization is the vector superposition of the two sublattice magnetizations.

The formation of spontaneous magnetization in ferrites can be explained as in ferromagnetic materials by using the Weiss molecular field theory. An important difference in Neel's two sublattice model was, however, that the total effective molecular field acting on each magnetic moment was assumed to be resulting from the superposition of the two different intra- and inter-sublattice molecular fields given by,

$$\begin{aligned} H_{eff}^{A} &= \alpha_{AA} M^{A} - \alpha_{AB} M^{B} \\ H_{eff}^{B} &= \alpha_{BB} M^{B} - \alpha_{AB} M^{A} \end{aligned} \tag{52}$$

where α_{AA}, α_{BB}, and α_{AB} are intra-sublattice molecular field constants for sublattice A and B respectively, and inter-sublattice molecular field constant between sublattice A and B.

The field-dependent and temperature-dependent magnetization in each sublattice can be then described by a Brillouin function with different effective fields on each sublattice $H_{eff}{}^{A}$ and $H_{eff}{}^{B}$ being variables, as follows [1],

$$\begin{aligned} M^{A}(H,T) &= M_{S}^{A} B_{J}\left[\frac{gJ^{A}\mu_{B}\mu_{0}\left(H + H_{eff}^{A}\right)}{k_{B}T}\right] = N_{V}^{A} gJ^{A}\mu_{B} B_{J}\left(\frac{gJ^{A}\mu_{B}\mu_{0}\left(H + \alpha_{AA}M^{A} - \alpha_{AB}M^{B}\right)}{k_{B}T}\right) \\ M^{B}(H,T) &= M_{S}^{B} B_{J}\left[\frac{gJ^{B}\mu_{B}\mu_{0}\left(H + H_{eff}^{B}\right)}{k_{B}T}\right] = N_{V}^{B} gJ^{B}\mu_{B} B_{J}\left(\frac{gJ^{B}\mu_{B}\mu_{0}\left(H + \alpha_{BB}M^{B} - \alpha_{AB}M^{A}\right)}{k_{B}T}\right) \\ M(H,T) &= M^{B}(H,T) - M^{A}(H,T) \end{aligned} \tag{53}$$

where

$$B_{J}(x) = \left(\frac{2J+1}{2J}\right)\coth\left[\frac{(2J+1)x}{2J}\right] - \left(\frac{1}{2J}\right)\coth\left(\frac{x}{2J}\right)$$

At temperatures above the Curie temperature, using the high temperature approximation to equation (9), we have

$$
\begin{aligned}
M^{A} &= \frac{N_V^A g^2 J^A\left(J^A+1\right)\mu_B^2\mu_0\left(H+\alpha_{AA}M^A-\alpha_{AB}M^B\right)}{3k_B T}\\
M^{B} &= \frac{N_V^A g^2 J^B\left(J^B+1\right)\mu_B^2\mu_0\left(H+\alpha_{BB}M^B-\alpha_{AB}M^A\right)}{3k_B T}\\
&\text{let } C_A = \frac{N_V^A g^2 J^A\left(J^A+1\right)\mu_B^2\mu_0}{3k_B} \text{ and } C_B = \frac{N_V^B g^2 J^B\left(J^B+1\right)\mu_B^2\mu_0}{3k_B}, \quad \text{then} \qquad (54)\\
M^{A} &= \frac{C_A\left(H-\alpha_{AB}M^B\right)}{T-C_A\alpha_{AA}}\\
M^{B} &= \frac{C_B\left(H-\alpha_{AB}M^A\right)}{T-C_B\alpha_{BB}}
\end{aligned}
$$

Solving these simultaneous equations results in

$$
\begin{aligned}
M^{A} &= \frac{\left\{C_A T - C_A C_B\left(\alpha_{BB}+\alpha_{AB}\right)\right\}H}{T^2-\left(C_A\alpha_{AA}+C_B\alpha_{BB}\right)T+C_A C_B\left(\alpha_{AA}\alpha_{BB}-\alpha_{AB}^2\right)}\\
M^{B} &= \frac{\left\{C_B T - C_A C_B\left(\alpha_{AA}+\alpha_{AB}\right)\right\}H}{T^2-\left(C_A\alpha_{AA}+C_B\alpha_{BB}\right)T+C_A C_B\left(\alpha_{AA}\alpha_{BB}-\alpha_{AB}^2\right)}\\
M = M^A + M^B &= \frac{C_A\left(T-C_B\alpha_{BB}-C_B\alpha_{AB}\right)H+C_B\left(T-C_A\alpha_{AA}-C_A\alpha_{AB}\right)H}{T^2-\left(C_A\alpha_{AA}+C_B\alpha_{BB}\right)T+C_A C_B\left(\alpha_{AA}\alpha_{BB}-\alpha_{AB}^2\right)} \qquad (55)\\
&= \frac{\left(C_A+C_B\right)T-C_A C_B\left(\alpha_{AA}+\alpha_{BB}+2\alpha_{AB}\right)}{T^2-\left(C_A\alpha_{AA}+C_B\alpha_{BB}\right)T+C_A C_B\left(\alpha_{AA}\alpha_{BB}-\alpha_{AB}^2\right)}H
\end{aligned}
$$

This equation can be simplified to

$$
\begin{aligned}
\frac{1}{\chi} = \frac{H}{M} &= \frac{T^2-\left(C_A\alpha_{AA}+C_B\alpha_{BB}\right)T+C_A C_B\left(\alpha_{AA}\alpha_{BB}-\alpha_{AB}^2\right)}{\left(C_A+C_B\right)T-C_A C_B\left(\alpha_{AA}+\alpha_{BB}+2\alpha_{AB}\right)}\\
&= \frac{T}{C_A+C_B}-\frac{C_A^2\alpha_{AA}+C_B^2\alpha_{BB}-2C_A C_B\alpha_{AB}}{\left(C_A+C_B\right)^2} \qquad (56)\\
&\quad -\frac{C_A C_B}{C_A+C_B}\left\{C_A\left(\alpha_{AA}+\alpha_{AB}\right)-C_A\left(\alpha_{AA}+\alpha_{AB}\right)\right\}^2\cdot\frac{1}{T-\dfrac{C_A C_B\left(\alpha_{AA}+\alpha_{BB}\right)-2C_A C_B\alpha_{AB}}{\left(C_A+C_B\right)}}
\end{aligned}
$$

At Curie temperature, $1/\chi=0$, so that we have [35]

$$T_C{}^2 - \left(C_A\alpha_{AA} + C_B\alpha_{BB}\right)T_C + C_A C_B\left(\alpha_{AA}\alpha_{BB} - \alpha_{AB}^2\right) = 0 \qquad (57)$$

Solving this equation with respect to T_C results in

$$T_C = \frac{1}{2}\left(C_A\alpha_{AA} + C_B\alpha_{BB}\right) \pm \sqrt{\left(C_A\alpha_{AA} - C_B\alpha_{BB}\right)^2 + 4C_A C_B\alpha_{AB}^2} \qquad (58)$$

Since

$$\left[\frac{1}{2}\left(C_A\alpha_{AA} + C_B\alpha_{BB}\right)\right]^2 \quad \langle \quad \left(C_A\alpha_{AA} - C_B\alpha_{BB}\right)^2 + 4C_A C_B\alpha_{AB}^2 \qquad (59)$$

the positive value of T_C is given by

$$T_C = \frac{1}{2}\left(C_A\alpha_{AA} + C_B\alpha_{BB}\right) + \sqrt{\left(C_A\alpha_{AA} - C_B\alpha_{BB}\right)^2 + 4C_A C_B\alpha_{AB}^2} \qquad (60)$$

This resultant equation shows the dependence of T_C on the molecular field constants α_{AA}, α_{BB}, and $\alpha_{AB.}$

2.2.5 Exchange energy in a two sublattice structure

Based on the nearest-neighbor exchange interaction approximation, the intra- and inter-sublattice exchange interaction energy can be expressed as [35]

$$\begin{aligned}
E_{ex}^{AA} &= -J_{AA}N_V^A Z_{AA} J_A \cdot J_A = -\frac{1}{2}\mu_0\alpha_{AA}M_A^2 = -\frac{1}{2}\mu_0\alpha_{AA}\left(N_V^A g J_A \mu_B\right)^2 \\
E_{ex}^{BB} &= -J_{BB}N_V^B Z_{BB} J_B^2 = -\frac{1}{2}\mu_0\alpha_{BB}M_B^2 = -\frac{1}{2}\mu_0\alpha_{BB}\left(N_V^B g J_B \mu_B\right)^2 \\
E_{ex}^{AB} &= -J_{AB}N_V^{A+B} Z_{AB} J_A \cdot J_B = -\frac{1}{2}\mu_0\alpha_{AB}M_A M_B = -\frac{1}{2}\mu_0\alpha_{AB}\left(N_V^A g J_A \mu_B\right)\left(N_V^B g J_B \mu_B\right)
\end{aligned} \qquad (61)$$

where $E_{ex}{}^{AA}$, $E_{ex}{}^{BB}$, $E_{ex}{}^{AB}$ are indicating of exchange energy densities from A-A, B-B, and A-B nearest exchange interactions respectively.

From these equations we can obtain the molecular field constants in terms of the exchange interaction constants as

$$\alpha_{AA} = \frac{2Z_{AA}J_{AA}}{\mu_0 N_V^A g^2 \mu_B^2}$$
$$\alpha_{BB} = \frac{2Z_{BB}J_{BB}}{\mu_0 N_V^B g^2 \mu_B^2} \qquad (62)$$
$$\alpha_{AB} = \frac{2N_V^{A+B} Z_{AB}J_{AB}}{\mu_0 N_V^A N_V^B g^2 \mu_B^2}$$

By substituting these equation to equation (55), the magnetization curve M(H, T) of ferrimagnets can be described in terms of the exchange interaction constants.

2.3 Thermodynamics of magnetostrictive materials

A mathematical statement of the first law of thermodynamics is as follows,

$$dU=\delta Q+\delta W+\delta W' \qquad (63)$$

where dU is the change in the state function U (the internal energy) for an infinitesimal step in the process, and δQ, δW, and δW' are incremental quantities of heat, mechanical work, and all other kinds of work done on the system.

When it comes to magnetic materials under applied magnetic field, we need to consider magnetic contribution to the internal energy U; change in magnetic energy $\mu_0 HdMV$, and change in magnetostrictive energy $-\sigma_M \lambda V$, where H, M, σ_M, λ, and V are applied magnetic field, magnetization, magnetoelastic stress, magnetostriction, and volume. Thus the change in internal energy on magnetizing a magnetostrictive material can be written as

$$dU = TdS - PdV+(\mu_0 HdM-\sigma_M \lambda)V \qquad (64)$$

The Gibbs free energy is

$$G = U+(P+\sigma e-\mu_0 HM)V-TS$$

$$dG = dU+PdV+VdP+(\sigma_M d\lambda+\lambda d\sigma_M+\mu_0 HdM+\mu_0 MdH)V-TdS-SdT \tag{65}$$

Substituting equation (64) into equation (65) gives

$$\begin{aligned} dG &= Tds-PdV+(\mu_0 HdM-\sigma_M\lambda)V+PdV+VdP+(\sigma_M\lambda+\lambda d\sigma_M-\mu_0 HdM- \\ &\quad \mu_0 MdH)V-TdS-SdT \\ &= -SdT+VdP-(\mu_0 MdH-\lambda d\sigma_M)V \end{aligned} \tag{66}$$

Important relations follow from the partial derivatives of the free energy;

$$\begin{aligned} &\left.\frac{\partial G}{\partial \sigma_M}\right)_{T,P,H} = V\lambda \\ &\left.\frac{1}{V}\frac{\partial G}{\partial H\partial \sigma_M}\right)_{T,P,\sigma_M} = \left(\frac{\partial \lambda}{\partial H}\right)_{T,P,\sigma_M} \equiv d(\text{piezomagnetic coefficient}) \\ &\left.\frac{\partial G}{\partial H}\right)_{T,P,\sigma_M} = \mu_0 MV = BV \\ &\left.\frac{1}{V}\frac{\partial G}{\partial \sigma_M \partial H}\right)_{T,P,H} = \left(\frac{\partial B}{\partial \sigma_M}\right)_{T,P,H} \equiv g(\text{piezomagnetic coefficient}) \end{aligned} \tag{67}$$

By Maxwell's relations, for small displacements,

$$\left.\frac{1}{V}\frac{\partial G}{\partial H\partial \sigma_M}\right)_{T,P,\sigma_M} = \left.\frac{1}{V}\frac{\partial G}{\partial \sigma_M \partial H}\right)_{T,P,H} \tag{68}$$

and therefore

$$\left(\frac{\partial \lambda}{\partial H}\right)_{T,P,\sigma_M} = \left(\frac{\partial B}{\partial \sigma_M}\right)_{T,P,H} \tag{69}$$

The resultant equation is an important result because it indicates that materials with a high strain derivative $(d\lambda/dH)_\sigma$ will show high stress sensitivity $(dB/d\sigma_M)_H$.

3. EXPERIMENTAL PROCEDURE

3.1 Preparation of samples

A series of polycrystalline Mn-, Cr-, and Ga- Ge-substituted cobalt ferrite samples with compositions of $CoM_xFe_{2-x}O_4$ (where M=Mn, Cr, Ga and x= 0.0 to 0.8) and $Co_{1+x}Ge_xFe_{2-2x}O_4$ (where x=0.0 to 0.6) were prepared by standard powder ceramic techniques using Fe_2O_3, M_2O_3 (M=Mn, Cr, Ga) or GeO_2, and Co_3O_4 powder as precursors.

Stoichiometrically blended powder was calcined at 1000°C for 24 hours, ball milled, and sieved to sizes <30 μm using a 400 mesh screen. After repeating the calcining procedure the powder was cold pressed at up to 15000 pound ram force using a 0.75 inch diameter die. The cold pressed “green state” samples were sintered at 1350°C for up to 24 hours and subsequently furnace cooled to room temperature.

3.2 Crystal/micro structure and chemical composition analysis

X-ray powder diffraction analysis of the samples with various compositions indicated that, within experimental error, they have single phase cubic spinel structure. The lattice parameter of each sample was determined by Rietveld refinement based on the X-ray powder diffraction data. Microstructures of the sintered samples were investigated using a JEOL 5910 scanning electron microscope (SEM) and quantitative compositional analysis was performed using energy-dispersive spectroscopy (EDS).

3.3 Magnetic properties measurement

Magnetic properties were measured using a vibrating sample magnetometer (VSM) and a superconducting quantum interference device (SQUID). For the measurements of the Curie temperature, T_C, the VSM was used to measure the magnetization (M) versus temperature (T) curve in the high temperature region from ambient temperature (nominally 300 K) up to 873 K under a field of 7.96 kA/m (100 Oe). The Curie temperature, T_C, was determined from the M vs. T curve by linear extrapolation from the region of maximum slope to the temperature axis. The temperature dependent magnetization at low temperatures was measured by SQUID in the temperature region from 10 K up to 400 K under a field of 3978.9 kA/m (50 kOe). For the measurements of temperature dependence of the first-order cubic anisotropy constant K_1, major hysteresis loops were measured at selected temperatures from 10 K up to 400 K under applied magnetic fields up to 3978.9 kA/m (50 kOe) and the closed parts of the major hysteresis loops were fitted by the law of approach (Eq. (36)).

Surface magnetic domain structures were observed by scanning probe magnetic force microscope and Kerr effect microscope for small (40 μm × 40 μm) and large (300 μm × 300 μm) areas respectively.

3.4 Magnetostriction measurement

Magnetostriction (λ) was measured by the strain gauge method. Measurements were carried out under applied fields up to 5570.4 kA/m (70 kOe) at selected temperatures from 10 K up to 400 K using a Quantum Design Physical Property Measurement System (PPMS). The magnetic field was applied parallel to the direction of strain measured (λ//). A “half bridge” configuration was used to compensate the effects of temperature and field on the strain gauge resistance, in which the second “dummy” gauge was attached to a copper reference sample. The strain gauges used for the measurements were Vishay Measurements

WK-06-031CF-350 model; gauge length = 0.79 mm, grid width = 1.57 mm, grid resistance=350.0±0.4 % ohm. M-bond 610 adhesive was used for bonding the strain gauge on the surface of samples and then the assembled samples were annealed at 150oC for 1 hour to cure the bond.

3.4.1 Half bridge configuration

Fig. 10 shows the basic Wheatstone bridge circuit with a half bridge configuration which is composed of four resistors, among which R_1 and R_2 were resistances of 350 ohm from Precision Resistive Product INC (GP1/4 model with 0.1 % resistance tolerance at 298 K), and R_3 and R_4 were resistances of the strain gauges (Vishay Measurements model WK-06-031CF-350) attached on the copper reference and the sample respectively. There are two kinds of methods to excite the circuit; one is applying a constant excitation voltage and the other is applying a constant excitation current. The conversion equation from the output data to strain depends on the excitation method, which will be discussed as follows.

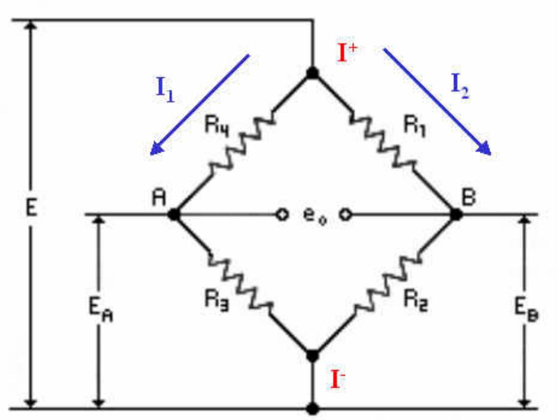

Fig. 10. Basic Wheatstone bridge circuit

3.4.1.1 Measurements under constant excitation voltage

Under a constant excitation voltage (E) applied, the output voltage (e_0) varies with the relative resistances of four resistors (R_1, R_2, R_3, R_4).

Specifically, output voltage actually depends on the resistance ratios R_1/R_2 and R_4/R_3 ;

$$\begin{aligned} E_A &= E\left(1-\frac{R_4}{R_4+R_3}\right), \qquad E_B = E\left(1-\frac{R_1}{R_1+R_2}\right) \\ e_0 &= E_A - E_B = E\left(\frac{R_1}{R_1+R_2}-\frac{R_4}{R_4+R_3}\right) \\ \frac{e_0}{E} &= \left(\frac{R_1/R_2}{R_1/R_2+1}-\frac{R_4/R_3}{R_4/R_3+1}\right) \end{aligned} \tag{70}$$

where

R_1, R_2= resistance of balancing resistors in a nominal state (for example, at 298 K under H=0)

R_3= resistance of strain gauge on the copper reference sample

R_4= resistance of strain gauge on the active test sample.

Since the resistances of the two balancing resistors R_1 and R_2 are the same ($R_1/R_2 = 1$) the output voltage e_0/E is determined by the resistance ratio (R_3/R_4);

$$\begin{aligned} \frac{e_0}{E} &= \left(\frac{R_3/R_4}{(R_3/R_4)+1}-\frac{1}{2}\right) \\ &= \left(\frac{R_{Cu}/R_T}{(R_{Cu}/R_T)+1}-\frac{1}{2}\right) \end{aligned} \tag{71}$$

where

R_{Cu} = resistance of strain gauge on the copper reference copper sample

R_T = resistance of active strain gauge on the test sample.

Since the magnetostriction of copper is negligibly small compared with that of the test sample ($\lambda_{Cu} \approx 0$ at all field strengths) it follows that $R_{Cu}(H=0) = R_{Cu}(H=H)$ so that only the resistance of the strain gauge attached on the test sample varies significantly with magnetic field H due to magnetostriction in the test sample, $R_T(H=H) = R(H=0) + \Delta R_T(H)$, so that equation (71) becomes,

$$\begin{aligned}\frac{e_0}{E} &= \left(\frac{R_{Cu}(H)/R_T(H)}{(R_{Cu}(H)/R_T(H))+1} - \frac{1}{2}\right) \\ &= \left[\frac{\dfrac{R_{Cu}(H=0)}{R_T(H=0)+\Delta R_T(H=H)}}{\dfrac{R_{Cu}(H=0)}{R_T(H=0)+\Delta R_T(H=H)}+1} - \frac{1}{2}\right]\end{aligned} \tag{72}$$

If the resistances of the strain gauges attached on Cu and the test sample are the same ($R_{Cu}(H=0)=R_T(H=0)=R$) then the above equation can be simplified to

$$\begin{aligned}\frac{e_0}{E} &= \frac{\dfrac{R}{R+\Delta R_T(H)}}{\dfrac{R}{R+\Delta R_T(H)}+1} - \frac{1}{2} = \frac{\dfrac{R}{R+\Delta R_T(H)}}{\dfrac{2R+\Delta R_T(H)}{R+\Delta R_T(H)}} - \frac{1}{2} \\ &= \frac{R}{2R+\Delta R_T(H)} - \frac{1}{2} = \frac{1}{2+\dfrac{\Delta R_T(H)}{R}} - \frac{1}{2} \\ &= \frac{1}{2+F_G\varepsilon} - \frac{1}{2} = \frac{F_G\varepsilon}{4+2F_G\varepsilon} \\ &\cong \frac{F_G\varepsilon}{4}\end{aligned} \tag{73}$$

where F_G is known as the "gauge factor" of the strain gage, $F_G = \dfrac{\Delta R/R}{\varepsilon}$ (where ε =strain). This dimensionless parameter normally has a value of about 2.

This resultant equation shows the relationship between the output voltage e_0 and the strain of the test sample ε under fixed excitation voltage E;

$$\varepsilon = \frac{4}{F_G} \cdot \frac{e_0}{E}(H). \tag{74}$$

This is the equation for the strain gauge bridge when it is operating under conditions of constant voltage.

3.4.1.2 Measurement under constant excitation current

Under a fixed excitation current (I) applied, the output "resistance" (e_0/I) varies with the relative resistances of four resistors (R_1, R_2, R_3, R_4). The current I_1 flowing through resistors R_3 and R_4 should be different from the current I_2 flowing through resistors R_1 and R_2 of the Wheatstone bridge (Fig. 10), depending on the resistances of the four resistors as follows,

$$\begin{gathered} I = I_1 + I_2 \\ \frac{I_1}{I_2} = \frac{R_1 + R_2}{R_3 + R_4}. \end{gathered} \tag{75}$$

Therefore the current flowing in each arm (I_1 and I_2) can be expressed in terms of resistances given by,

$$\begin{gathered} I_1 = \frac{R_1 + R_2}{R_1 + R_2 + R_3 + R_4} I \\ I_2 = \frac{R_3 + R_4}{R_1 + R_2 + R_3 + R_4} I. \end{gathered} \tag{76}$$

Since the output voltage (e_0) is

$$\begin{aligned} e_0 &= E_A - E_B \\ &= I_1R_4 - I_2R_1 \\ &= \left[\frac{(R_1+R_2)R_4}{R_1+R_2+R_3+R_4} - \frac{(R_3+R_4)R_1}{R_1+R_2+R_3+R_4}\right]I \end{aligned} \tag{77}$$

therefore the out of balance voltage divided by the constant current supplied to the bridge (e_0/I) can be expressed as

$$\begin{aligned} \frac{e_0}{I} &= \frac{(R_1+R_2)R_4 - (R_3+R_4)R_1}{R_1+R_2+R_3+R_4} \\ &= \frac{R_2R_4 - R_3R_1}{R_1+R_2+R_3+R_4}. \end{aligned} \tag{78}$$

When $R_3=R_{Cu}(H)$, $R_4=R_T(H)$, and $R_1=R_2=R$, the equation (78) becomes

$$\frac{e_0}{I}(H) = \frac{R\{R_T(H) - R_{Cu}(H)\}}{2R + R_T(H) + R_{Cu}(H)}. \tag{79}$$

This can be compared with equation (72).

Using the same assumption previously shown, $R_{Cu}(H=0)=R_{Cu}(H=H)=R$, and letting $R_T(H=H)=R+\Delta R_T(H)$, the equation (79) can be expressed as,

$$\begin{aligned} \frac{e_0}{I}(H) &= \frac{R[\{R+\Delta R_T(H)\} - R]}{4R + \Delta R_T(H)} \\ &= \frac{R \cdot \Delta R_T(H)}{4R + \Delta R_T(H)} \end{aligned}$$

Assuming small changes in resistance $4R+\Delta R_T(H) \cong 4R$

$$\begin{aligned} \frac{e_0}{I}(H) &\cong \frac{R \cdot \Delta R_T(H)}{4R} \\ &= \frac{\Delta R_T(H)}{4}. \end{aligned} \tag{80}$$

Since the gage factor (F_G) is

$$F_G = \frac{\Delta R/R}{\varepsilon} \tag{81}$$

therefore the output resistance becomes

$$\frac{e_0}{I}(H) = \frac{F_G R}{4} \cdot \varepsilon\,. \tag{82}$$

This resultant equation shows the relationship between the measured value (e_0/I) and the strain of the test sample ε under fixed excitation current I;

$$\varepsilon = \frac{4}{F_G R} \cdot \frac{e_0}{I}(H)\,. \tag{83}$$

This is the equation for the strain gauge bridge when it is operating under conditions of constant current. This is not the usual familiar equation for the out of balance condition of the bridge but is needed in the present work because the PPMS is configured to measure the strain gauge bridge output in this way rather than in the more conventional constant voltage configuration.

4. RESULTS AND DISCUSSION

4.1. Experimental results for Ga-substituted cobalt ferrite

4.1.1. X-ray diffraction analysis

The X-ray diffraction patterns of Ga-substituted cobalt ferrite CoGaxFe2-xO4 (x=0.0, 0.2, 0.4, 0.6, 0.8) samples are shown in Fig. 11, in which it is confirmed that all the samples have a cubic spinel structure. The typical spinel ferrites have a space group of Fd3m and the lattice parameter varies from 8.3 to 8.5 Å depending on the metal ions [36]. Fig. 6 shows the "idealized" closed packed cubic spinel structure assuming all the ions are perfect spheres. In this ideal structure the oxygen parameter u; which is the distance between the oxygen ion and the face of the cube edge along the cube diagonal of the spinel subcell, is theoretically equal to 3/8. However, the actual ionic positions in the spinel lattice are not perfectly regular as shown in Fig. 6 because the tetrahedral sites are often too small for the metal ions so that the oxygen ions around the tetrahedral sites must deviate from the theoretical positions to accommodate them, which also causes the oxygen ions around the octahedral sites to move to accommodate the expansion in tetrahedral sites. Consequently the actual ionic positions and the resulting lattice parameters should depend on the distribution of different metal ions between tetrahedral and octahedral sites. Generally the actual u parameters of ferrites are slightly larger than 3/8.

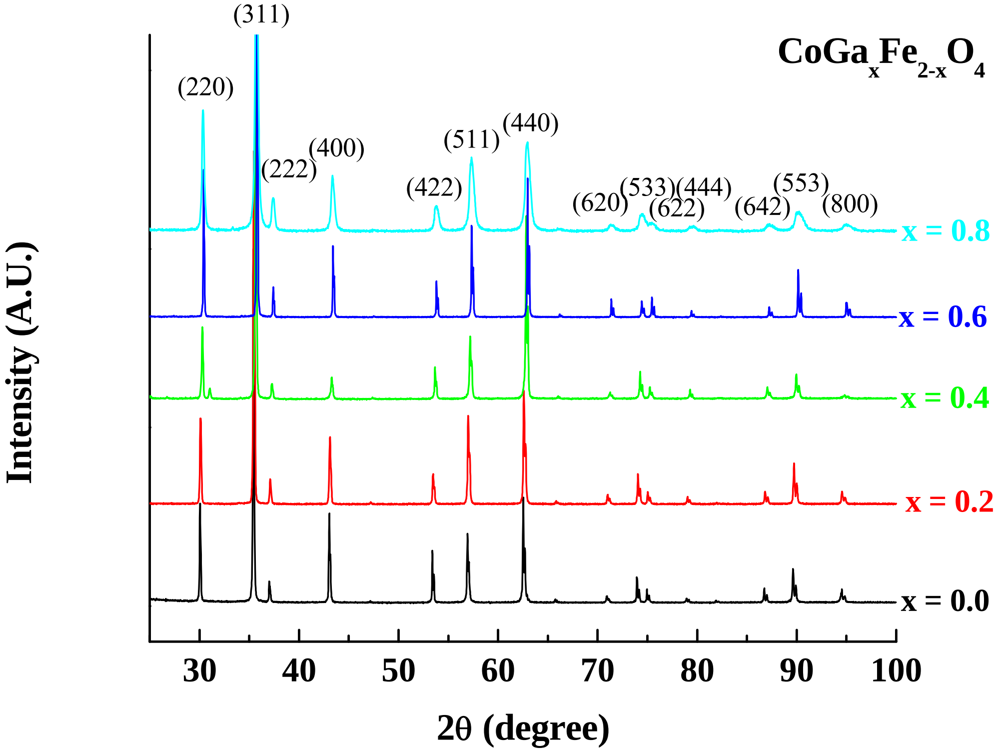

Fig. 11. X-ray diffraction patterns of Ga-substituted cobalt ferrites CoGa$_x$Fe$_{2-x}$O$_4$ (where x = 0.0 to 0.8).

4.1.2. Lattice Parameter

The lattice parameter of each sample was determined by Rietveld refinement based on X-ray diffraction data. Fig. 12 shows the observed and calculated powder diffraction patterns of $CoGa_{0.6}Fe_{1.4}O_4$. The resultant variation in lattice parameter with substituted gallium content is shown in Fig. 13, which does not appear to be a simple linear function. Based on the fact that the radius of Ga^{3+} ions in tetrahedral and octahedral sites (r_{IV} = 0.047 nm, r_{VI} = 0.062 nm) [37] is small compared to that of high spin Fe^{3+} ions in each site (r_{IV} = 0.049 nm, r_{VI} = 0.0645 nm) [37] the lattice parameter was expected to decrease as the substituted gallium content x increases assuming that it follows Vegard's law [38]. In fact, however, non-linear behavior was observed, in which lattice parameter increases from x=0 up to x=0.4 and then decreases as the gallium content increases from x=0.4 up to x=0.8, making a local maximum at x~0.4. Similar non-linear behavior in lattice parameter has been reported for the Si-substituted cobalt ferrites $Co_{1+x}Si_xFe_{2-2x}O_4$ [39], in which the maximum value of lattice parameter was observed at the sample of x ~ 0.2 Si content. It was mentioned [39] that this non-linear behavior had been reported for systems which were not completely normal or inverse, however, the reason for this non-linear behavior has not been clearly explained so far. One possible explanation for this phenomenon may be the following. As mentioned before the Co^{2+} ions should be distributed between tetrahedral and octahedral sites in pure cobalt ferrite, with the actual site occupancy depending on the details of the fabrication process. Thus some of the tetrahedral sites were initially occupied by Co^{2+} ions. Since the radius of Co^{2+} ions in tetrahedral sites (r_{IV} = 0.038 nm) [37] is small compared to that of Ga^{3+} ions in tetrahedral sites (r_{IV} = 0.047 nm) [37] the lattice parameter should increase as the substituted Ga^{3+} ions replaced the Co^{2+} ions in tetrahedral sites. After all of the Co^{2+} ions in tetrahedral sites were replaced by Ga^{3+} ions then Fe^{3+} ions would be replaced by further substituted Ga^{3+} ions, whether Ga^{3+} ions substitute into tetrahedral or octahedral sites, which could cause the lattice parameter to decrease with the content of Ga^{3+} ions.

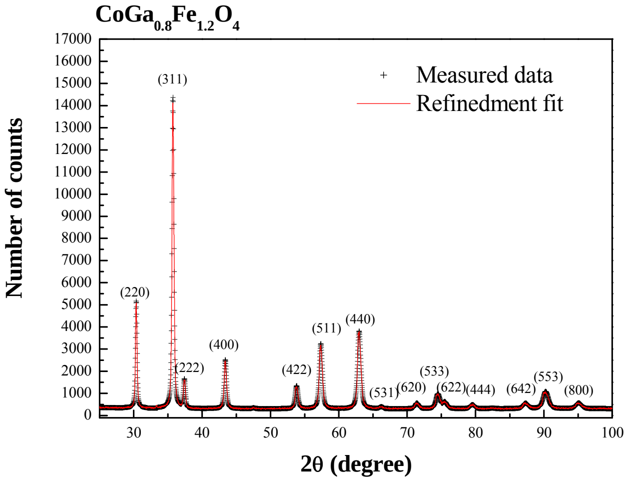

Fig. 12. Observed and calculated x-ray diffraction patterns of $CoGa_{0.6}Fe_{1.4}O_4$.

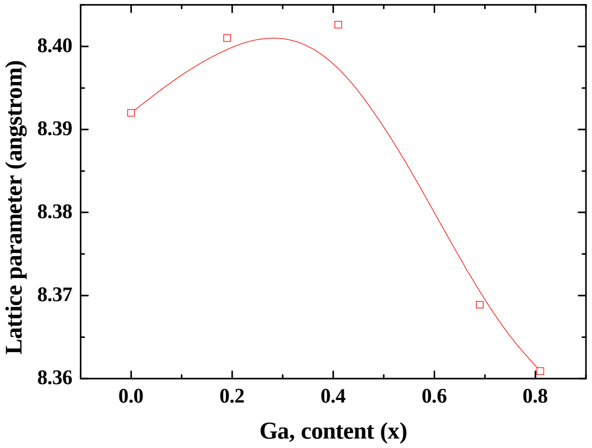

Fig. 13. Lattice parameters of $CoGa_xFe_{2-x}O_4$ (where x=0.0 to 0.8).

4.1.3. SEM and EDX analysis

The comparison of target and final compositions of sintered samples is shown in Table. III. The final composition was determined from the measurements at more than 5 different positions in each sample. Scanning electron microscopy (SEM) investigations showed that all the sintered samples had a homogeneous microstructure with similar grain sizes of the order of 10 µm (Fig. 14)

Table III. Target compositions of a series of Ga-substituted cobalt ferrite samples, and the final compositions determined by energy-dispersive x-ray spectroscopy (EDX) in an SEM

Target composition	Final composition by EDX		
	Fe	Co	Ga
$CoFe_{2.0}O_4$	2.05	0.95	—
$CoGa_{0.2}Fe_{1.8}O_4$	1.81	1.00	0.19
$CoGa_{0.4}Fe_{1.6}O_4$	1.55	1.04	0.41
$CoGa_{0.6}Fe_{1.4}O_4$	1.33	0.98	0.69
$CoGa_{0.8}Fe_{1.2}O_4$	1.15	1.04	0.81

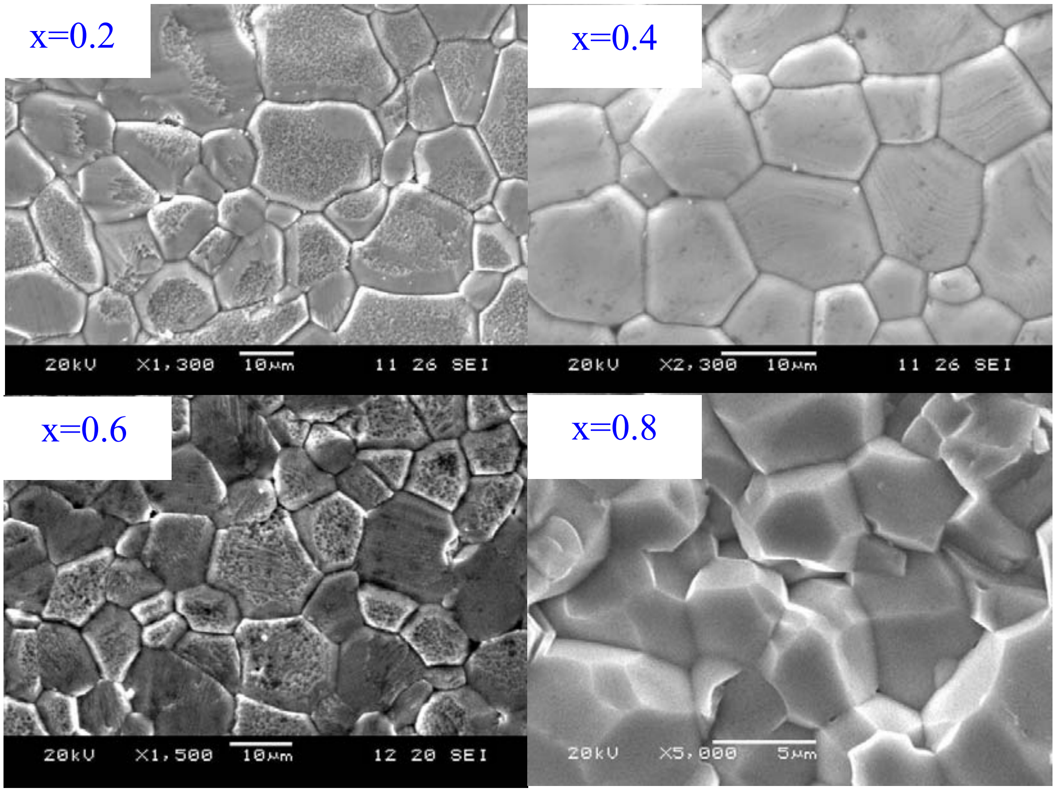

Fig. 14. SEM images of Ga-substituted cobalt ferrites $CoGa_xFe_{2-x}O_4$ (where x=0.2 to 0.8).

4.1.4. Curie temperature

The temperature dependent magnetizations of Ga substituted cobalt ferrite $CoGa_xFe_{2-x}O_4$ samples are shown in Fig. 15 (a). From the M vs T curves, it was evident that the Curie temperature T_C was reduced by substitution of Ga for Fe (Fig. 15 (b)). This is considered to be due to reduction in exchange interaction caused by Ga substitution. A similar effect has been observed when substituting Mn or Cr for Fe in cobalt ferrite [7, 9]. In fact, T_C decreases at a greater rate with Ga substitution than with Mn or Cr substitution. This can perhaps be understood based on the fact that tetrahedral sites have a higher number of nearest neighbor cations than octahedral sites (Fig. 7). Thus the change in interaction energy caused by substitution at the tetrahedral site may be expected to be larger than at the octahedral sites.

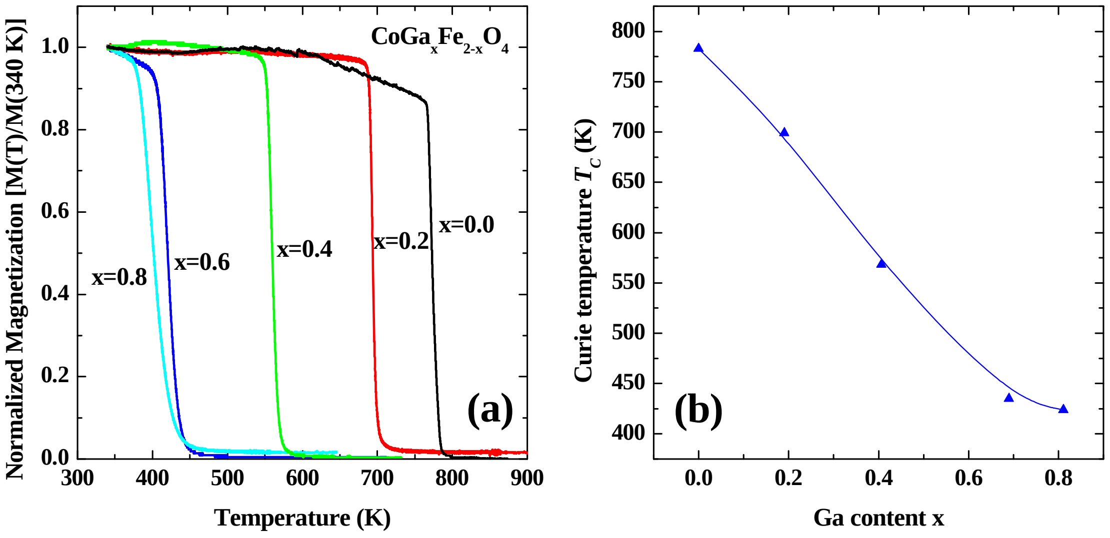

Fig. 15 (a) Temperature dependent normalized magnetization relative to value of 340 K and (b) Curie temperatures T_C of $CoGa_xFe_{2-x}O_4$ samples as a function of the substituted content x.

4.1.5 Hysteresis curve

Fig. 16 and 17 show the variation in M vs H with gallium content measured at various temperatures from 10 K to 400 K. As temperature increased the hysteresis curves for all the samples with various gallium contents altogether became softer over the whole range of temperatures. Both the magnetic remanence ratio M_R/M_S and coercive force H_C decreased with temperature as shown in Fig. 18 (a) and (b) respectively. For a selected temperature samples with higher gallium content x showed lower M_R/M_S and H_C except for those at 200 K. Interestingly the x=0.6 and 0.8 Ga samples showed a local maximum in H_C only at this selected temperature. The saturation magnetization M_S and the absolute magnitude of the first-order cubic anisotropy constant $|K_1|$ were determined by fitting the hysteresis loops based on the law of approach to saturation (see section 2.1.6.2). For the fitting process magnetization curves with fields higher than 1 T (796 kA/m) were used for the high temperature range above 150 K. For low temperature range below 150 K, only the parts of the magnetization curves with higher than 2.5 T (1990 kA/m) were used for the fitting. The resultant values of M_S and K_1 as a function of temperature for the samples with various gallium contents are shown in Fig. 15 (c) and (d) respectively. The saturation magnetization M_S of all samples on a whole decreased as temperature increased. The small increase in M_S below 150 K with temperature for the pure cobalt ferrite and x=0.2 Ga samples is considered due to the fact that even the highest field of 5 T in these measurements could not saturate the samples. This can also explain the similar behavior in K_1 below 150 K for pure cobalt ferrite and that below 50 K for x=0.2 Ga sample. For fixed values of temperature, even though there was still existing inaccuracy in values below 150 K due to non-saturation, it looks that x=0.2 and 0.4 Ga samples showed higher values of M_S than pure cobalt ferrite, which is consistent with the expected Ga^{3+} ion's preference for tetrahedral sites. For x=0.6 and 0.8 Ga samples the values of M_S are very close each other comparing with those of x=0.2 and 0.4 Ga samples which have much higher values of M_S over the whole temperature range. There are two possible explanations for this. The first is that as the content of Ga^{3+} ions increased, Ga^{3+} ions occupied tetrahedral sites up to x=0.4, above which Ga^{3+} ions started to substitute into octahedral sites rather than tetrahedral sites. The other explanation is that the substitution of Ga^{3+} ions changed the exchange interactions among A-A, B-B, and A-B sub-lattices so that as the content of Ga^{3+} ions increased the directions of the magnetic moments in A and B sites may have changed.

The calculated $|K_1|$ plotted as a function of temperature also showed very similar behavior with M_S. Just like the results of M_S, the values of K_1 of two pairs of x=0.2 and 0.4 Ga samples and x=0.6 and 0.8 Ga samples were very close to each other respectively, however, there existed a big difference in behavior of $|K_1|$ with temperature between the two pairs. This can be explained by the same interpretation for the results of lattice parameter variance with x (Fig. 13), from which abrupt change between the two pairs of samples was considered to be related to cations distribution between tetrahedral and octahedral sites. Using the same assumption that the substitution of Ga^{3+} ions on tetrahedral sites up to x=0.4 causes more of the Co^{2+} ions to be located at the octahedral sites, the enhanced values of K_1 for the x=0.2 and 0.4 Ga samples can be understood based on the single ion anisotropy theory (see section 2.2.3).

As observed in the H_C vs T curves a sudden change in $|K_1|$ for the x=0.6 and 0.8 Ga samples was observed between 150 K and 200 K. This change in behavior around 200 K was also observed more clearly in the results of magnetostriction measurements. As will be discussed in the following chapter this phenomena is considered to be caused by the change of sign in K_1 around 200 K. Considering the fact that only the absolute magnitude of $|K_1|$ can be obtained by using law of approach to saturation the abrupt change in $|K_1|$ around 200 K calculated by this method might be an indicative of the change in sign of K_1 near that temperature.

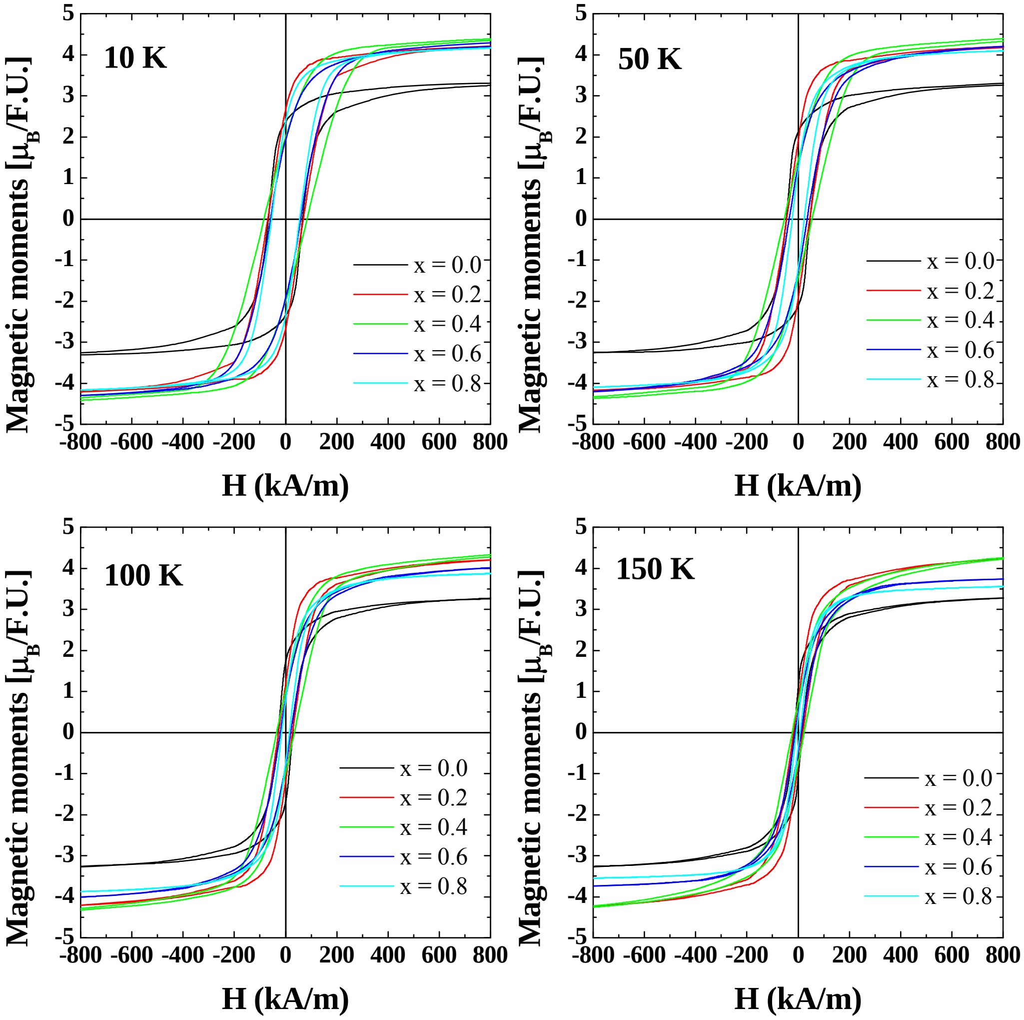

Fig. 16. Magnetization (M) vs magnetic field (H) curves for $CoGa_xFe_{2-x}O_4$ samples (where x=0.0 to 0.8) measured at 10 K, 50 K, 100 K, and 150 K.

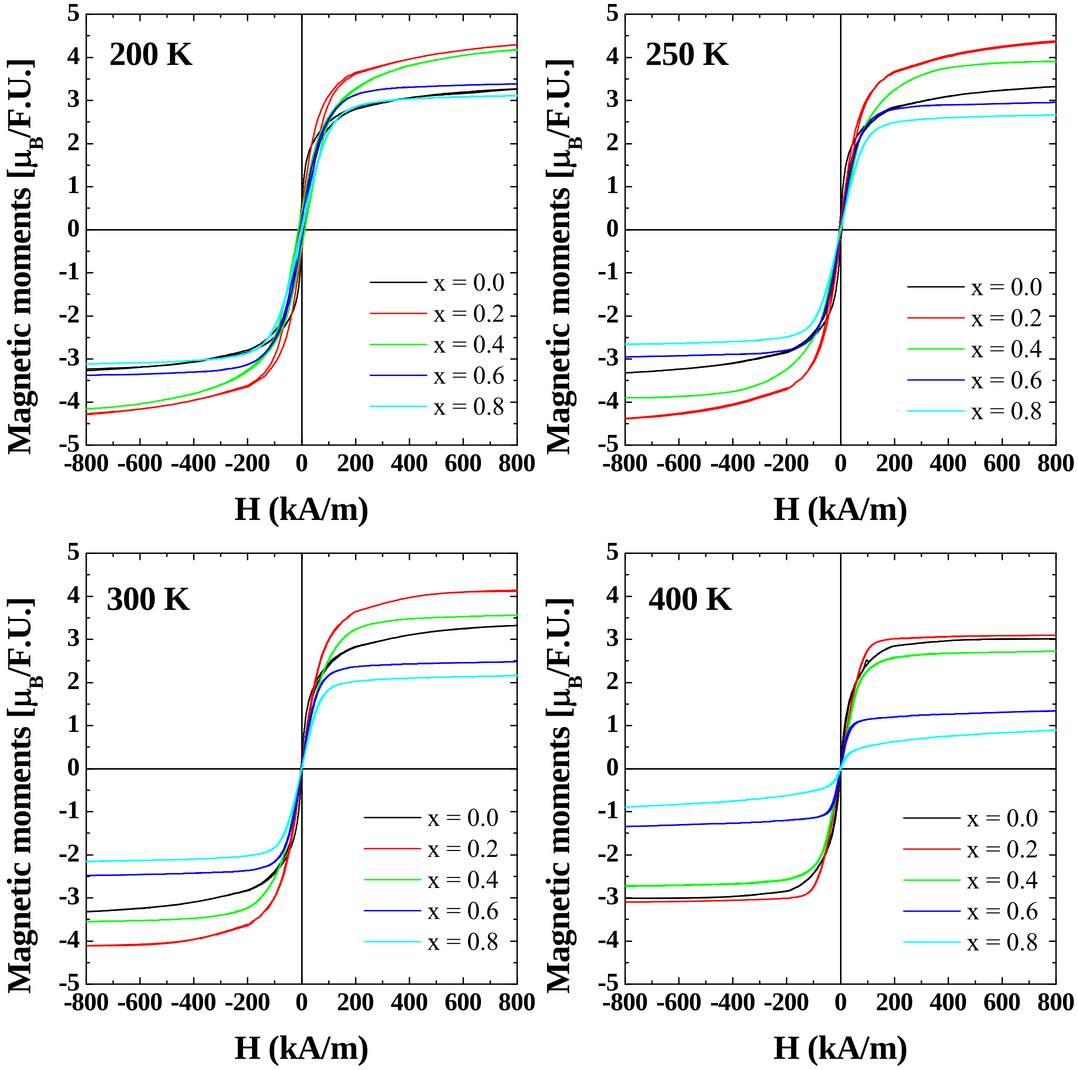

Fig. 17. Magnetization (M) vs magnetic field (H) curves for $CoGa_xFe_{2-x}O_4$ samples (where x=0.0 to 0.8) measured at 200 K, 250 K, 300 K, and 400 K.

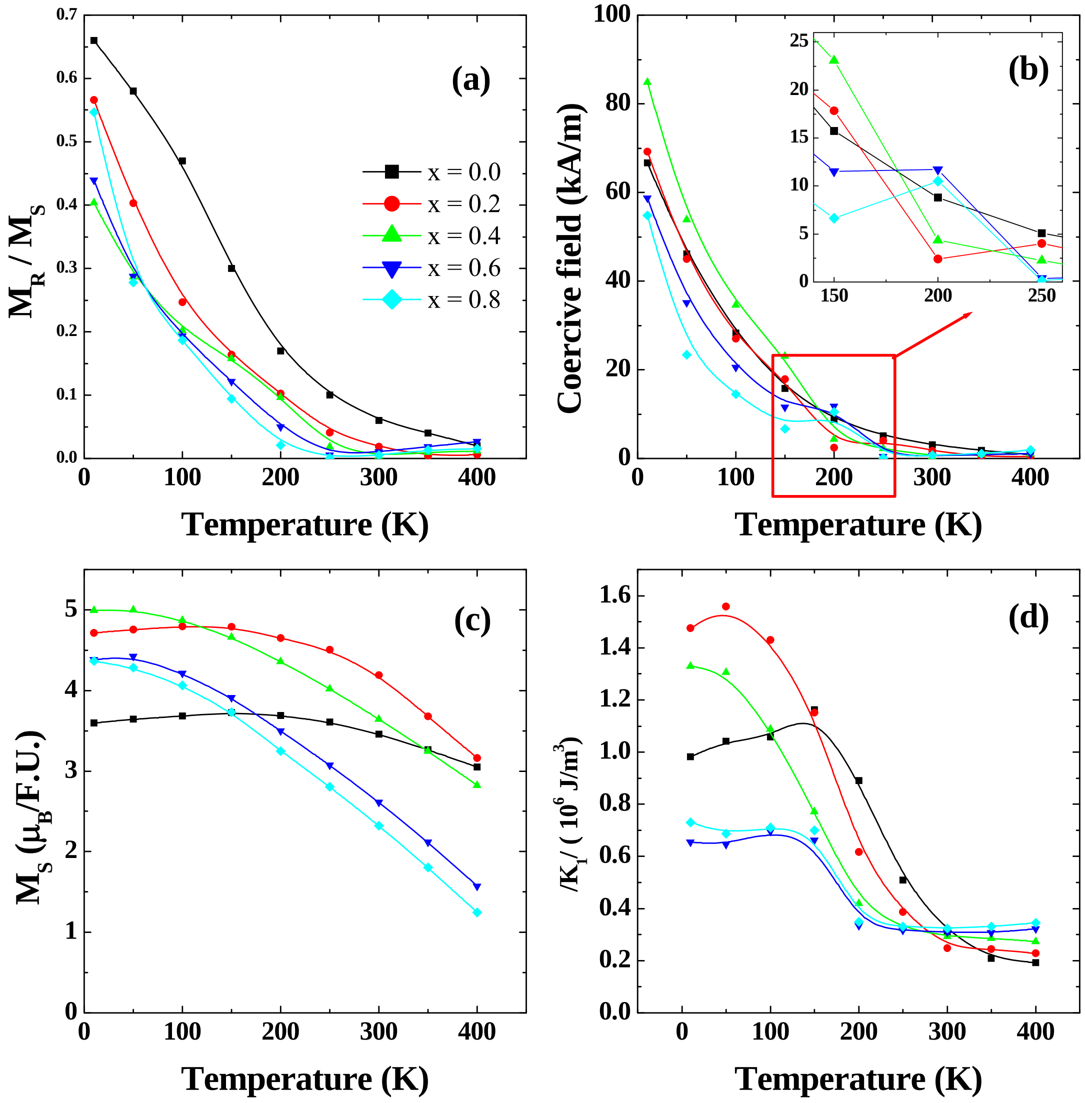

Fig. 18. (a) Magnetic remanence (M_R/M_S) and (b) coercive field (H_C) as a function of temperature for $CoGa_xFe_{2-x}O_4$ samples (where x=0.0 to 0.8). Temperature dependences of (c) the saturation magnetization M_S and (d) the absolute magnitude of first-order cubic anisotropy constant $|K_1|$ were determined by fitting the major hysteresis loops based on the law of approach to saturation**.**

4.1.6. Magnetostriction

For polycrystalline cubic materials with randomly oriented crystallites the saturation magnetostriction λ_S as discussed in section 2.1.7.1 can be expressed by,

$$\lambda_s = \frac{2}{5}\lambda_{100} + \frac{3}{5}\lambda_{111} \tag{84}$$

assuming that the materials have isotropic elastic properties. Even for the materials with isotropic elastic properties this equation is valid only when the materials are in a magnetically saturated state. There has been no general formulated equation reported for the magnetostriction of non-saturated magnetic state. For the cobalt ferrite based materials, as shown previously in the hysteresis loops (Fig. 16 and 17), the anisotropy energy was too large to saturate even under the highest magnetic field of $\mu_0H=5$ T using our experimental equipment. With respect to this it was necessary to create some terminologies to determine the magnitudes in magnetostriction of the samples in non-saturated states. Fig. 19 shows the magnetostriction (λ) vs magnetic field (H) curve of pure cobalt ferrite $CoFe_2O_4$ sample measured at 10 K. The values of magnetostriction were determined by selecting the first measured data point under zero field (H=0) as the initial state (strain=0). Since the magnetostriction even at zero applied magnetic field (H=0) can vary because of the various possible domain structures even in the demagnetized state (see section 2.1.7) new terminologies were created as λ_{Max}, λ_{Min}, and λ_{Rem}, which are indicated by arrows in Fig. 19, to quantify the values of magnetostriction conveniently. Using these characteristic values of strain it was possible to compare the magnetoelastic properties for different samples.

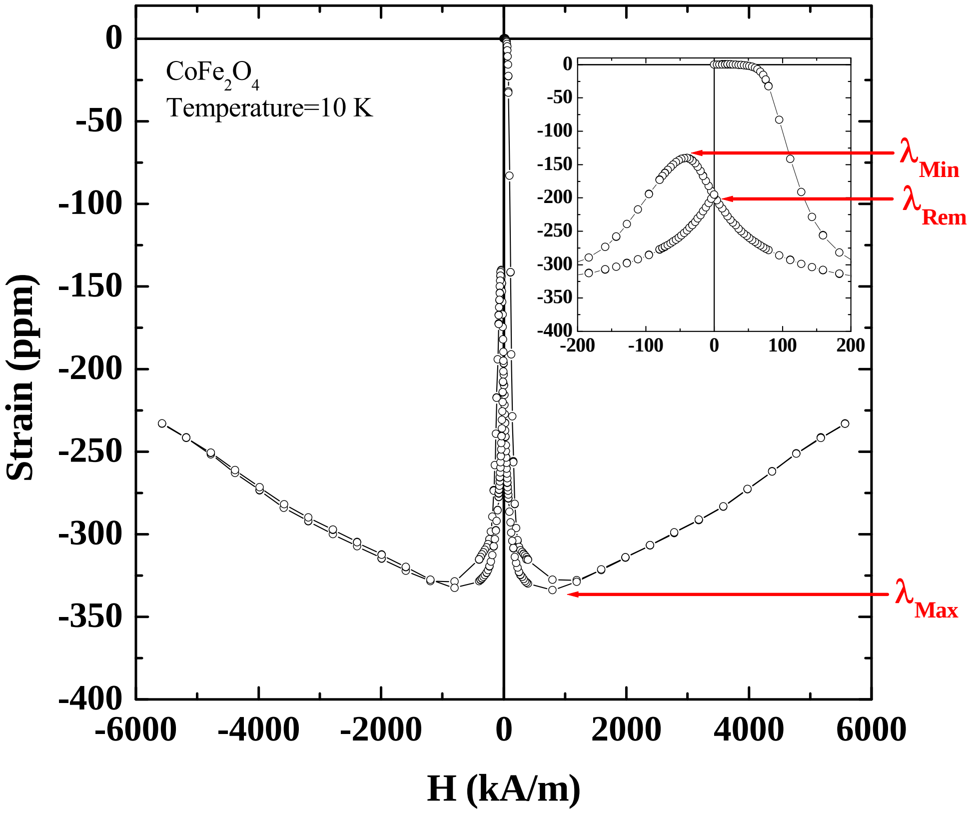

Fig. 19. Magnetostriction (λ_H) vs magnetic field (H) of cobalt ferrite $CoFe_2O_4$ measured at 10 K. Inset is an enlarged part of the low magnetic fields region. The measured strains were plotted with the relative values from the starting data point as zero strain. Data points corresponding to the defined terminologies λ_{Max}, λ_{Min}, and λ_{Rem} are indicated by arrows.

Fig. 20 and 21 show the λ_H-λ_{Min} vs magnetic field (H) curves for $CoGa_xFe_{2-x}O_4$ samples (where x=0.0 to 0.8) measured at the same temperatures that were selected for hysteresis loops measurements. Gallium substitution was found to have a strong effect on magnetostriction. Generally the magnitude of magnetostriction decreased with increasing Ga content from x=0.2 to 0.8 over the whole range of temperatures. The magnetostriction for low values of x (x = 0.0, 0.2 and 0.4) showed negative magnetostriction over the entire temperature range, while that of high values of x (x=0.6 and 0.8) showed complicated behavior as temperature changes. This is indicative of different signs for the two cubic magnetostriction coefficients (λ_{100} and λ_{111}). For pure cobalt ferrite it was well known that $\lambda_{100} < 0$ and $\lambda_{111} > 0$, and that the absolute magnitude is $|\lambda_{100}| > |\lambda_{111}|$ [30]. Positive value of K_1 for cobalt ferrite have been explained by single ion anisotropy theory (see chapter (2.2.3). Therefore the negative magnetostriction for low values of x samples can be understood by the same reasoning.

For x = 0.6 and x = 0.8 samples the signs of the magnetostriction changed with temperature. At the low temperature region below 200 K, the slope of magnetostriction $d\lambda/dH$ changed from negative to positive as field increased, which is indicative of positive K_1 (<100> easy axes) in this temperature range (Fig. 22) assuming that the signs of λ_{100} and λ_{111} were not changed by the Ga-substitution. At the high temperature range above 200 K, however, the slope $d\lambda/dH$ changed from positive to negative as field increased, which indicates that the anisotropy constant K_1 changed its sign to be negative so that the <111> directions became the easy axes (Fig. 23). These results are consistent with those of magnetization measurements, in which there observed a sudden change in H_C and K_1 around 200 K too (Fig. 18).

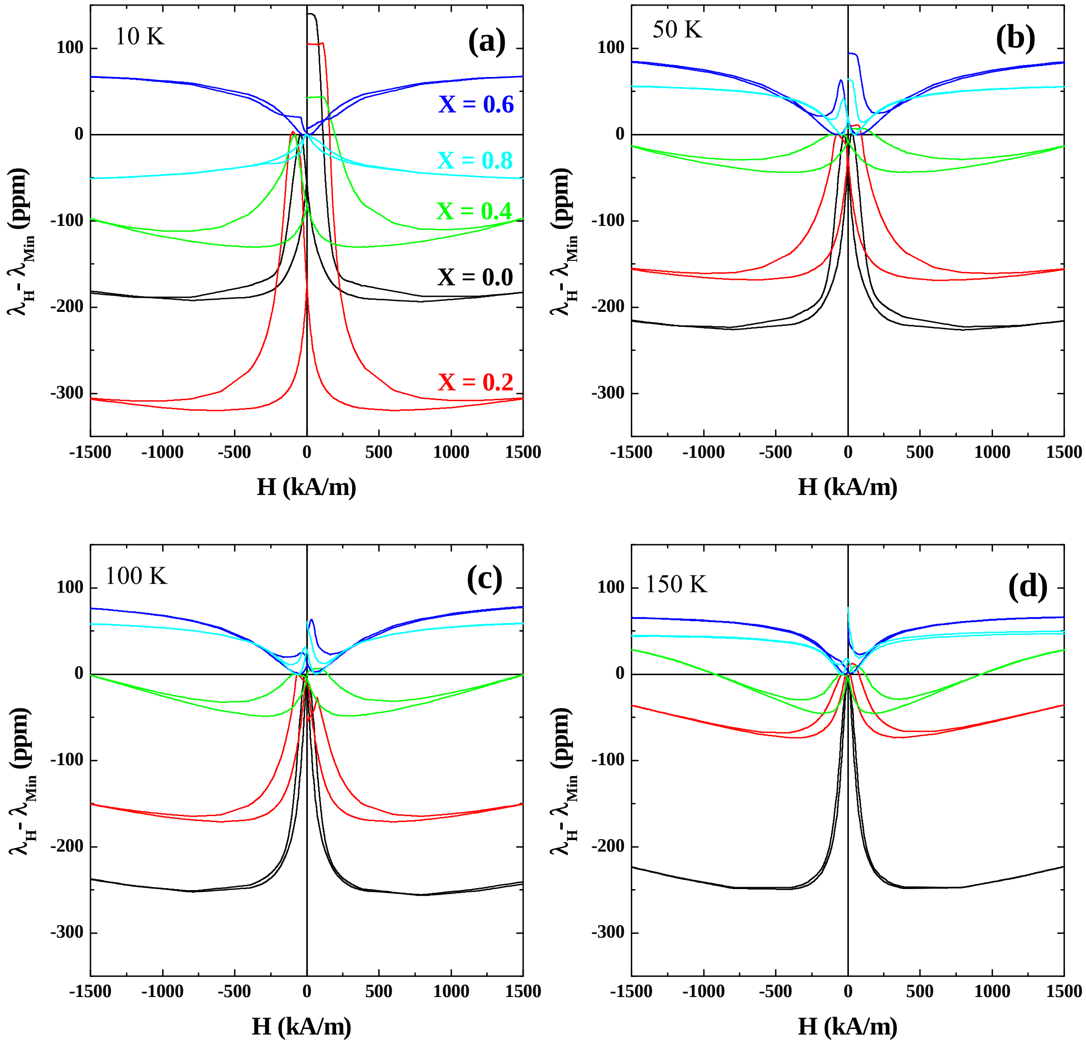

Fig. 20. Magnetostriction (λ_H-λ_{Min}) vs magnetic field (H) curves for $CoGa_xFe_{2-x}O_4$ samples (where x=0.0 to 0.8) measured at 10 K, 50 K, 100 K, and 150 K.

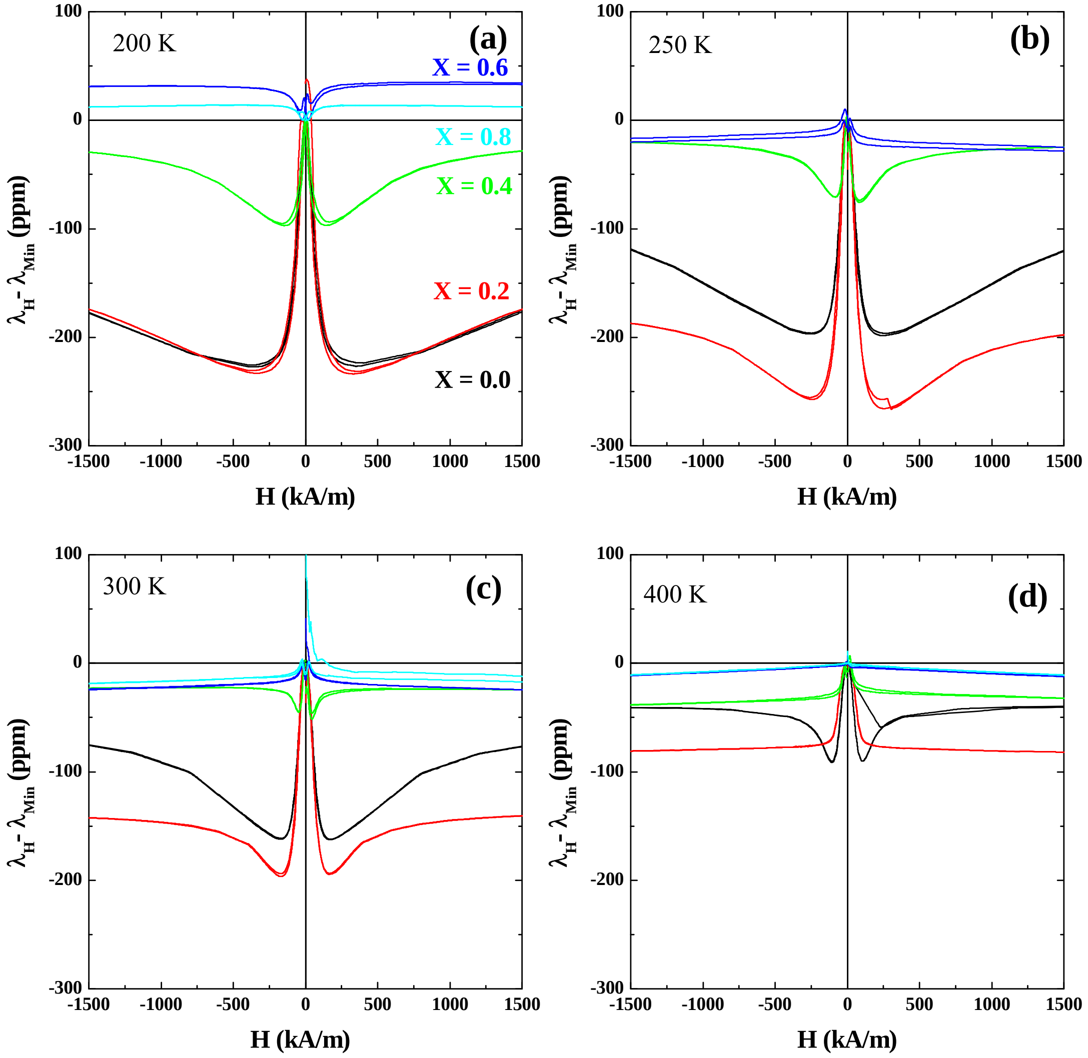

Fig. 21. Magnetostriction (λ_H-λ_{Min}) vs magnetic field (H) curves for $CoGa_xFe_{2-x}O_4$ samples (where x=0.0 to 0.8) measured at 200 K, 250 K, 300 K, and 400 K.

With respect to the sensor application λ_{Rem} should be an important characteristic value of materials because the remanence magnetic state should probably be the most useful magnetic state of the material in real applications. For this reason, the values of λ_H-λ_{Rem} were taken from the magnetostriction curves of various Ga contents x and compared to each other by plotting those in the same graphs as shown in Fig. 22 and 23. At the temperature range below 200 K the maximum magnetostriction was observed in the pure cobalt ferrite (x=0.0), however, at temperatures above 200 K the maximum magnetostriction was observed in x=0.2 Ga sample. Considering that the conventional applications should usually happen at room temperature (~300 K) this enhanced magnitude in magnetostriction by Ga-substitution measured at 300 K is a promising result. Moreover, it is worth mentioning the notable result that the values of strain derivative $d(\lambda_H-\lambda_{Rem})/dH$, which is one of the most important factors in sensor applications (see section 2.3), were also increased by a small amount of Ga-substitution for Fe (e.g. $CoGa_{0.2}Fe_{1.8}O_4$) at 300 K as shown in Fig. 24 and 25. Similar behavior of enhanced strain derivative $d(\lambda_H-\lambda_{Rem})/dH$ has been observed in recent studies of Mn- and Cr-substituted cobalt ferrites $CoMn_xFe_{2-x}O_4$ and $CoCr_xFe_{2-x}O_4$ [7, 9]. The systematic comparison among these materials will be discussed in the following chapters.

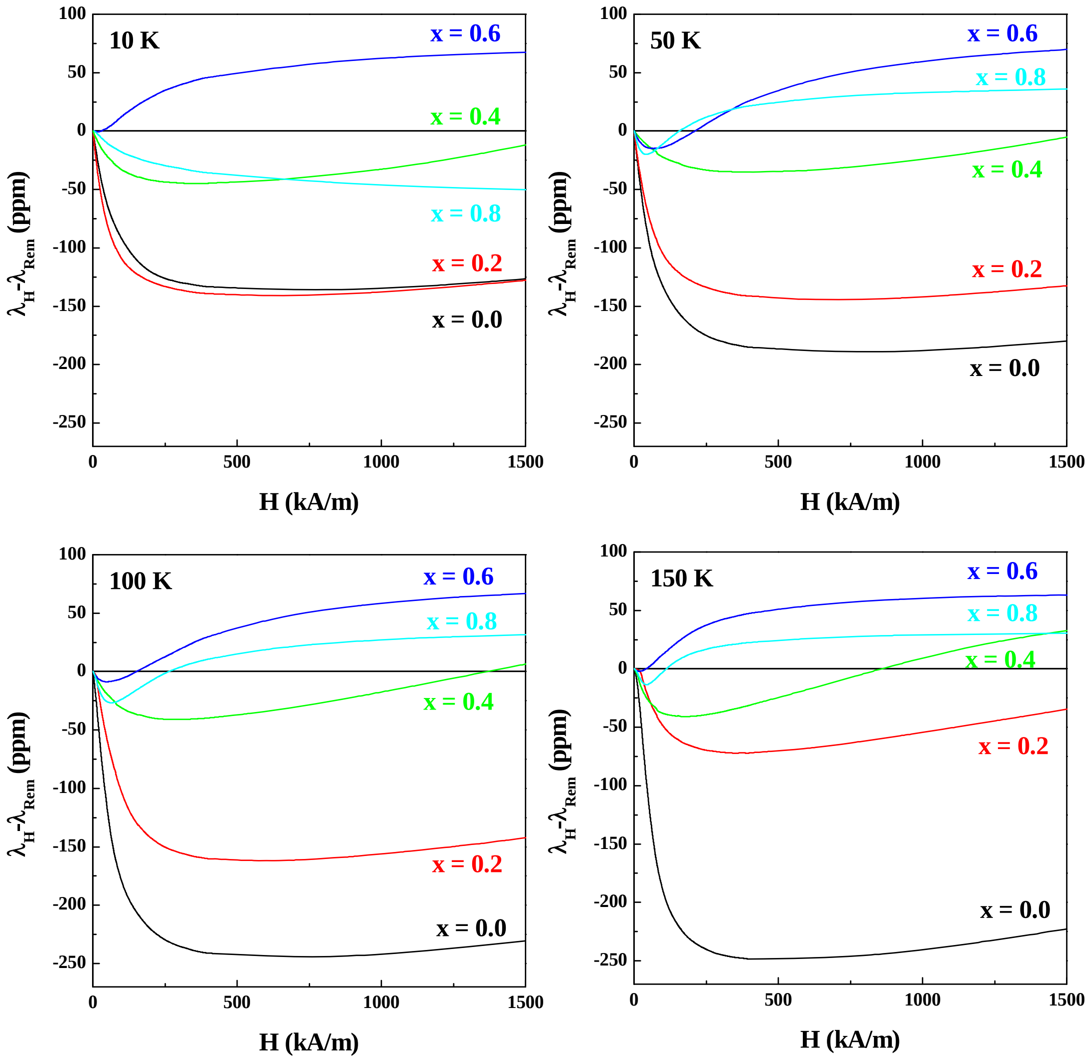

Fig. 22. Magnetostriction (λ_H-λ_{Rem}) vs magnetic field (H) curves for $CoGa_xFe_{2-x}O_4$ samples (where x=0.0 to 0.8) measured at 10 K, 50 K, 100 K, and 150 K.

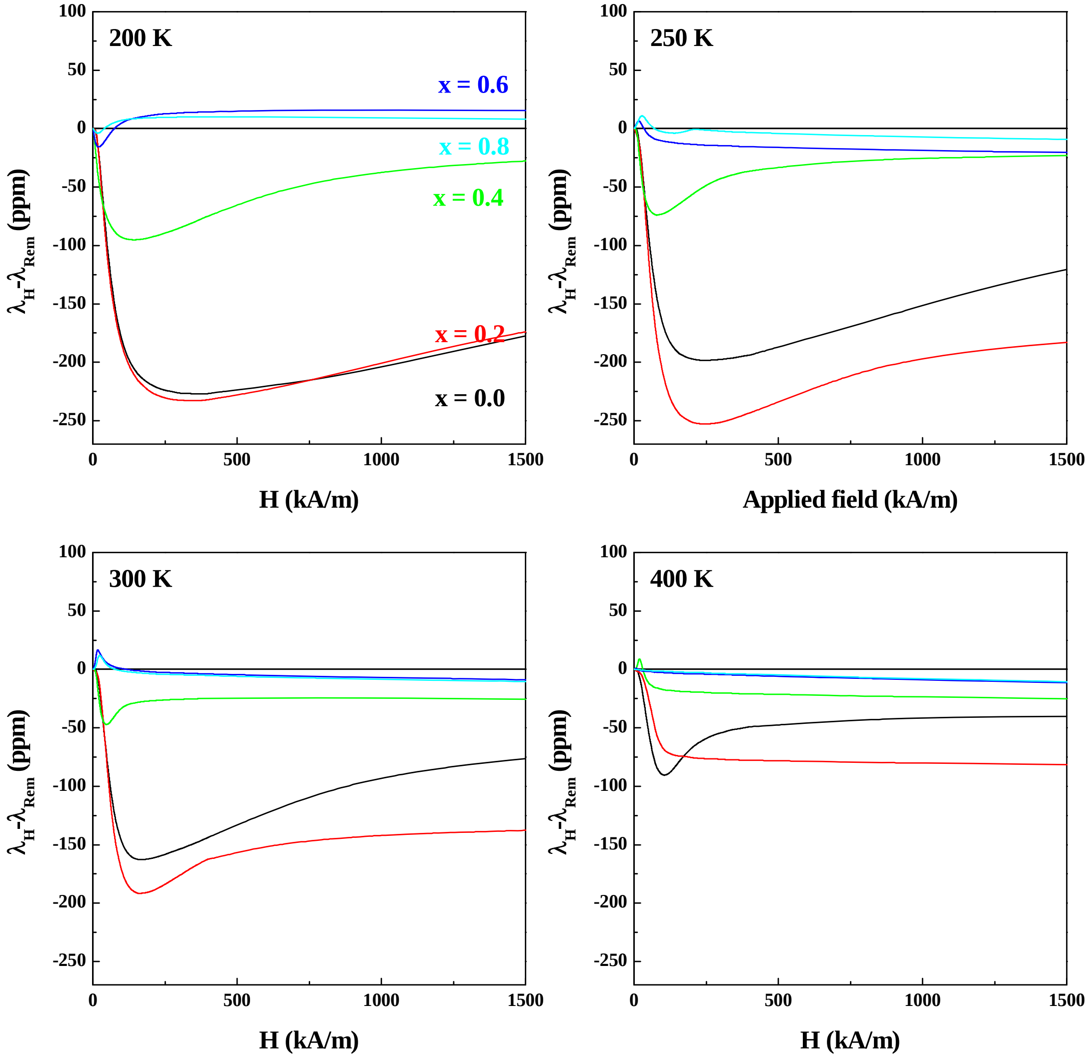

Fig. 23. Magnetostriction (λ_H-λ_{Rem}) vs magnetic field (H) curves for $CoGa_xFe_{2-x}O_4$ samples (where x=0.0 to 0.8) measured at 200 K, 250 K, 300 K, and 400 K.

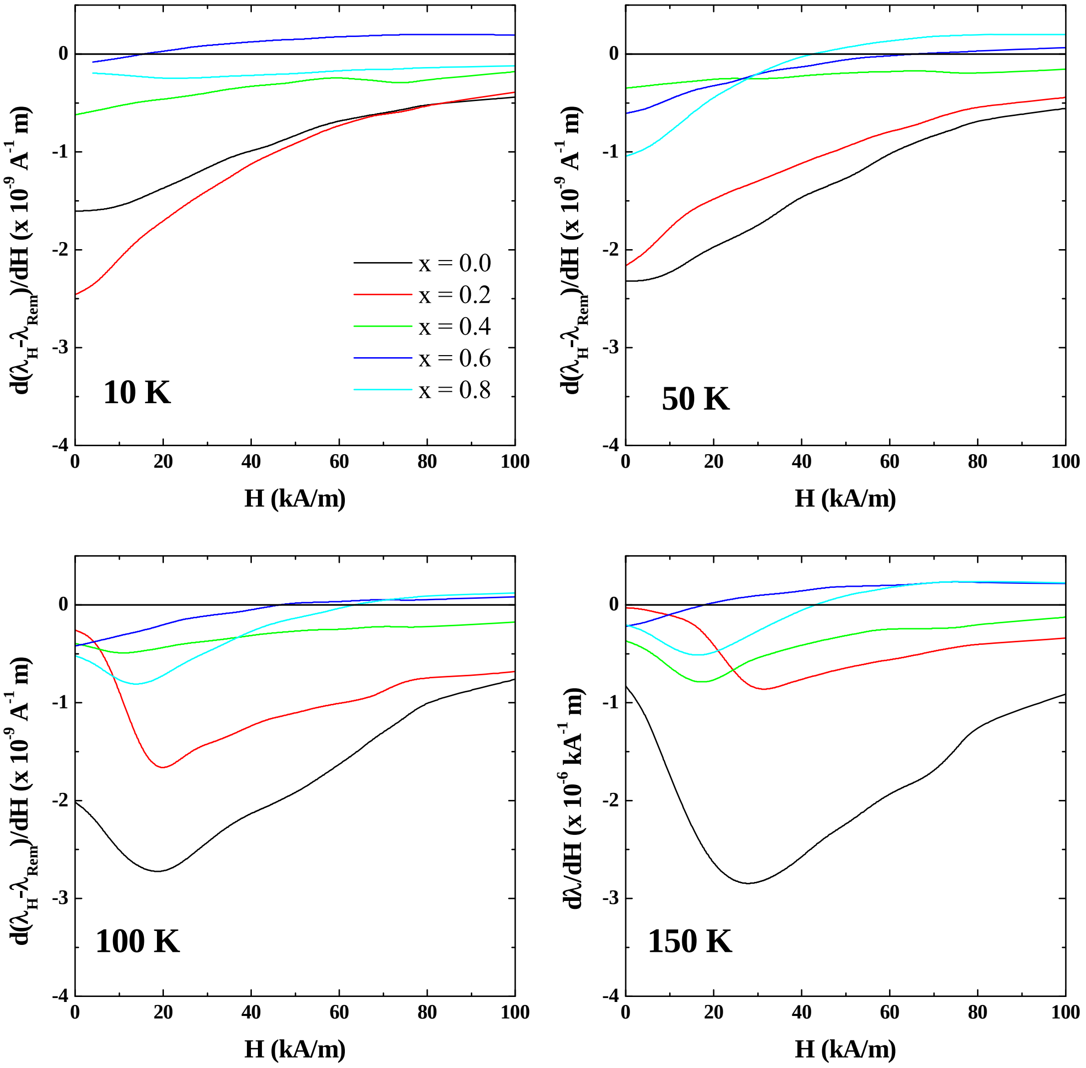

Fig. 24. Magnetostriction derivatives $d(\lambda_H-\lambda_{Rem})/dH$ vs magnetic field (H) curves for $CoGa_xFe_{2-x}O_4$ samples (where x=0.0 to 0.8) measured at 10 K, 50 K, 100 K, and 150 K.

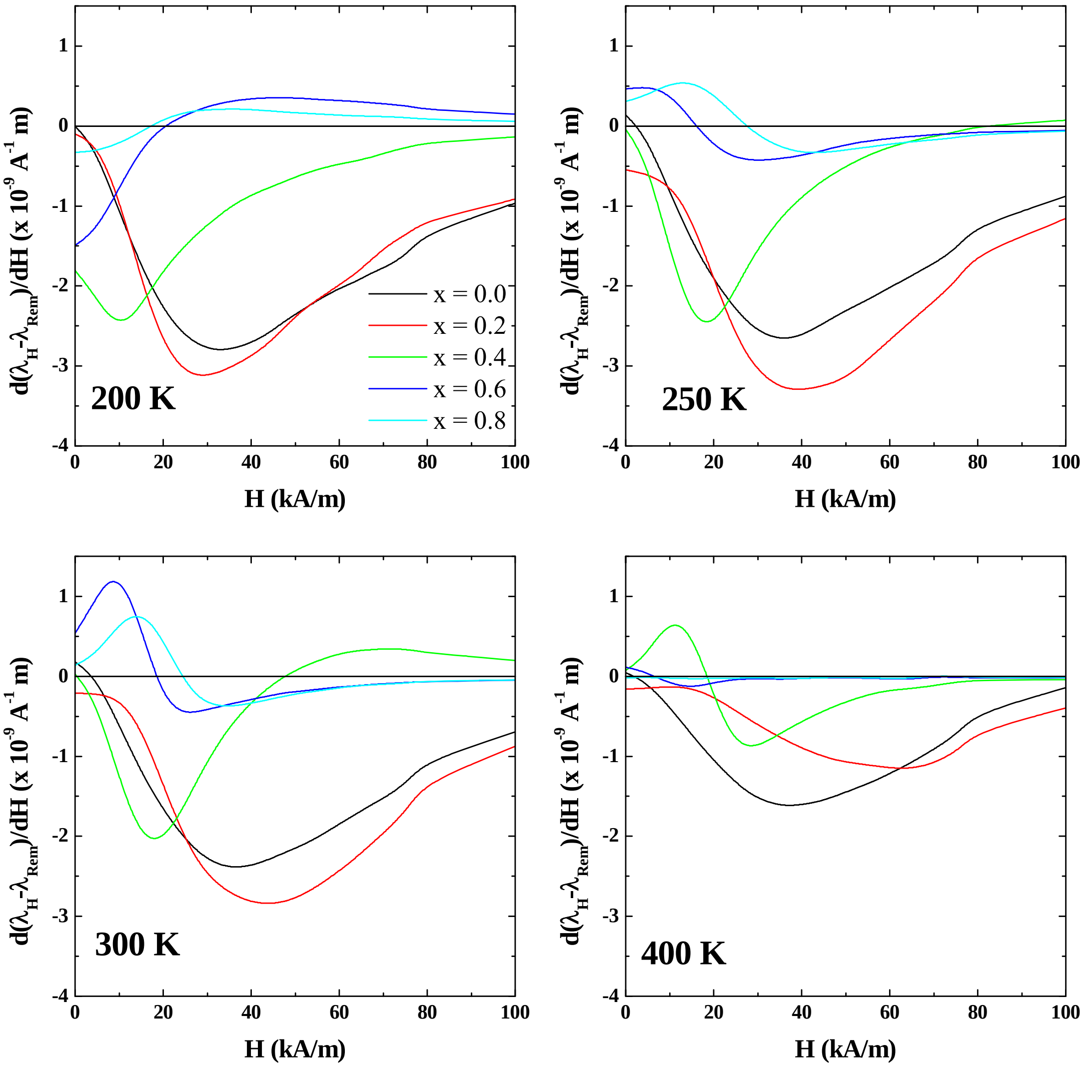

Fig. 25. Magnetostriction derivatives d(λ_H-λ_{Rem})/dH vs magnetic field (H) curves for CoGa$_x$Fe$_{2-x}$O$_4$ samples (where x=0.0 to 0.8) measured at 200 K, 250 K, 300 K, and 400 K.

In order to investigate the variation in maximum values of $(\lambda_H - \lambda_{Rem})_{Max}$ and its derivatives $[d(\lambda_H - \lambda_{Rem})/dH]_{Max}$ with temperature these values were plotted as a function of temperature as shown in Fig. 26 and 27. For low values of x (x = 0.0 and 0.2) the behaviors in $[\lambda_H - \lambda_{Rem}]_{Max}$ were similar to each other over the whole temperature range except for at 150 K where x=0.2 Ga sample showed abrupt decrease in magnitude. Based on the fact that the total magnetostriction is determined by the relative values of λ_{100} and λ_{111}, and each magnitude should have different temperature dependence, it can be deduced that any of these two magnetostriction coefficients (or both of them) changed significantly at 150 K. Similar behavior was also observed in the maximum slope of magnetostriction as shown in Fig. 27, in which the smallest magnitude of 0.9 in

$[d(\lambda_H - \lambda_{Rem})/dH]_{Max}$ was observed at 150 K. In the case of x=0.6 and 0.8 Ga samples both samples showed the change in sign of magnetostriction from positive to negative values as temperature increased from 200 K to 250 K. Since the magnetostriction curves of these samples look saturated in this temperature range (200 K and 250 K) the change in sign of the maximum magnetostriction should be due to the change in the magnitude of λ_{100} and λ_{111} - $|\lambda_{100}| < 1.5\ |\lambda_{111}|$ at low temperatures and $|\lambda_{100}| > 1.5\ |\lambda_{111}|$ at high temperatures - because equation (84) should be valid in the saturated state for these samples. The temperature dependence of $[d(\lambda_H - \lambda_{Rem})/dH]_{Max}$ for x=0.6 and 0.8 was not included in Fig. 27 because the sign of the slope was changed with field even at fixed temperatures for these samples.

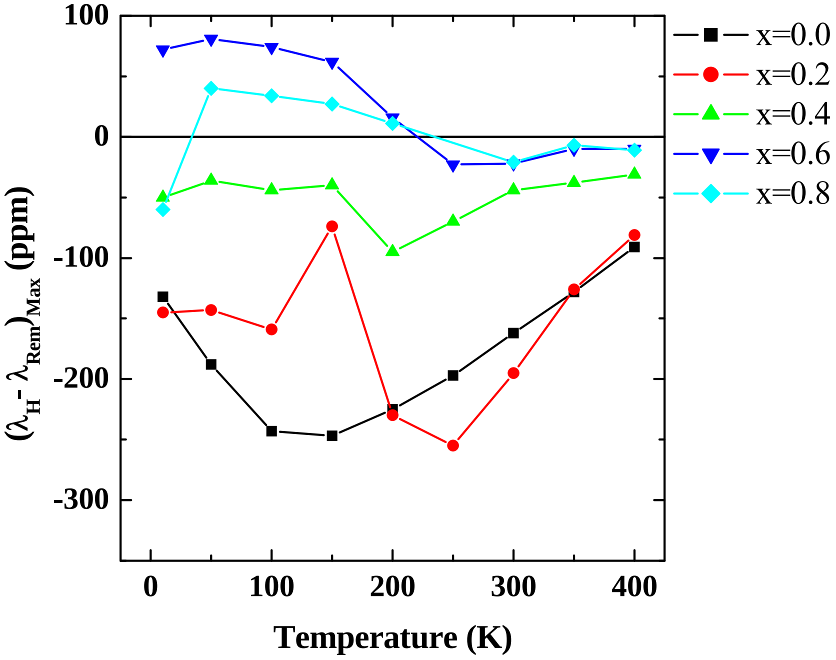

Fig. 26. Maximum magnetostriction $(\lambda_H-\lambda_{Rem})_{Max}$ of $CoGa_xFe_{2-x}O_4$ samples (where x=0.0 to 0.8) measured at various temperatures.

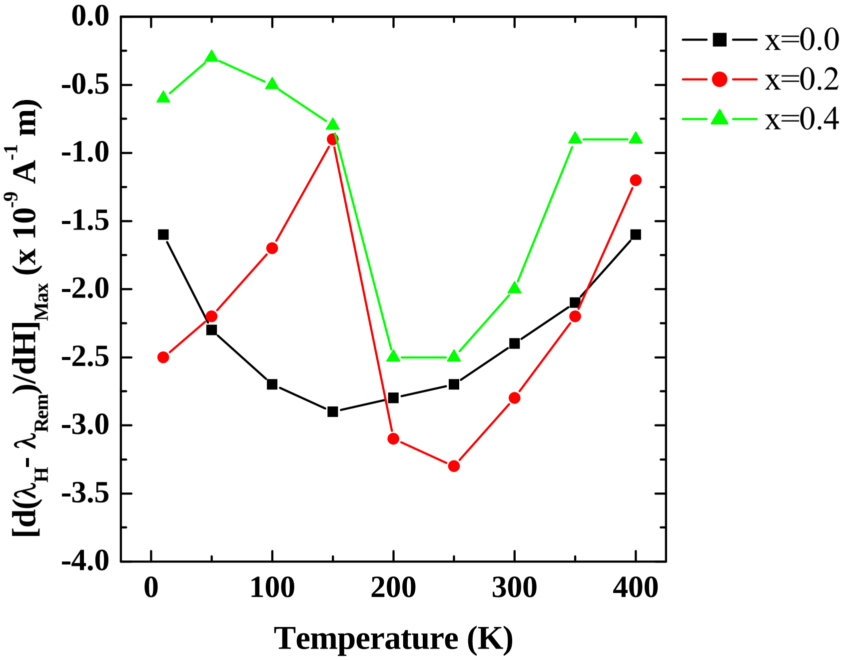

Fig. 27. Maximum magnetostriction derivatives $[d(\lambda_H-\lambda_{Rem})/dH]_{Max}$ of $CoGa_xFe_{2-x}O_4$ samples (where x=0.0 to 0.8) at various temperatures

4.2. Experimental results for Ge-substituted cobalt ferrite

4.2.1. X-ray diffraction analysis

The X-ray diffraction patterns of Ge-substituted cobalt ferrite $Co_{1+x}Ge_xFe_{2-2x}O_4$ (x=0.0, 0.1, 0.2, 0.4, 0.6) samples are shown in Fig. 28, in which it is confirmed that all the samples have a cubic spinel structure. The observed and calculated powder diffraction patterns of $Co_{1.6}Ge_{0.6}Fe_{0.8}O_4$ are shown in Fig. 29. The lattice parameter of each sample was determined by Rietveld refinement based on X-ray diffraction data and the results are shown in Fig. 30. Comparing the results with the Ga-substituted cobalt ferrite, which showed a local maximum in lattice parameter at x~0.4 (Fig.13), Ge-substituted cobalt ferrite samples showed monotonic decrease in lattice parameter as Ge content increase up to x=0.6. This indicates, based on the same simple interpretation used for the Ga-series, that substitution of Ge^{4+} ions into tetrahedral sites caused the reduction in lattice parameter because the radius of Ge^{4+} ions in tetrahedral sites (r_{IV} = 0.039 nm) [37] is small compared with that of Fe^{3+} (r_{IV}= 0.049 nm) [37] in tetrahedral sites.

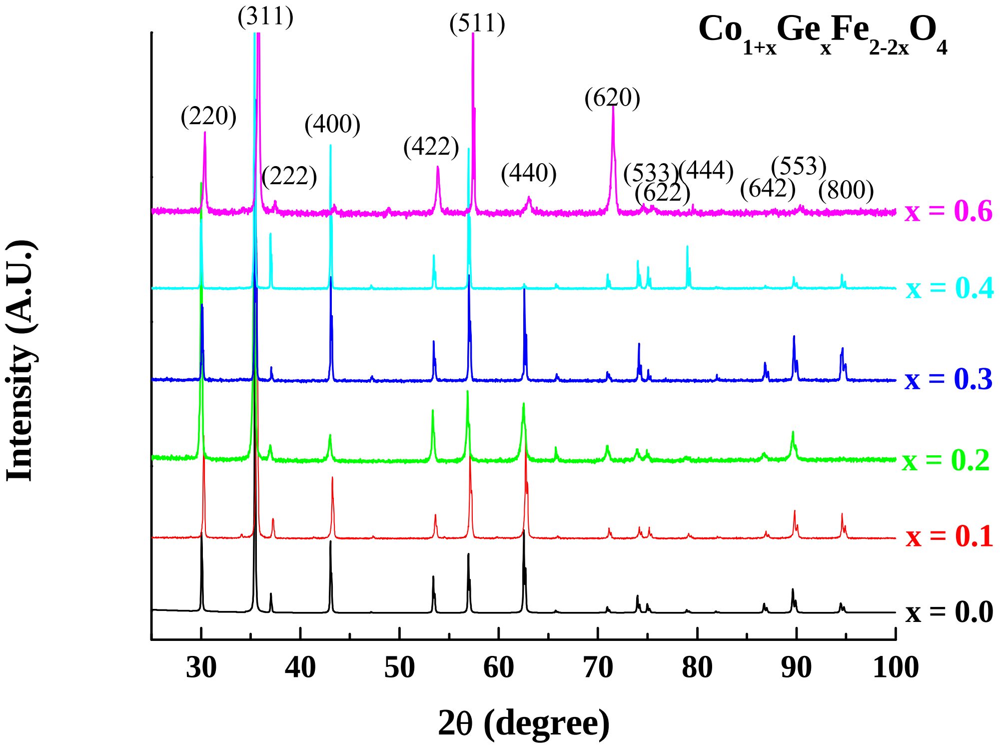

Fig. 28. X-ray diffraction patterns of Ga-substituted cobalt ferrites Co$_{1+x}$Ge$_x$Fe$_{2-2x}$O$_4$ (where x = 0.0 to 0.6)

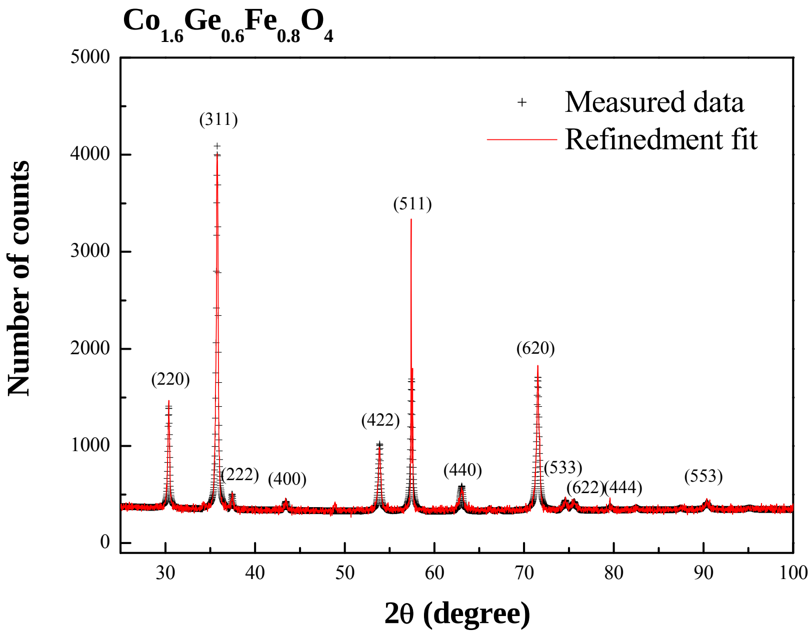

Fig. 29. Observed and calculated x-ray diffraction patterns of $Co_{1.6}Ge_{0.6}Fe_{0.8}O_4$.

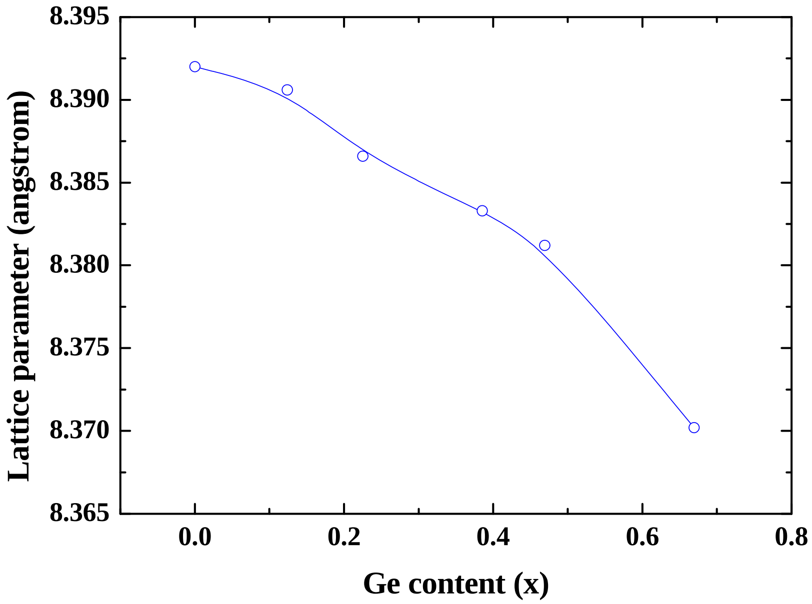

Fig. 30. Lattice parameters of $Co_{1+x}Ge_xFe_{2-2x}O_4$ (where x = 0.0 to 0.6).

4.2.2. SEM and EDX analysis

The comparison of target and final compositions of sintered samples is shown in Table. II. Scanning electron microscopy (SEM) investigations showed that all the sintered samples had a homogeneous microstructure with similar grain sizes of the order of 10 μm (Fig. 31.)

Table IV. Target compositions of a series of Ge-substituted cobalt ferrite samples, and the actual final compositions determined by energy-dispersive x-ray spectroscopy (EDX) in an SEM.

Target composition	Final composition by EDX		
	Fe	Co	Ge
$CoFe_{2.0}O_4$	2.05	0.95	—
$Co_{1.1}Ge_{0.1}Fe_{1.8}O_4$	1.77	1.11	0.12
$Co_{1.2}Ge_{0.2}Fe_{1.6}O_4$	1.57	1.21	0.22
$Co_{1.3}Ge_{0.3}Fe_{1.4}O_4$	1.29	1.33	0.38
$Co_{1.4}Ge_{0.4}Fe_{1.2}O_4$	1.10	1.43	0.47
$Co_{1.6}Ge_{0.6}Fe_{0.8}O_4$	0.70	1.63	0.67

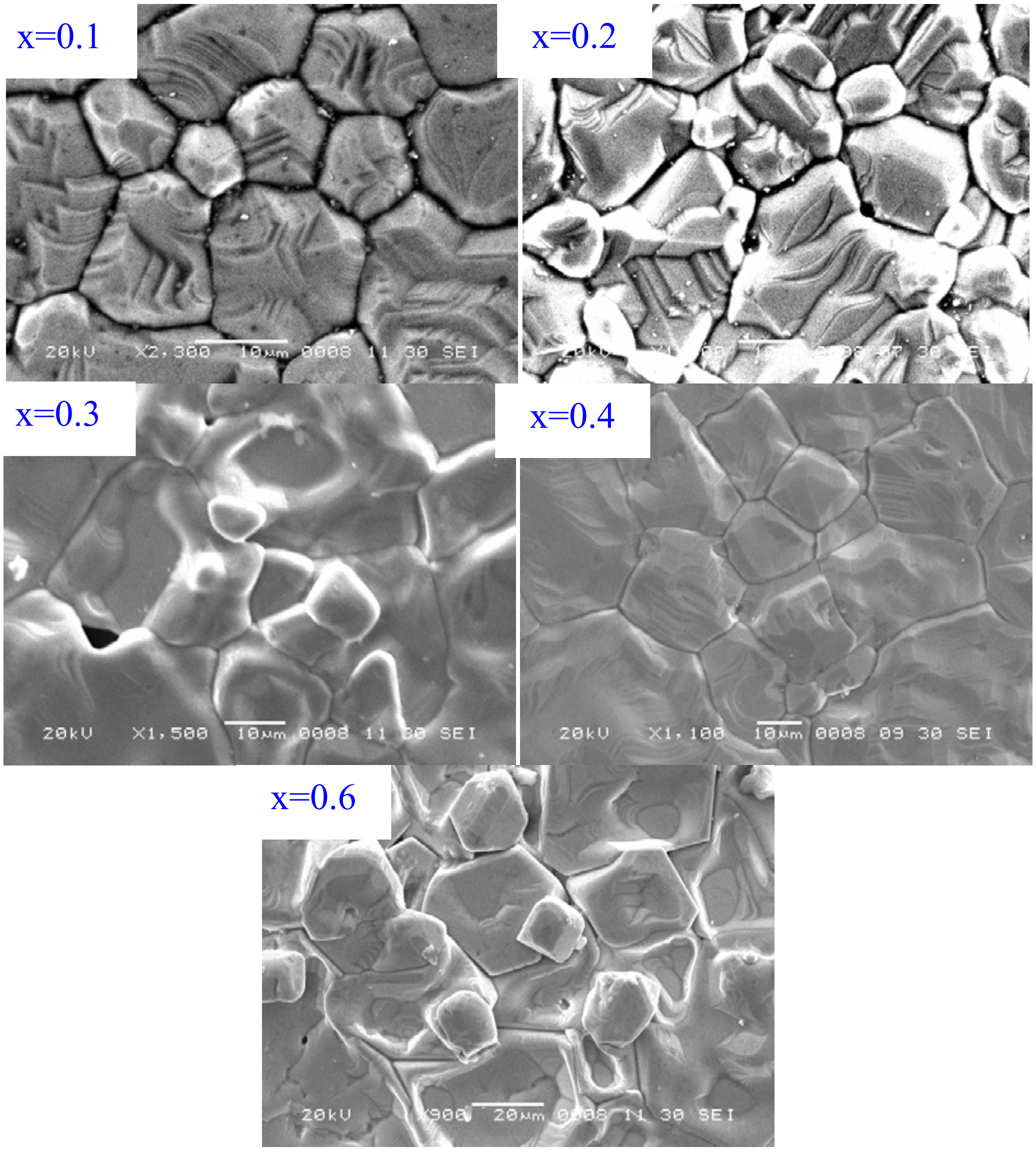

Fig. 31. SEM images of Ge-substituted cobalt ferrites $Co_{1+x}Ge_xFe_{2-2x}O_4$ (where x=0.0 to 0.6)

4.2.3. Curie temperature

The temperature dependent magnetizations of Ge substituted cobalt ferrite samples, $Co_{1+x}Ge_xFe_{2-2x}O_4$, are shown in Fig. 32. From the M vs T curves, it was evident that the Curie temperature T_C was reduced by substitution of Ge for Fe, which is a similar result to that observed in the Ga-series (Fig. 15). This is considered to be due to reduction in exchange interaction caused by Ge substitution.

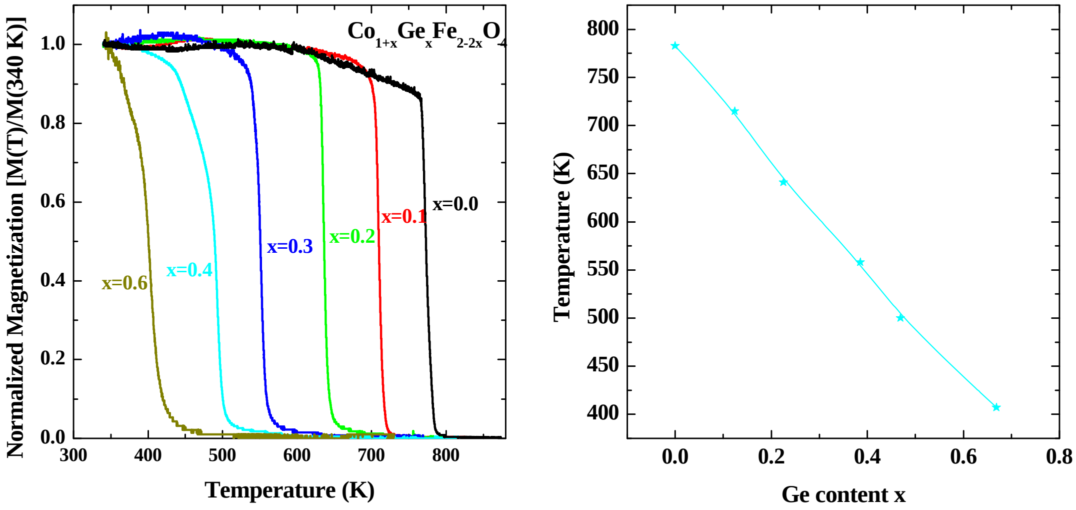

Fig. 32 (a) Temperature dependent normalized magnetization relative to value of 340 K for $Co_{1+x}Ge_xFe_{2-2x}O_4$ samples (where x=0.0 to 0.6) (b) Curie temperatures T_C of $Co_{1+x}Ge_xFe_{2-2x}O_4$ (where x = 0.0 to 0.6) as a function of the substituted content x.

4.2.4 Hysteresis curve

Fig. 33 shows the variation in M vs H and coercive force H_C with germanium content measured at room temperature. Compared with M vs T of pure cobalt ferrite, those of Ge-substituted cobalt ferrites show softer magnetic behavior (lower H_C) as the germanium content increases from x=0.1 to 0.6.

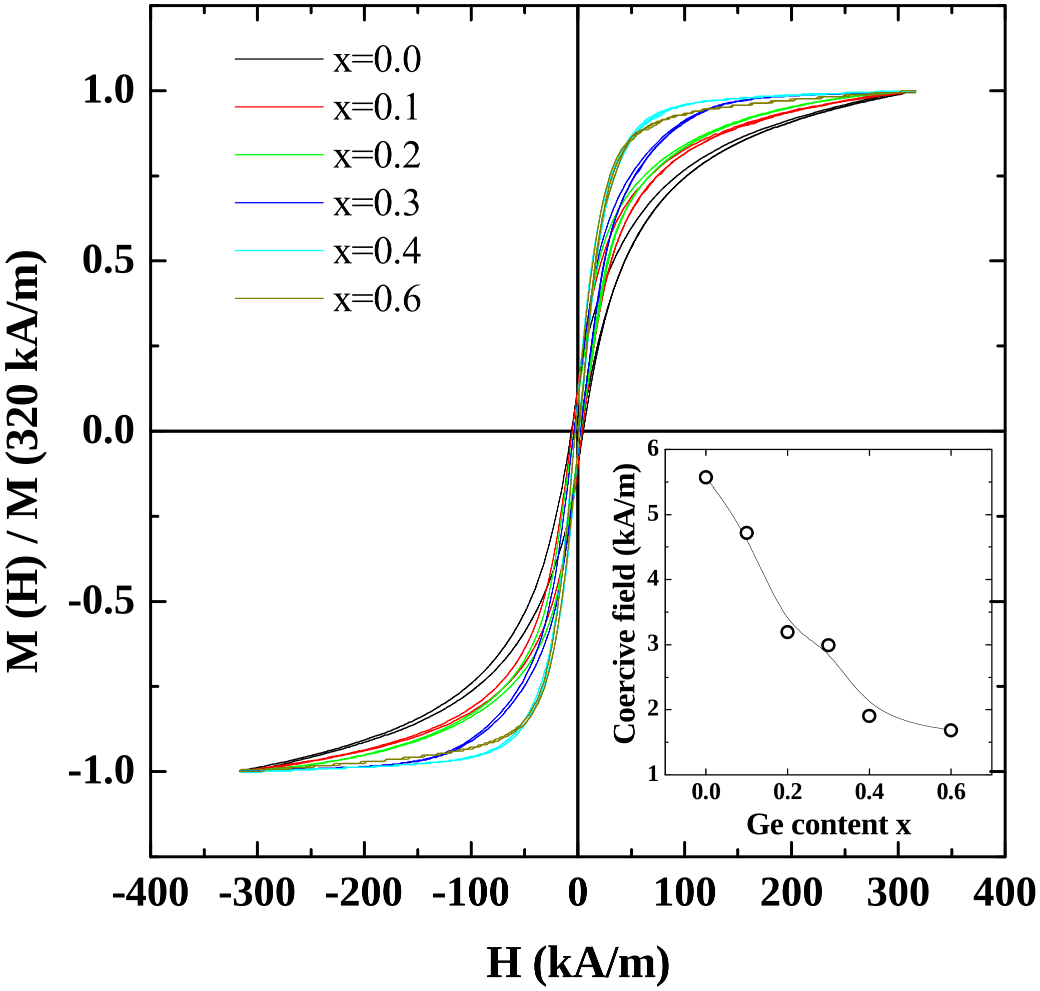

Fig. 33. Normalized magnetization (M) vs magnetic field (H) curves measured at room temperature for $Co_{1+x}Ge_xFe_{2-2x}O_4$ samples (where x=0.0 to 0.6). Inset: Coercive field (H_C) versus germanium content x.

4.2.5. Magnetostriction

Fig. 34 shows show the λ_H-λ_{Rem} vs magnetic field (H) curves for $Co_{1+x}Ge_xFe_{2-2x}O_4$ samples (where x=0.0 to 0.6) measured at room temperature. As shown in Fig. 34 the magnitude of magnetostriction decreased with increasing Ge content for x up to 0.6, which is similar with the results of Ga-series measured at 300 K (Fig. 23). While the magnitude of magnetostriction monotonically decreased with Ge content x, the magnitude of maximum strain derivative $[d(\lambda_H-\lambda_{Rem})/dH]_{max}$ significantly increased for all the samples with Ge content from 0.1 to 0.6 as shown in Fig. 35. Compared with Ga-series (Fig. 24 and 25), Ge-substituted cobalt ferrite shows much higher magnitude of $[d(\lambda_H-\lambda_{Rem})/dH]_{max}$ 5.7×10^{-6} $A^{-9}m$ which is the highest value among recently reported cobalt ferrite based materials. In the case of Ga-series, x=0.6 and 0.8 Ga samples showed a change in sign of magnetostriction from positive to negative values as field increased at 300 K, which should be an indicative of negative K_1. On the other hand, for Ge-series, there was no change in sign of magnetostriction even for the sample with the highest value of Ge content of x=0.6.

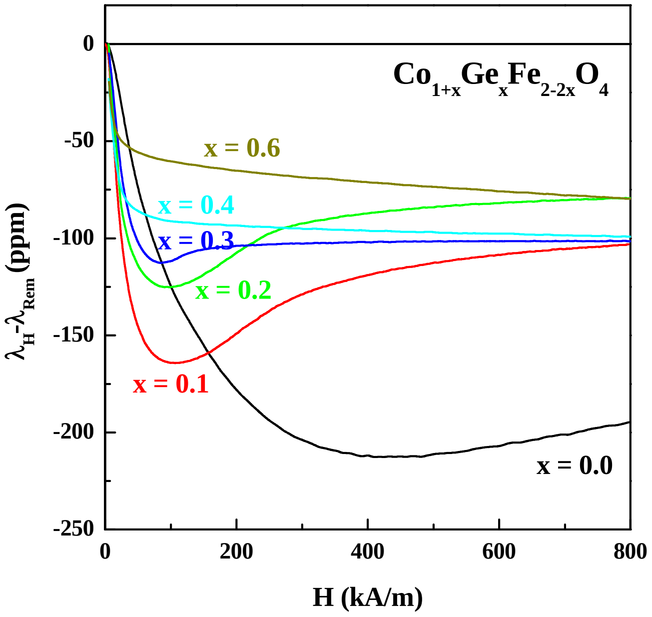

Fig. 34. Magnetostriction (λ_H-λ_{Rem}) vs magnetic field (H) curves for $Co_{1+x}Ge_xFe_{2-2x}O_4$ samples (where x=0.0 to 0.6) measured at room temperature.

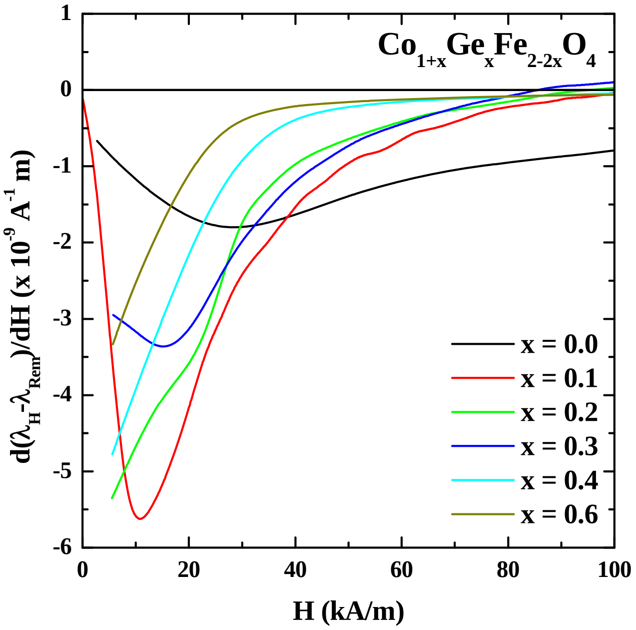

Fig. 35. Magnetostriction derivatives d(λ_H-λ_{Rem})/dH vs magnetic field (H) curves for $Co_{1+x}Ge_xFe_{2-2x}O_4$ samples (where x=0.0 to 0.6) measured at room temperature.

4.2.6. Domain images

Fig. 36 and 37 show the surface magnetic domain images of $Co_{1.33}Ga_{0.38}Fe_{1.29}O_4$ observed by Kerr effect microscopy and scanning probe magnetic force microscopy for large (300 μm x 300 μm) and small (40 μm x 40 μm) areas respectively. As shown in these figures various patterns and sizes of domains were observed at different locations on the surface, which usually occurs for polycrystalline magnetic materials with high magnetic anisotropy energy because the distribution of easy axes near the surface should be determined by the distribution in orientations of crystallites. Moreover, various external effects such as residual stresses, could be influencing the surface domain structure. For these reasons, investigating intrinsic domain structure should be done with single crystal samples with high quality.

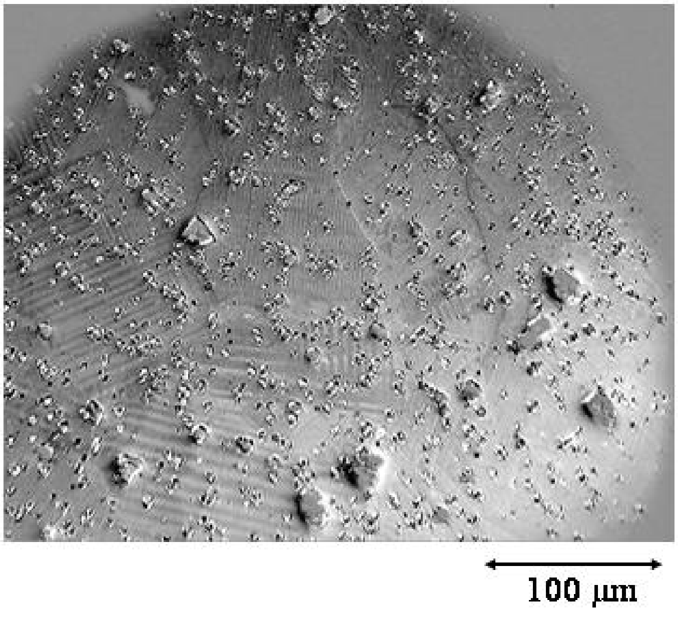

Fig. 36. Surface magnetic domain image of $Co_{1.33}Ga_{0.38}Fe_{1.29}O_4$ observed by Kerr effect microscope.

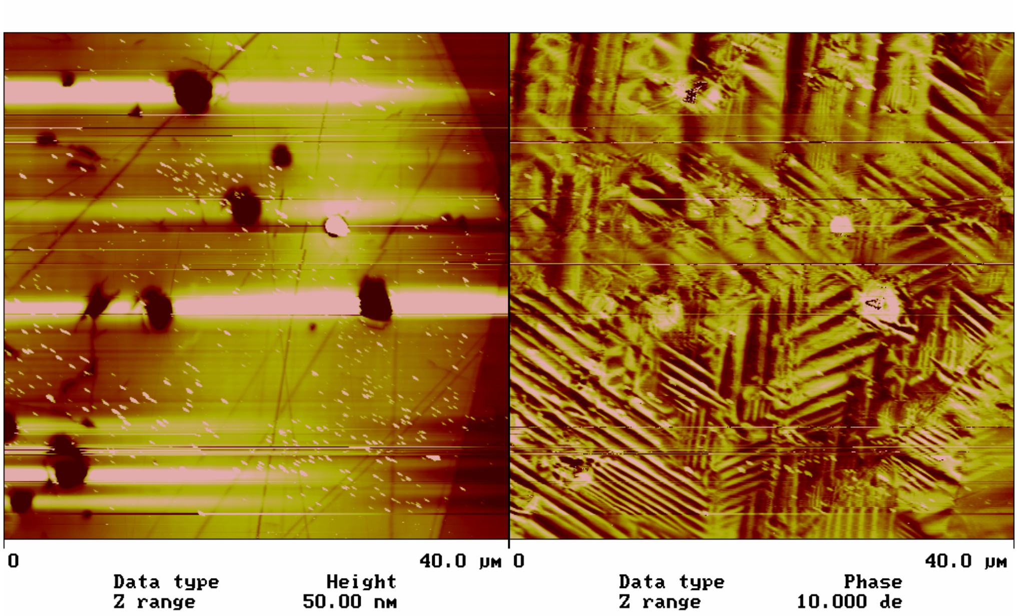

Fig. 37. Surface magnetic domain image of $Co_{1.33}Ga_{0.38}Fe_{1.29}O_4$ observed by scanning probe magnetic force microscope (MFM).

4.3 Comparison of experimental results of Mn-, Cr-, Ga-, and Ge-substituted cobalt ferrites

4.3.1 Lattice parameter

Composition dependent lattice parameters of Mn-, Cr-, Ga-, Ge-substituted cobalt ferrites were determined by Rietveld refinement based on X-ray diffraction data, which is shown in Fig. 38. In order to compare the relative sizes of cations included in these ferrite materials the effective radii of Cr, Mn, Fe, Co, Ga, and Ge ions at various conditions are listed in Table. V [37]. Supposing that all the magnetic elements have high spin state, the relative ionic sizes at the two possible interstitial sites in spinel structure are given by,

Tetrahedral site: $Co^{2+}<Ge^{4+}<Ga^{3+}<Fe^{3+}<Fe^{2+}<Mn^{2+}$

Octahedral site: $Ge^{4+}<Co^{3+}<Cr^{3+}<Ga^{3+}<Mn^{3+}$, $Fe^{3+}<Co^{2+}<Fe^{2+}<Cr^{2+}<Mn^{2+}<Ga^{2+}$.

For Ga- and Ge-substituted cobalt ferrites the reduction in lattice parameter with substitution content x can be understood by the smaller ionic sizes of Ga^{3+} and Ge^{4+} ions than Fe^{3+} ions in tetrahedral sites because these two ions are known to prefer tetrahedral site [11, 12]. However, in the case of Cr- and Mn- substituted cobalt ferrites, the behavior in lattice parameter with x can not be clearly understood. According to the relative ionic sizes in Table III, the size of Cr^{3+} ion is smaller than that of Mn^{3+} ion thus the lattice parameter of Cr-substituted cobalt ferrite was expected to be higher than that of Mn-substituted cobalt ferrite because both cations are known to prefer octahedral site [11]. Various possible hypotheses can be made to explain this phenomenon, such as existence of mixed valences in Cr or Mn ions, however, additional data need to be obtained for this analysis.

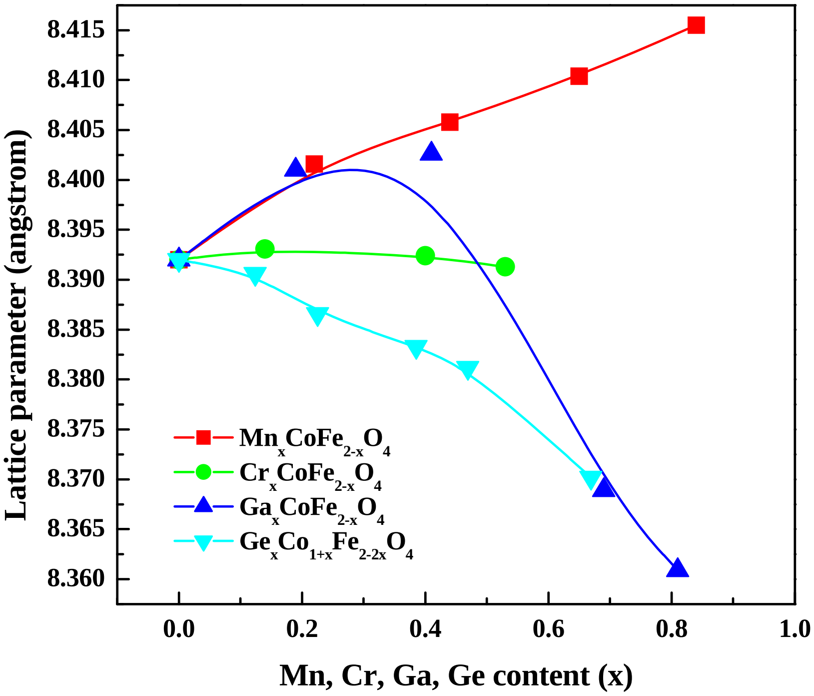

Fig. 38. Lattice parameters of $CoM_xFe_{2-x}O_4$ (M=Mn, Cr, Ga) and $Co_{1+x}Ge_xFe_{2-2x}O_4$ samples with various cation contents.

Table V. Effective ionic radii of some elements in 4th period. Effective ionic radii are based on the assumption that the ionic radii of O^{2-} (CN6) is 1.4 Å and that of F^- (CN6) is 1.33 Å [37].

	Condition	**Radius (Å)**
Cr^{2+}	Octahedral site, low spin	0.73
	Octahedral site, high spin	0.80
Cr^{3+}	Octahedral site	0.615
Mn^{2+}	Tetrahedral site, high spin	0.66
	Octahedral site, low spin	0.67
	Octahedral site, high spin	0.83
Mn^{3+}	Octahedral site, low spin	0.58
	Octahedral site, high spin	0.645
Fe^{2+}	Tetrahedral site, high spin	0.63
	Octahedral site, low spin	0.61
	Octahedral site, high spin	0.78
Fe^{3+}	Tetrahedral site, high spin	0.49
	Octahedral site, low spin	0.55
	Octahedral site, high spin	0.645
Co^{2+}	Tetrahedral site	0.38
	Octahedral site, low spin	0.65
	Octahedral site, high spin	0.745
Co^{3+}	Octahedral site, low spin	0.545
	Octahedral site, high spin	0.61
Ga^{2+}	Octahedral site	1.20
Ga^{3+}	Tetrahedral site	0.47
	Octahedral site	0.62
Ge^{4+}	Tetrahedral site	0.39
	Octahedral site	0.53

4.3.2 Curie temperature

The variation in Curie temperature T_C of Mn-, Cr-, Ga-, and Ge-substituted cobalt ferrite samples, $CoMn_xFe_{2-x}O_4$, $CoCr_xFe_{2-x}O_4$, $CoGa_xFe_{2-x}O_4$, $Co_{1+x}Ge_xFe_{2-2x}O_4$ with substituted content x are shown in Fig. 39. From the graph, it is evident that the Curie temperature T_C was reduced by substitution of any of the four elements of Mn, Cr, Ga, and Ge for Fe. This is considered to be due to reduction in exchange interaction caused by the substitution. In fact, T_C decreased at the greatest rate with Ge substitution compared with those of Ga, Cr, and Mn substitutions, which are listed in the order of decreasing rate. This can be understood based on the fact that Ge and Ga prefer tetrahedral sites while Cr and Mn prefer octahedral sites, and that tetrahedral sites have a higher number of nearest neighbor cations than octahedral sites (Fig. 7). If the exchange interaction energy is mainly determined by the number of nearest neighbor exchange interactions then the change in interaction energy caused by substitution at the tetrahedral site should be larger than at the octahedral sites.

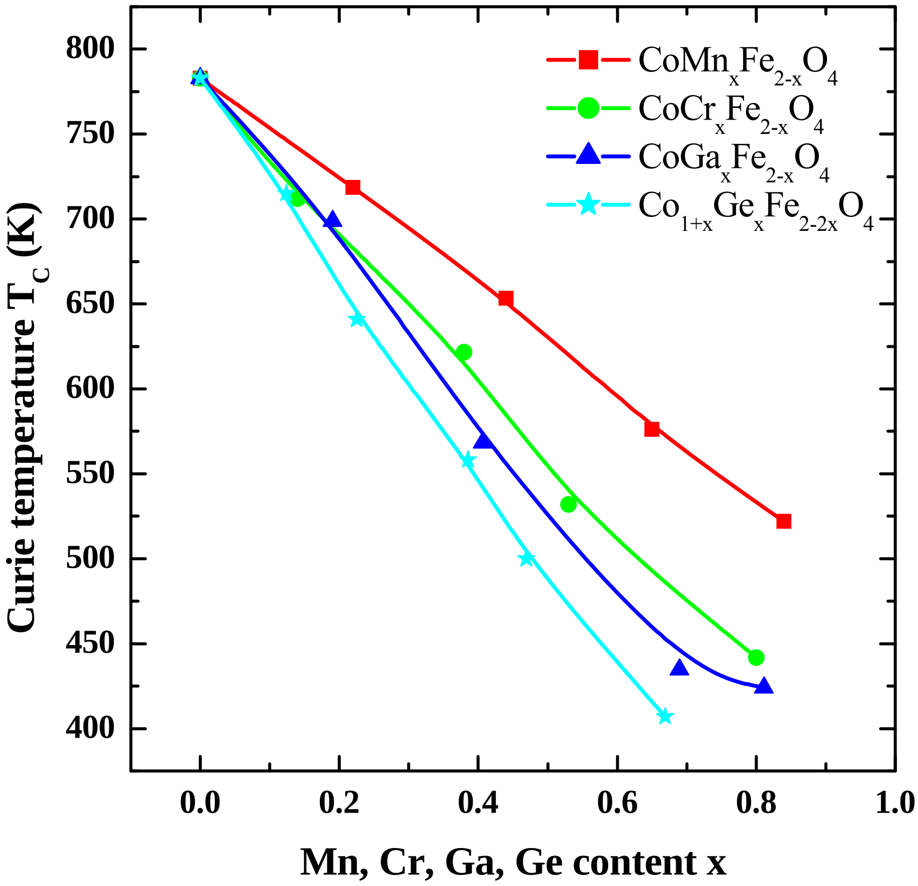

Fig. 39. Curie temperatures T_C of $CoMn_xFe_{2-x}O_4$, $CoCr_xFe_{2-x}O_4$, $CoGa_xFe_{2-x}O_4$ and $Co_{1+x}Ge_xFe_{2-2x}O_4$ samples (where x = 0.0 to 0.8) as a function of the substituted content x.

4.3.3 Hysteresis curves

Fig. 40 shows the variation in M vs H with substitution content x of $CoMn_xFe_{2-x}O_4$, $CoCr_xFe_{2-x}O_4$, $CoGa_xFe_{2-x}O_4$ and $Co_{1+x}Ge_xFe_{2-2x}O_4$ samples measured at room temperature. The general behavior was that as substitution content x increased the magnetization curves became magnetically softer for all samples. In order to compare the rate in magnetic softness among the samples coercive fields H_C for each series of samples were plotted as shown in Fig. 41. This result is considered to be due to the reduction in anisotropy energy, which should also influence the coercive field H_C. As shown in Fig. 41, the greatest rate in reduction of H_C with x was observed in the Ge-series. It should be mentioned that similar behavior was observed in T_C measurements (Fig. 39), which indicates that Ge-substitution was more efficient in reducing both the exchange interaction and anisotropy energies than the other three elements substitutions. For the Mn-series, which had been fabricated several years ago, each composition of sample was not fabricated under the same condition because the optimum condition for the fabrication process, such as sintering temperature or time, were not known at that time. Thus the coercive fields of Mn-series samples might be affected by the different fabrication processes used for different samples. In the case of the other three series, however, all the samples were fabricated under the same conditions and procedures. Therefore the differences in behavior of coercive field for these samples can be interpreted as due to intrinsic reasons.

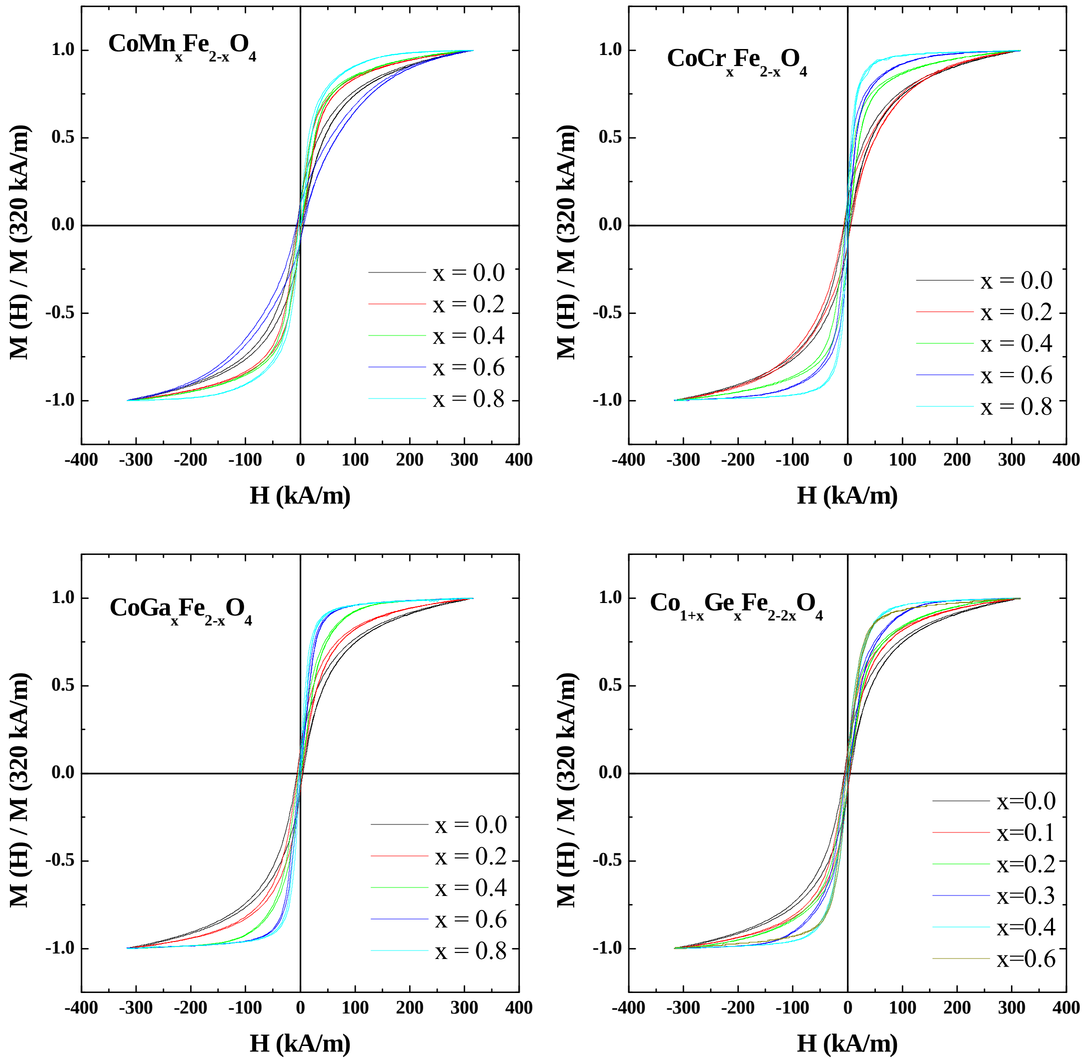

Fig. 40. Magnetization (M) vs magnetic field (H) curves for CoMn$_x$Fe$_{2-x}$O$_4$, CoCr$_x$Fe$_{2-x}$O$_4$, CoGa$_x$Fe$_{2-x}$O$_4$ and Co$_{1+x}$Ge$_x$Fe$_{2-2x}$O$_4$ samples (where x = 0.0 to 0.8) as a function of the substituted content x measured at room temperature.

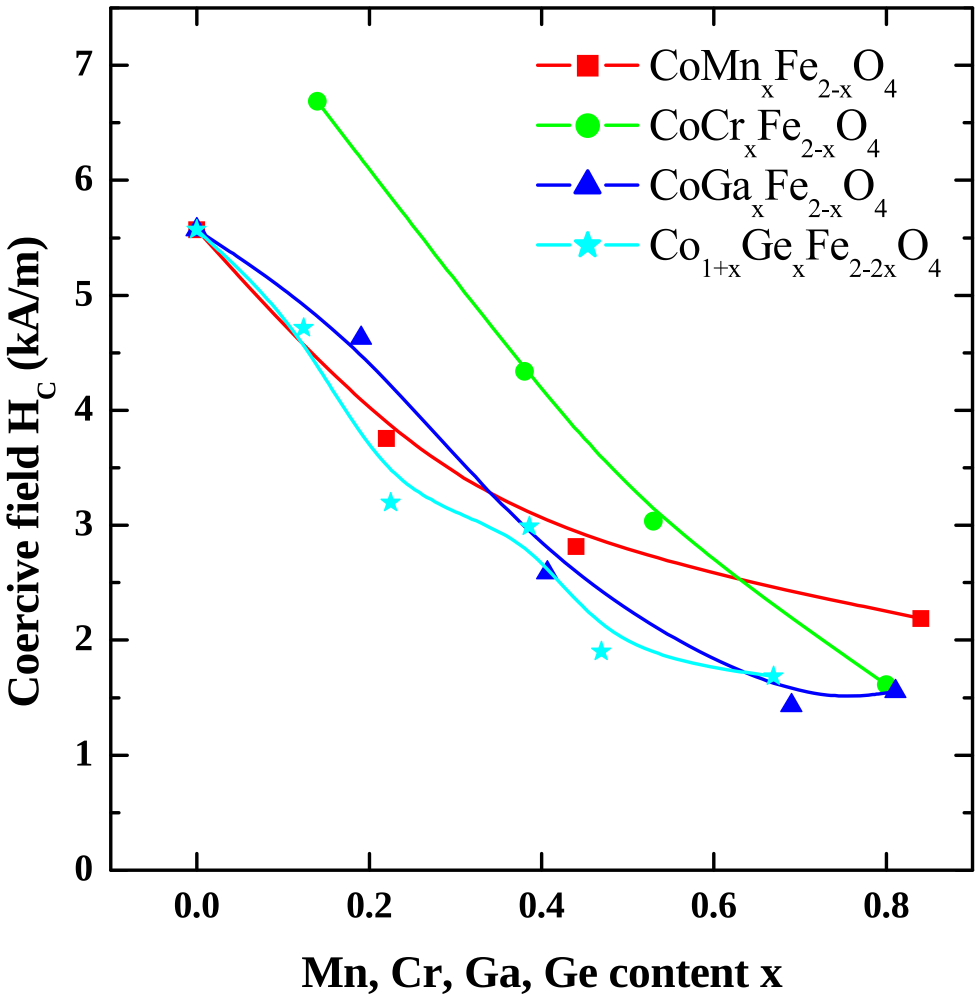

Fig. 41. Coercive fields H_C of $CoMn_xFe_{2-x}O_4$, $CoCr_xFe_{2-x}O_4$, $CoGa_xFe_{2-x}O_4$ and $Co_{1+x}Ge_xFe_{2-2x}O_4$ samples (where x = 0.0 to 0.8) as a function of the substituted content x measured at room temperature.

4.3.4 Magnetostriction

For reversible processes under small applied field and stress there is a thermodynamic relationship which relates $(d\lambda/dH)_\sigma$ to the stress sensitivity of induction $(dB/d\sigma)_H$ (see section 2.3). The strain derivative can therefore be used as a predictor of the stress sensitivity of magnetic induction to stress or torque when selecting materials for stress or torque sensor applications. In this respect, the strain derivatives $d(\lambda_H-\lambda_{Rem})/dH$ for $CoMn_xFe_{2-x}O_4$, $CoCr_xFe_{2-x}O_4$, $CoGa_xFe_{2-x}O_4$ and $Co_{1+x}Ge_xFe_{2-2x}O_4$ samples (where x = 0.0 to 0.8) measured at room temperature were compared as shown in Fig. 42. Generally the maximum magnitude in the strain derivative decreased as the substitution content x increased except for the Cr-series, which showed maximum slope of 2.2×10^{-9} $A^{-1}m$ at x=0.4 Cr sample. Among all the samples investigated, the maximum magnitude magnitude of $[d(\lambda_H-\lambda_{Rem})/dH]_{Max}$ 5.7×10^{-9} $A^{-1}m$ was observed in the x=0.1 Ge sample, which is the highest value among recently reported cobalt ferrite based materials. For Mn- and Ga-series, the maximum magnitudes of 2.7×10^{-9} $A^{-1}m$ and 2.8×10^{-9} $A^{-1}m$ were observed in x=0.2 Mn and Ga samples respectively. Actually the value of strain derivative was different for the two cases of magnetostriction curves; when H was increasing and decreasing. The calculated strain derivatives shown in Fig. 42 were obtained from the latter case.

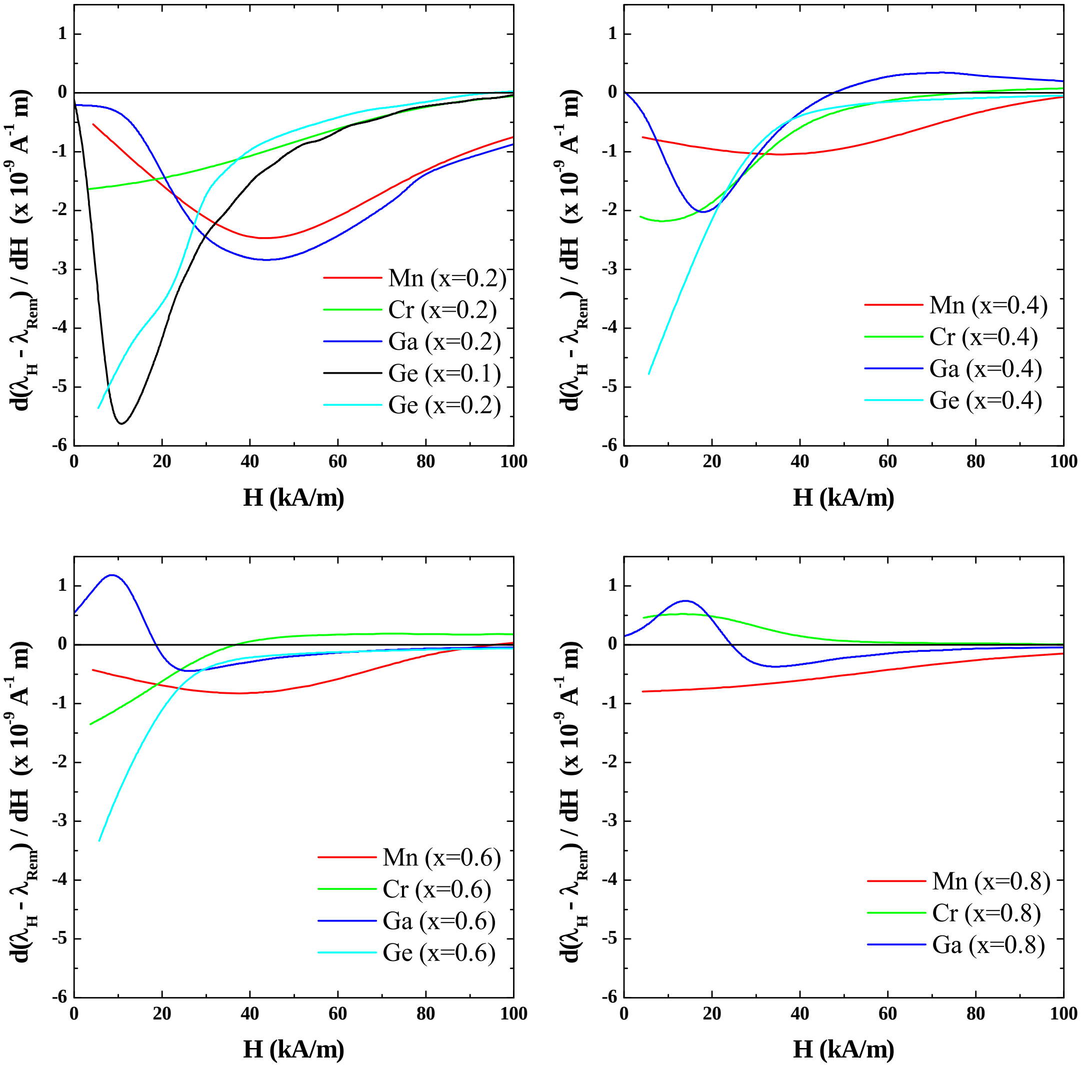

Fig. 42. Comparison in magnetostriction derivatives $d(\lambda_H\text{-}\lambda_{Rem})/dH$ vs magnetic field (H) curves for $CoMn_xFe_{2-x}O_4$, $CoCr_xFe_{2-x}O_4$, $CoGa_xFe_{2-x}O_4$ and $Co_{1+x}Ge_xFe_{2-2x}O_4$ samples (where x = 0.0 to 0.8) measured at room temperature.

5. CONCLUSIONS

The magnetic and magnetoelastic properties of a series of Ga- and Ge-substituted cobalt ferrites have been investigated and the results showed that by such substitutions it is possible to control the magnetic and magnetoelastic properties of the materials over a wide range. Substitution of Ga and Ge for Fe was found to decrease the Curie temperature at a greater rate than Mn or Cr substitution, which is consistent with the assumption that Ga^{3+} and Ge^{4+} ions prefer the tetrahedral sites (number of nearest neighbor cations = 12), whereas Mn^{3+} and Cr^{3+} prefer the octahedral sites (number of nearest neighbor cations = 6). The room temperature hysteresis curves were more easily changed to lower coercivity by Ga or Ge substitution than Mn or Cr substitution, which indicates that the anisotropy energy decreased more rapidly by Ga or Ge substitution than by Mn or Cr substitution.

The absolute magnitude of the first-order cubic anisotropy constant $|K_1|$ for Ga-substituted cobalt ferrites decreased as temperature increased, especially at the temperature range around 150-200 K there being an abrupt change in $|K_1|$. Similar behavior was observed at that temperature range in magnetostriction curves. There was also a rapid change in the maximum magnetostriction $[\lambda_H-\lambda_{Rem}]_{Max}$ and maximum magnetostriction derivatives $[d(\lambda_H-\lambda_{Rem})/dH]_{Max}$ around 150-200 K, which was not observed in pure cobalt ferrite. More evidence was observed in the slope of magnetostriction with magnetic field $d\lambda/dH$ for the high content of x=0.6 and 0.8 Ga samples; $d\lambda/dH$ changed from negative to positive as field increased for the temperature range below 200 K, while $d\lambda/dH$ changed from positive to negative as magnetic field increased for the temperature range above 200 K. Based on these results, it is considered that there was a change in sign of anisotropy constant K_1 at around 200 K for Ga-substituted cobalt ferrites.

At room temperature, the maximum magnitude of magnetostriction of Ga- and Ge-substituted cobalt ferrites decreased at about the same rate as was observed with Cr-substitution, however, the maximum strain derivative $(d\lambda/dH)_{max}$ of 5.7×10^{-9} $A^{-1}m$ for the x = 0.1 Ge sample, and 2.8×10^{-9} $A^{-1}m$ for the x = 0.2 Ga sample were greater than any of the Mn- or Cr-substituted samples. This enhanced $(d\lambda/dH)_{max}$ implies high stress sensitivity, which suggests that adjusting Ge or Ga content substituted into cobalt ferrite can be a promising route for controlling critical magnetic properties in sensor applications. For comparison between Ga- and Ge-substituted cobalt ferrites, both Ga^{3+} and Ge^{4+} ions are known to prefer tetrahedral sites, the higher ionic valence of Ge^{4+} ions seems to increase the magnetoelastic coupling between the magnetic ions and the lattice more than Ga^{3+} ions.

APPENDIX. AUTHOR'S PUBLICATIONS AND PRESENTATIONS

PUBLICATIONS

Song, S. H.; Lo, C. C. H.; Lee, S. J.; Aldini, S. T.; Snyder, J. E.; Jiles, D. C. (2007) "Magnetic and magnetoelastic properties of Ga-substituted cobalt ferrite" Journal of Applied Physics, 101, pp. 09C517.

Lee, S. J.; **Song, S.** H.; C. C. H.; Aldini, S. T.; Jiles, D. C. (2007) "Magneto-optic properties of $CoFe_{2-x}Ga_xO_4$" Journal of Applied Physics, 101, pp. 09C502.

Lee, S. J.; Lo, C. C. H.; Matlage, P. N.; **Song, S.** H.; Melikhov, Y.; Snyder, J. E.; Jiles, D. C. (2007) "Magnetic and magnetoelastic properties of Cr-substituted cobalt ferrite" accepted by Journal of Applied Physics.

Melikhov, Y.; Snyder, J. E.; Lo, C. C. H.; Matlage, P. N.; **Song, S. H.**; Dennis, K. W.; Jiles, D. C. (2006) "The effect of Cr-substitution on the magnetic anisotropy and its temperature dependence in Cr-substituted cobalt ferrite" IEEE Transactions on Magnetics, 42, pp. 2861.

Jiles, D. C.; **Song, S. H.** (2007) "Magnetic structures in $Pr_6Ni_2Si_3$ and $Pr_5Ni_2Si_3$" Journal of Applied Physics, 101, pp. 023918.

Song, S. H.; Snyder, J. E.; Jiles, D. C. (2006) "Theoretical calculation of magnetic structure variation in $Pr_5Ni_2Si_3$ compounds" Journal of Applied Physics, 99, pp. 08P304.

Song, S. H.; Pecharsky, A. O.; Wu, D.; Dennis, K. W.; Pecharsky, V. K.; Snyder, J. E.; Jiles, D. C.; Lograsso, T. A.; McCallum, R. W. (2005) "Thermal Expansion and Gruneisen Parameters in Some Pr-Ni-Si Compounds" Journal of Applied Physics, 97, pp. 10M516.

Jiles, D.C.; **Song, S. H.**; Snyder, J. E.; Pecharsky, V. K.; Lograsso, T. A.; Wu, D.; Pecharsky, A. O. ; Mudryk, Y. ; Dennis, K. W.; McCallum, R. W. (2005) "Thermal expansion and magnetostriction in Pr-Ni-Si compounds" Journal of Magnetism and Magnetic Materials, 299, pp. 288.

Song, S. H.; Snyder, J. E.; Jiles, D. C. (2005) "Thermal expansion and magnetostriction in $Pr_5Ni_2Si_3$ compounds" IEEE Transactions on Magnetics, 41, pp. 3499.

Lee, S. J.; **Song, S. H.**; Jiles, D. C.; Hauser, H. (2005) "Magneto-optic sensor for remote evaluation of surfaces" IEEE Transactions on Magnetics, 41, pp. 2257.

PRESENTATIONS

Song, S. H.; Lo, C. C. H.; Lee, S. J.; Aldini, S. T.; Snyder, J. E.; Jiles, D. C. “Magnetic and magnetoelastic properties of Ga-substituted cobalt ferrite” Presented at the 10th Joint Magnetism and Magnetic Materials/ InterMag Conference, Baltimore, Maryland, January 2007.

Lee, S. J.; **Song, S. H.**; C. C. H.; Aldini, S. T.; Jiles, D. C. “Magneto-optic properties of $CoFe_{2-x}Ga_xO_4$” Presented at the 10th Joint Magnetism and Magnetic Materials/ InterMag Conference, Baltimore, Maryland, January 2007.

Song, S. H.; Snyder, J. E.; Jiles, D. C. “Magnetic structures in $Pr_6Ni_2Si_3$ and $Pr_5Ni_2Si_3$ homologous compounds using first principles calculations” Presented at the International Conference on Magnetism, Kyoto, Japan, August 2006

Lo, C. C. H.; Matlage, P. N.; Melikhov, Y.; Snyder, J. E.; **Song, S. H.**; Jiles, D. C. “Magnetoelastic and magnetic properties of chromium substituted cobalt ferrite” Presented at the International Magnetics Conference, San Diego, May 2006.

Melikhov, Y.; Snyder, J. E.; Lo, C. C. H.; Matlage, P. N.; **Song, S. H.**; Dennis, K. W.; Jiles, D. C. “Magnetic anisotropy of Cr-substituted cobalt ferrite” Presented at the American Physical Society, March Meeting, Baltimore, March 2006.

Song, S. H.; Snyder, J. E.; Wu, D.; Lograsso, T. A.; Dennis, K. W.; McCallum, R. W.; Janssen, Y.; Jiles, D. C. “Thermal Expansion and Magnetostriction in $Pr_5Ni_2Si_3$ compounds” Presented at the International Magnetic Conference, Nagoya, April 2005.

Lee, S. J.; **Song, S. H.**; Melikhov, Y.; Jiles, D. C.; Hauser, H. “Jones matrix Analysis for Angular Displacement Sensor” Presented at the International Magnetic Conference, Nagoya, April 2005.

Song, S. H.; Snyder, J. E.; Wu, D.; Lograsso, T. A.; Dennis, K. W.; McCallum, R. W.; Janssen, Y.; Jiles, D. C. “Thermal Expansion and Magnetostriction in $Pr_5Ni_2Si_3$ Single crystal” Presented at the American Physical Society Conference, Los Angeles, California, March 2005.

Lee, S. J.; **Song, S. H.**; Jiles, D. C.; Hauser, H. “Application of magneto-optic sensor for the evaluation of non-magnetic and non-conducting surfaces” Presented at the 49th Annual Conference on Magnetism and Magnetic Materials, Jacksonville, Florida, November 2004.

Lee, S. J.; **Song, S. H.**; Jiles, D. C. “AC modulated magnetic optic sensor for remote investigation of surface deformation” Review of progress in quantitative NDE, Golden ,Colorado, July 2004.

Song, S. H.; Baker, B.J.; Paulsen, J.A.; Snyder, J.E.; Jiles, D.C.; Pecharsky, A.O.; McCallum, R.W.; Dennis, K.W. “Thermal Expansion and Magnetostriction in $Pr_5Ni_{1.9}Si_3$” Presented at the American Physical Society Conference, Montreal, Canada, May 2004.

JOURNAL OF APPLIED PHYSICS **101**, 09C517 (2007)

Magnetic and magnetoelastic properties of Ga-substituted cobalt ferrite

S. H. Song[a)]
Materials and Engineering Physics Program, Ames Laboratory, U.S. Department of Energy, Iowa State University, Ames, Iowa 50011 Department of Materials Science and Engineering, Iowa State University, Ames, Iowa 50011

C. C. H. Lo and S. J. Lee
Center for Nondestructive Evaluation, Iowa State University, Ames, Iowa 50011

S. T. Aldini
Materials and Engineering Physics Program, Ames Laboratory, U.S. Department of Energy, Iowa State University, Ames, Iowa 50011

J. E. Snyder and D. C. Jiles
Wolfson Centre for Magnetics, Cardiff University, Cardiff CF24 3AA, United Kingdom

(Presented on 10 January 2007; received 31 October 2006; accepted 3 January 2007; published online 3 May 2007)

Magnetic and magnetoelastic properties of a series of Ga-substituted cobalt ferrites, $CoGa_xFe_{2-x}O_4$ ($x=0.0-0.8$), have been investigated. The Curie temperature T_C and hysteresis properties were found to vary with gallium content (x), which indicates that exchange and anisotropy energies changed as a result of substitution of Ga for Fe. The maximum magnitude of magnetostriction decreased monotonically with increasing gallium content over the range $x=0.0-0.8$. The rate of change of magnetostriction with applied magnetic field ($d\lambda/dH$) showed a maximum value of 3.2×10^{-9} A^{-1} m for $x=0.2$. This is the highest value among recently reported cobalt ferrite based materials. It was found that the dependence of magnetic and magnetoelastic properties on the amount of substituent (x) was different for Mn, Cr, and Ga. This is considered to be due to the differences in cation site occupancy preferences of the elements within the spinel crystal structure: Mn^{3+} and Cr^{3+} prefer the octahedral (B) sites, whereas Ga^{3+} prefers the tetrahedral (A) sites. © *2007 American Institute of Physics*. [DOI: 10.1063/1.2712941]

I. INTRODUCTION

Cobalt ferrite based composites have high magnetostriction λ and high sensitivity $dB/d\sigma$ of magnetic induction to applied stress and are chemically. These factors make these materials attractive for use in magnetoelastic sensors.[1] However, to enable practical applications a family of materials is needed, in which the magnetoelastic response, magnetic properties, and their temperature dependences can be tailored by a well defined "control variable" such as chemical composition. Substituted cations can occupy tetrahedral or octahedral sites in the spinel structure. Mn^{3+} and Cr^{3+} are reported to prefer the octahedral sites.[2–4] A series of Mn- and Cr-substituted cobalt ferrite $CoMn_xFe_{2-x}O_4$ and $CoCr_xFe_{2-x}O_4$ (where $x=0.0-0.8$) samples was recently studied to investigate the effect of change in chemical composition and crystallographic site occupancy on the magnetic and magnetoelastic properties. Promising results were obtained, showing that Curie temperature and magnetic anisotropy could be decreased, and $d\lambda/dH$ increased without causing much loss of magnetostriction.[5–8] Mössbauer spectroscopy investigations confirmed that the Mn^{3+} ions and the Cr^{3+} ions substitute preferentially into the octahedral sites in cobalt ferrite.[9,10] In the present study, a family of Ga-substituted cobalt ferrite $CoGa_xFe_{2-x}O_4$ samples has been investigated. Ga^{3+} is known to prefer the tetrahedral sites,[11,12] therefore the results were expected to be different from those of Mn- and Cr-substituted cobalt ferrites.

II. EXPERIMENTAL METHODS

A series of polycrystalline Ga-substituted cobalt ferrite samples with compositions of $CoGa_xFe_{2-x}O_4$ (where $x=0.0-0.8$) was prepared by standard powder ceramic techniques[5] using Fe_2O_3, Ga_2O_3, and Co_3O_4 powders as precursors. Samples were calcined twice, sintered at 1350 °C for 24 h, and were subsequently furnace cooled to room temperature. The final compositions of the sintered samples were found to be close to the target composition, as shown in Table I. All the samples had a cubic spinel structure which

TABLE I. Target compositions of a series of Ga-substituted cobalt ferrite samples and the final compositions determined by energy-dispersive x-ray spectroscopy (EDX) in a SEM.

Target composition	Final composition by EDX		
	Fe	Co	Ga
$CoFe_{2.0}O_4$	2.05	0.95	···
$CoGa_{0.2}Fe_{1.8}O_4$	1.81	1.00	0.19
$CoGa_{0.4}Fe_{1.6}O_4$	1.55	1.04	0.41
$CoGa_{0.6}Fe_{1.4}O_4$	1.33	0.98	0.69
$CoGa_{0.8}Fe_{1.2}O_4$	1.15	1.04	0.81

[a)] Electronic mail: song73@iastate.edu

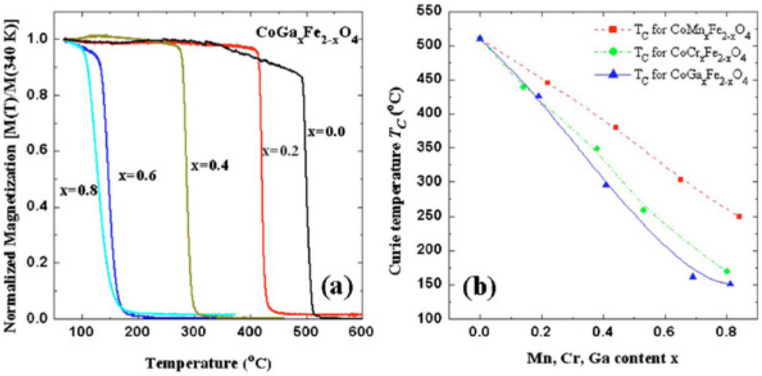

FIG. 1. (a) (Color online) Temperature dependent normalized magnetization for $CoGa_xFe_{2-x}O_4$ samples (where $x = 0.0-0.8$). (b) Curie temperatures T_C of $CoCr_xFe_{2-x}O_4$, $CoMn_xFe_{2-x}O_4$ and $CoGa_xFe_{2-x}O_4$ samples (where $x = 0.0-0.8$) as a function of the substituted content x.

was confirmed using x-ray powder diffractometry. Scanning electron microscopy (SEM) investigations showed that all the sintered samples had a homogeneous microstructure with similar grain sizes of the order of 10 μm. Magnetization (M) versus temperature (T) under a field of 7.96 kA/m (100 Oe) and magnetization (M) versus applied magnetic field (H) at ambient temperature (nominally 300 K) were measured using a vibrating sample magnetometer (VSM). The Curie temperature T_C was determined from the M vs T curve by linear extrapolation from the region of maximum slope down to the temperature axis. Magnetostriction as a function of applied field (λ vs H) was measured at room temperature using the strain gauge method.

III. RESULTS AND DISCUSSIONS

The temperature dependent magnetizations of Ga substituted cobalt ferrite samples, $CoGa_xFe_{2-x}O_4$, are shown in Fig. 1(a). From the M vs T curves, it was evident that the Curie temperature T_C was reduced by substitution of Ga for Fe. This is considered to be due principally to reduction in the A-B site exchange interaction caused by Ga substitution. A similar effect has been observed when substituting Mn or Cr for Fe in cobalt ferrite.[5,6] T_C decreases at a greater rate with Ga substitution than with Mn or Cr substitution [Fig. 1(b)]. This can perhaps be understood because the tetrahedral sites have a higher number of next nearest neighbor cations, to which they are superexchange coupled, than the octahedral sites have. Thus the change in interaction energy caused by substitution at the tetrahedral sites may be expected to be larger than at the octahedral sites for the same amount of substitution.

Figure 2 shows the variation in M vs H and coercive field (H_c) with gallium content. Compared with M vs H of pure cobalt ferrite, those of Ga-substituted cobalt ferrites show softer magnetic behavior (lower H_c) as the gallium content increases from $x=0.2$ to 0.8. This is believed to be due to the reduction in anisotropy energy caused by Ga substitution. Anisotropy energy decreases as a function of T/T_C faster than magnetization does. This has been both measured[13] and modeled theoretically[14] for single-crystal cobalt ferrite. Likewise, we have observed this experimentally for Mn-substituted and Cr-substituted cobalt ferrites.[7,8] So with T_C decreasing as a function of x even more strongly with Ga substitution than it does for Cr or Mn substitution, the anisotropy energy at 300 K is expected to decrease, even more than for Cr or Mn substitution for the same value of x.

Gallium substitution was found to have a strong effect

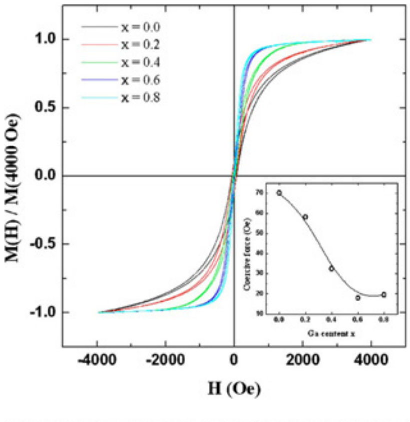

FIG. 2. (Color online) Normalized magnetization (M) vs magnetic field (H) curves measured at 300 K for $CoGa_xFe_{2-x}O_4$ samples (where $x=0.0-0.8$). Inset: coercive field (H_c) vs gallium content x.

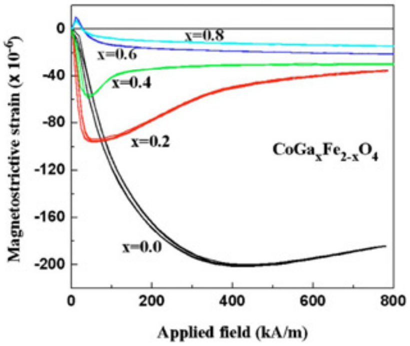

FIG. 3. (Color online) Magnetostriction (λ) vs magnetic field (H) curves for $CoGa_xFe_{2-x}O_4$ samples (where $x=0.0-0.8$).

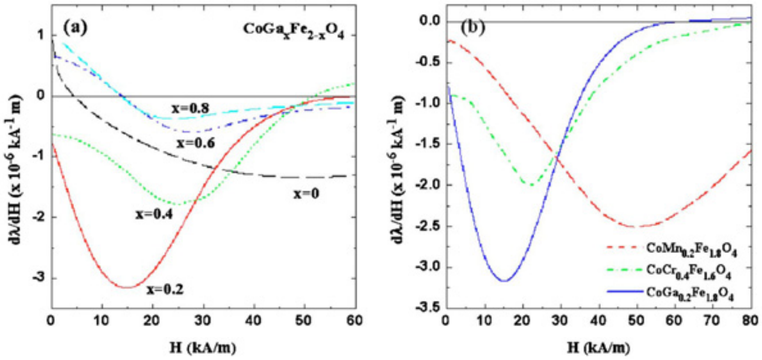

FIG. 4. (Color online) (a) Magnetostriction derivatives $d\lambda/dH$ for $CoGa_xFe_{2-x}O_4$ samples (where $x=0.0-0.8$). (b) Comparison of $d\lambda/dH$ for $CoMn_{0.2}Fe_{1.8}O_4$, $CoCr_{0.4}Fe_{1.6}O_4$, and $CoGa_{0.2}Fe_{1.8}O_4$ samples.

on magnetostriction. As shown in Fig. 3, the magnitude of magnetostriction decreased with increasing Ga content for x up to 0.8. The magnetostriction for low values of x ($x=0.0$, 0.2, and 0.4) was found to change slope as the field was increased, starting with a negative slope $d\lambda/dH$ at low fields but changing to a positive slope at high fields. This is indicative of different signs for the two cubic magnetostriction coefficients. For $x=0.6$ and $x=0.8$ the signs of the slope changed, so that it was positive at low fields, while at high fields the slope changed to negative. The simplest explanation for this is that the addition of Ga changed the sign of the anisotropy coefficient so that the magnetic easy axes changed from those with a negative magnetostriction to those with a positive magnetostriction. This would account for the low field slope change in from negative to positive. However, as the sign of the slope $d\lambda/dH$ still changed at high fields, this indicates that the magnetic hard axes had magnetostriction coefficients with different signs from the easy axes. It is worth mentioning that substituting small amounts of Ga for Fe (e.g., $CoGa_{0.2}Fe_{1.8}O_4$) increased the magnitude of maximum strain derivative $(d\lambda/dH)_{max}$, as shown in Fig. 4(a), while the magnitude of magnetostriction decreased monotonically with Ga content. Similar behavior has been observed in recent studies of Mn- and Cr-substituted cobalt ferrites $CoMn_xFe_{2-x}O_4$ and $CoCr_xFe_{2-x}O_4$,[5,6] in which the largest values of $(d\lambda/dH)_{max}$ for Mn- and Cr-substituted cobalt ferrites were reported to be 2.5×10^{-9} A^{-1} m (at $x=0.2$ for Mn) and 2.0×10^{-9} A^{-1} m (at $x=0.4$ for Cr), respectively. For Cr-substituted cobalt ferrite, the magnitude of $(d\lambda/dH)_{max}$ for $x=0.2$ Cr sample was 1.5 $\times10^{-9}$ A^{-1} m. Compared with Mn- and Cr-substituted cobalt ferrite, Ga-substituted cobalt ferrite shows much higher magnitude of $(d\lambda/dH)_{max}$ (3.2×10^{-9} A^{-1} m) even at a much lower applied field of $H=15$ kA/m [Fig. 4(b)]. The magnitude of $d\lambda/dH$ is expected to depend inversely on anisotropy energy (steeper $d\lambda/dH$ for lower anisotropy, when it is easier to change the direction of magnetization).

For reversible processes under small applied field and stress, there is a thermodynamic relationship which relates $(d\lambda/dH)_\sigma$ to the stress sensitivity of induction $(dB/d\sigma)_H$. The strain derivative can therefore be used as a predictor of the stress sensitivity of magnetic induction to stress or torque when selecting materials for stress or torque sensor applications.

IV. CONCLUSIONS

Substitution of Ga for Fe was found to decrease the Curie temperature at a greater rate than Mn or Cr substitution, which is consistent with the suggestion that Ga^{3+} ions prefer the tetrahedral sites whereas Mn^{3+} and Cr^{3+} prefer the octahedral sites. The maximum magnitude of magnetostriction λ_{max} decreased at about the same rate as was observed with Cr substitution; however, the strain derivative $(d\lambda/dH)_{max}$ of 3.2×10^{-9} A^{-1} m for the $x=0.2$ Ga sample was greater than for any of the Mn- or Cr-substituted samples. This enhanced $(d\lambda/dH)_{max}$ implies high stress sensitivity, which suggests that adjusting Ga content substituted into cobalt ferrite can be a promising route for controlling critical magnetic properties of the material for practical stress sensor applications.

ACKNOWLEDGMENTS

This work was supported by the U.S. NSF under Grant No. DMR-0402716 and by the UK Engineering and Physical Sciences Research Council under Grant No. EP/057094.

[1] Y. Chen, J. E. Snyder, C. R. Schwichtenberg, K. W. Dennis, R. W. McCallum, and D. C. Jiles, IEEE Trans. Magn. **35**, 3652 (1999).
[2] A. H. Morrish, *The Physical Principles of Magnetism* (Wiley, New York, 1965).
[3] A. Navrotsky and O. J. Kleppa, J. Inorg. Nucl. Chem. **29**, 2701 (1967).
[4] R. C. O'Handley, *Modern Magnetic Materials Principles and Applications* (Wiley, New York, 2000).
[5] J. A. Paulsen, A. P. Ring, C. C. Lo, J. E. Snyder, and D. C. Jiles, J. Appl. Phys. **97**, 044502 (2005).
[6] C. C. H. Lo, P. N. Matlage, Y. Melikhov, J. E. Snyder, S. H. Song, and D. C. Jiles, International Magnetics Conference, San Diego, 2006 (unpublished).
[7] Y. Melikhov, J. E. Snyder, D. C. Jiles, A. P. Ring, C. C. H. Lo, J. A. Paulsen, and K. W. Dennis, J. Appl. Phys. **99**, 08R102 (2006).
[8] Y. Melikhov, J. E. Snyder, C. C. H. Lo, P. Matlage, S. H. Song, K. Dennis, and D. C. Jiles, IEEE Trans. Magn. **42**, 2861 (2006).
[9] K. Krieble, C. C. H. Lo, Y. Melikhov, and J. E. Snyder, J. Appl. Phys. **99**, 08M912 (2006).
[10] K. Krieble, T. Schaeffer, J. A. Paulsen, A. P. Ring, C. C. H. Lo, and J. E. Snyder, J. Appl. Phys. **97**, 10F101 (2005).
[11] M. H. Mahmoud, H. H. Hamdeh, J. C. Ho, A. M. Abdalla, and A. I. Abdel-Mageed, Solid State Commun. **120**, 451 (2001).
[12] B. Kaur, M. Bhat, F. Licci, R. Kumar, S. D. Kulkarni, P. A. Joy, K. K. Bamzai, and P. N. Kotru, J. Magn. Magn. Mater. **305**, 392 (2006).
[13] H. Shenker, Phys. Rev. **107**, 1246 (1957).
[14] M. Tachiki, Prog. Theor. Phys. **23**, 1055 (1960).

JOURNAL OF APPLIED PHYSICS **101**, 09C502 (2007)

Magneto-optic properties of $CoFe_{2-x}Ga_xO_4$

S. J. Lee[a)]
Center for Nondestructive Evaluation, Iowa State University, Ames, Iowa 50011

S. H. Song
Department of Materials Science and Engineering, Iowa State University, Ames, Iowa 50011

C. C. Lo
Center for Nondestructive Evaluation, Iowa State University, Ames, Iowa 50011

S. T. Aldini
Materials and Engineering Physics Program, Ames Laboratory, U.S. Department of Energy (DOE), Ames, Iowa 50011

D. C. Jiles
Wolfson Centre for Magnetics, Cardiff CF24 3AA, United Kingdom

(Presented on 9 January 2007; received 31 October 2006; accepted 15 November 2006; published online 22 March 2007)

Research on cobalt ferrite based composites has increased recently due to their potential applications such as noncontact magnetoelastic stress or torque sensors and erasable magneto-optic recording media. We report a study of the polar Kerr rotation spectra for $CoFe_{2-x}Ga_xO_4$ (with $x=0.4$ and $x=0.8$). Each of the spectra consists of two peaks of negative Kerr rotation in the measured photon energy range of 1.5–3.0 eV. For $x=0.4$, one peak occured at 1.8 eV and the other at 2.25 eV. For $x=0.8$, the first peak shifted to a higher energy of about 1.9 eV, while the second peak remained at 2.25 eV. The origin of the peaks in the polar Kerr spectra and the observed shift of peak position resulting from Ga substitution can be explained by the intervalence charge-transfer transition, in which an electron from a metallic cation is transferred to a neighboring cation through an optical excitation. © *2007 American Institute of Physics*. [DOI: 10.1063/1.2693953]

I. INTRODUCTION

Cobalt ferrite $CoFe_2O_4$, which has a spinel crystal structure, shows interesting physical properties such as high sensitivity of magnetization to applied stress, excellent chemical stability, and a large magneto-optic effect.[1–4] There are two types of sublattice sites in the spinel structure, the tetrahedral (*A* sites) and the octahedral (*B* sites), and the different types of metallic ions are distributed according to the formula $Fe_A[CoFe]_BO_4$.[5] The Co^{2+} and Fe^{3+} cation distributions can be described as $(Fe^{3+})_A[Co^{2+}Fe^{3+}]_BO_4$. The magnetic properties or magneto-optic properties, including the exchange interactions, of these ferrites have been found to be dependent on how the cations are distributed among the two sublattices.[6–8]

Recently, cobalt ferrite composites[9] and their Mn-substituted modifications[10] have been actively investigated as part of the development of materials for highly sensitive noncontact stress and torque sensors. It was observed that the substitution of Mn for Fe led to the reduction of both the Curie temperature and the magnetostriction with increasing Mn content. This result indicates that it is possible to adjust the temperature dependence of magnetic properties and magnetomechanical hysteresis by systematic variation of the chemical composition.

Research into the magneto-optic properties of cobalt ferrites and their modifications based on chemical substitution has also been undertaken because of their potential application to magneto-optic recording media. Martens *et al.*[11] studied the magneto-optic properties of cobalt ferrite single crystals. They observed that the extrema (maxima and minima) of the polar Kerr rotation spectrum are located at photon energies of 1.8, 2.1, 3.5, 3.9, and ~5 eV. They concluded that the origin of these is most likely due to charge transfer transitions and crystal field transitions of Co^{2+} on the tetrahedral sites in the spinel structure. Kim *et al.*[2] studied magneto-optic transitions in $CoFe_2O_4$ and $NiFe_2O_4$ samples prepared as films on glass substrates by the sol-gel method. They observed peaks at 2.0 and 2.2 eV in the polar Kerr rotation spectrum. They attributed the peak at 2.0 eV as due to the crystal field transition from the $3d^7$ configuration of the Co^{2+} ions at the tetrahedral sites; and the peak at 2.2 eV as due to the $[Co^{2+}]t_{2g} \rightarrow [Fe^{3+}]t_{2g}$ intervalence charge transfer (IVCT) transitions. In an IVCT transitions, an electron in a cation is transferred to a neighboring cation through an optical excitation.[12]

Peeters and Martens[13] studied the polar Kerr rotations of $CoFe_{2-x}Al_xO_4$ and $Co_xFe_{3-x}O_4$. They have shown that the magneto-optic effects below 2 eV are contributed by the crystal field transitions of Co^{2+} (T_d) and by charge transfer transitions of Co^{2+} to Fe^{3+} on the octahedral sites. Recently Zhou *et al.*[4] investigated the doping effects of Al^{3+} on the magneto-optic Kerr effects in nanocrystalline $CoFe_{2-x}Al_xO_4$ thin films deposited on a silicon substrate. They found that the substitution of Fe^{3+} in $CoFe_2O_4$ by Al^{3+} caused the creation of additional peaks in the spectrum that were associated

---

[a)] Electronic mail: sjlee@ameslab.gov

0021-8979/2007/101(9)/09C502/3/$23.00

with crystal field transition, and also a shift of the Kerr rotation peak that was associated with an IVCT transition.

Magneto-optic Kerr spectra for iron containing spinels and garnets have similar transition structures for photon energies greater than 3 eV,[14–16] and therefore studies have focused on the polar Kerr rotation spectra below 3 eV.[3,13] In the present work, we studied the polar Kerr rotations for gallium substituted cobalt ferrite samples, $CoFe_{2-x}Ga_xO_4$ with $x=0.4$ and $x=0.8$. The samples were prepared by standard powder ceramic techniques, and the photon energy range of the magneto-optic polar Kerr spectra was measured between 1.5 and 3.0 eV with increments of 0.05 eV.

II. EXPERIMENTAL DETAILS

Polycrystalline bulk cobalt ferrite samples with compositions of $CoFe_{2-x}Ga_xO_4$ ($x=0.4$ and $x=0.8$) were prepared by standard powder ceramic techniques[9] using Fe_2O_3, Ga_2O_3, and Ga_3O_4 powder as precursors. Samples were calcined twice, sintered at 1350 °C for 24 h, and subsequently furnace cooled to room temperature. The final compositions of the sintered samples were found to be close to the target composition.

The crystal structures of the samples were determined using x-ray powder diffractometry. Scanning electron microscopy (SEM) was used to examine the microstructures. The surfaces of the polycrystalline cobalt ferrite samples were prepared for the optical measurements by polishing with abrasives, the final grade being a paste of 0.3 μm diameter alumina. Magneto-optic measurements were performed with a polar configuration setup using a 75 W Xe short-arc lamp light source with a photoelastic modulator (PEM).[17]

In the polar Kerr effect, the near-normal incident, linearly polarized light becomes elliptically polarized light after it is reflected. The major axis of the reflected light is rotated from the polarization axis of the incident light. The angle of rotation is known as the Kerr angle or Kerr rotation. In this experiment, the angle of incidence was kept below 4°. A magnetic field of 5 kG was applied at room temperature perpendicular to the sample surface.

III. RESULTS AND DISCUSSION

X-ray diffraction measurements showed that the polycrystalline cobalt ferrite samples with compositions of $CoFe_{2-x}Ga_xO_4$ ($x=0.4$ and $x=0.8$) have a single phase spinel crystal, as shown in Fig. 1. No extra crystalline phases or peaks related to CoO and Fe_2O_3 were observed. All the sintered samples were found to have a homogeneous microstructure with similar grain sizes of the order of 10 μm. An example is given in Fig. 2, which shows the SEM image of the $CoFe_{1.2}Ga_{0.8}O_4$ sample.

The measured polar Kerr rotation spectra for $CoFe_{2-x}Ga_xO_4$ ($x=0.4$ and $x=0.8$) samples are shown in Fig. 3. Each consists of two peaks of negative Kerr rotation. For $x=0.4$, one peak occurred at 1.8 eV and the other was at 2.25 eV. For $x=0.8$, the first peak shifted to a higher energy of about 1.9 eV, while the second peak remained at 2.25 eV. Similar peaks at 1.8 and 2.1 eV appeared in the polar Kerr

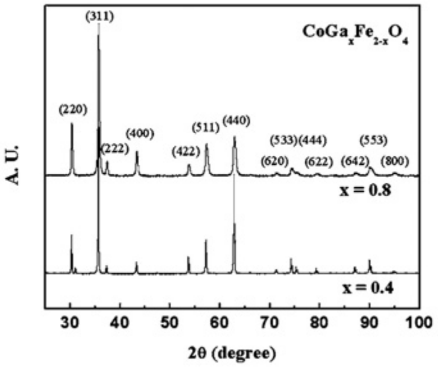

FIG. 1. X-ray diffraction data for polycrystalline cobalt ferrite samples with compositions of $CoFe_{2-x}Ga_xO_4$ ($x=0.4$ and $x=0.8$).

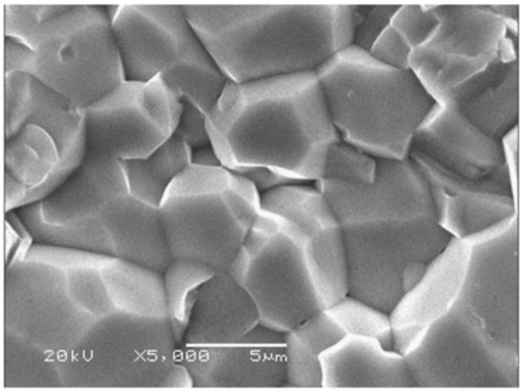

FIG. 2. SEM image showing a homogeneous, equiaxed microstructure of the $CoFe_{2-x}Ga_xO_4$ with $x=0.8$.

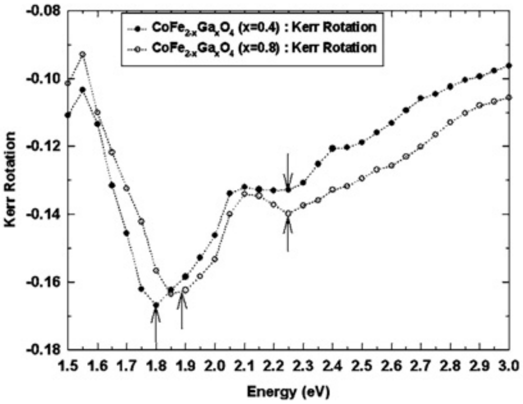

FIG. 3. Magneto-optic Kerr rotation spectra for $CoFe_{2-x}Ga_xO_4$ ($x=0.4$ and $x=0.8$) samples.

rotation spectrum of cobalt ferrite single crystal.[11] The origin of these peaks was not clear, but both Co^{2+} charge transfer transitions and crystal field transitions of Co^{2+} were assumed to contribute to these peaks.

Zhou *et al.*[3] introduced the molecular orbital theory of IVCT transitions to interpret the correlation between structures and IVCT transitions. The theory indicated that doping with the relatively large ions could lead to the increase of the distance between Co^{2+} and Fe^{3+} ions at the octahedral sites, and this caused the energy gap of the IVCT transitions to be reduced. Alternatively when the doping ions are relatively small, the energy gap of IVCT transitions increases. As the radius of the Ga^{3+} ions [$r_{VI}=0.062$ nm (Ref. 18)] is small compared with that of Fe^{3+} ions [$r_{VI}=0.0645$ nm with high spin state (Ref. 18)], the energy gap of IVCT transitions would increase with increased Ga^{3+} ion content. The peak position at 1.8 eV shifted to 1.9 eV as the doping concentration of $CoFe_{2-x}Ga_xO_4$ increased from $x=0.4$ to 0.8, as expected from the molecular orbital theory of IVCT transitions. However, for the peak position of 2.25 eV no noticeable shift was observed as doping level increased.

IV. SUMMARY AND CONCLUSIONS

The magneto-optic spectra and, in particular, the polar Kerr rotations of Ga substituted cobalt ferrites have been investigated for $CoFe_{2-x}Ga_xO_4$ with $x=0.4$ and $x=0.8$. A peak appeared at 1.8 eV in the Kerr rotation spectrum of $CoFe_{2-x}Ga_xO_4$ with $x=0.4$ and this shifted to 1.9 eV for the $CoFe_{2-x}Ga_xO_4$ composition with $x=0.8$. This shift can be explained by the molecular orbital theory of IVCT transitions, which predicts that the smaller radius of Ga^{3+} ions substituting for Fe^{3+} ions in $CoFe_{2-x}Ga_xO_4$ increases the energy gap of IVCT transitions. This observation was correct for the lower energy peak but was not clear for the higher energy peak at 2.25 eV. It was observed from the experiment that the control of Kerr rotation of Ga substituted cobalt ferrites is possible by adjusting the Ga content.

ACKNOWLEDGMENTS

This research was supported by NSF Division of Materials Research under Grant No. DMR-0402716 and by the UK Engineering and Physical Sciences Research Council under Grant No. EP/D057094.

[1] Y. Melikhov, J. E. Snyder, C. C. H. Lo, P. N. Matlage, S. H. Song, K. W. Dennis, and D. C. Jiles, IEEE Trans. Magn. **42**, 2861 (2006).

[2] K. J. Kim, H. S. Lee, M. H. Lee, and S. H. Lee, J. Appl. Phys. **91**, 9974 (2002).

[3] B. Zhou, Y. W. Zhang, Y. J. Yu, C. S. Liao, C. H. Yan, L. Y. Chen, and S. Y. Wang, Phys. Rev. B **68**, 024426 (2003).

[4] B. Zhou, Y.-W. Zhang, C.-S. Liao, Y.-J. Yu, C.-H. Yan, L.-Y. Chen, and S.-Y. Wang, Appl. Phys. Lett. **82**, 1188 (2003).

[5] W. G. Wyckoff, *Crystal Structures* (Wiley-Interscience, New York, 1965).

[6] L. Zhao, H. Yang, X. Zhao, L. Yu, Y. Cui, and S. Feng, Mater. Lett. **60**, 1 (2006).

[7] K. Suzuki, T. Namikawa, and Y. Yamazaki, Jpn. J. Appl. Phys., Part 1 **27**, 361 (1988).

[8] M. Abe and M. Gomi, J. Appl. Phys. **53**, 8172 (1982).

[9] R. W. McCallum, K. W. Dennis, D. C. Jiles, J. E. Snyder, and Y. Chen, Low Temp. Phys. **27**, 266 (2001).

[10] J. A. Paulsen, A. P. Ring, C. C. H. Lo, J. E. Snyder, and D. C. Jiles, J. Appl. Phys. **97**, 044502 (2005).

[11] J. W. D. Martens, W. L. Peeters, and E. Erman, Solid State Commun. **41**, 667 (1982).

[12] W. F. J. Fontijn, P. J. van der Zaag, M. A. C. Devillers, V. A. M. Brabers, and R. Metselaar, Phys. Rev. B **56**, 5432 (1997).

[13] W. L. Peeters and J. W. D. Martens, J. Appl. Phys. **53**, 8178 (1982).

[14] Z. Simsa, P. Siroky, F. Lukes, and E. Schmidt, Phys. Status Solidi B **96**, 137 (1979).

[15] S. Wittekoek, T. A. J. Popma, J. M. Robertson, and P. F. Bongers, Phys. Rev. B **12**, 2777 (1975).

[16] F. J. Khan, P. S. Pershan, and J. P. Remeika, Phys. Rev. **186**, 891 (1969).

[17] S. J. Lee, R. Lange, S. Hong, S. Zollner, P. C. Canfield, B. N. Harmon, and D. W. Lynch, Thin Solid Films **313–314**, 222 (1998).

[18] J. A. Dean, *Lange's Handbook of Chemistry*, 15th ed. (McGraw-Hill, New York, 1999).

IEEE TRANSACTIONS ON MAGNETICS, VOL. 42, NO. 10, OCTOBER 2006 2861

The Effect of Cr-Substitution on the Magnetic Anisotropy and Its Temperature Dependence in Cr-Substituted Cobalt Ferrite

Y. Melikhov[1,2], J. E. Snyder[2,3,4], C. C. H. Lo[1], P. N. Matlage[3], S. H. Song[3], K. W. Dennis[4], and D. C. Jiles[2], *Fellow, IEEE*

[1]Center for Nondestructive Evaluation, Iowa State University, Ames, IA 50011 USA
[2]Wolfson Centre for Magnetics, Cardiff University, Cardiff CF24 3AA, U.K.
[3]Materials Science and Engineering Department, Iowa State University, Ames, IA 50011 USA
[4]Materials and Engineering Physics Program, Ames Laboratory, U.S. Department of Energy (DOE), Ames, IA 50011 USA

The temperature dependence of the magnetic anisotropy of magnetoelastic chromium-substituted cobalt ferrites ($CoCr_xFe_{2-x}O_4$ with $0 \leqslant x \leqslant 0.8$) was investigated over the temperature range 10–400 K. The first-order cubic anisotropy coefficient K_1 was calculated by fitting the high-field regimes of the major hysteresis loops to the law of approach to saturation, which is based on the assumption that at sufficiently high field only rotational processes remain. It was found that anisotropy increases substantially with decreasing temperature from 400 to 150 K. Below 150 K, it appears that even under a maximum applied field of 5 T, the anisotropy of $CoFe_2O_4$ and $CoCr_{0.2}Fe_{1.8}O_4$ is so high that it prevents complete approach to saturation. In general, at fixed temperature the magnetic anisotropy decreases with increasing Cr content, which could be explained based on the one-ion model and the results of Mossbauer studies: According to the one-ion anisotropy model, Co^{2+} ions in octahedral sites of the spinel structure are responsible for the high anisotropy of cobalt ferrite, and substitution of Cr^{3+} for Fe^{3+} appears to displace Co^{2+} ions from octahedral sites to tetrahedral sites.

Index Terms—**Cobalt ferrite, ferrite, law of approach (LoA), magnetic anisotropy.**

I. INTRODUCTION

NEW magnetostrictive cobalt–ferrite composites and their substituted modifications [1], [2] show magnetoelastic properties that are promising for use in stress or torque sensors because of their high levels of magnetostriction λ and high slope of magnetostriction versus applied field $d\lambda/dH$. In order to selectively control the magnetomechanical response of these materials for strain sensing and actuating applications, more needs to be known about the variation of the basic magnetic and magnetoelastic properties with composition and temperature.

Magnetic anisotropy is one of the important properties determining magnetoelastic response. In this paper, we report the effect of chromium substitution for iron on magnetocrystalline anisotropy and its temperature dependence for a series of sintered bulk Cr-substituted cobalt ferrites ($CoCr_xFe_{2-x}O_4$ with $0 \leqslant x \leqslant 0.8$) over the temperature range 10–400 K.

II. EXPERIMENTAL DETAILS AND RESULTS

A series of chromium-substituted cobalt–ferrite samples with compositions $CoCr_xFe_{2-x}O_4$ (where x ranges from 0 to 0.8) were prepared by standard powder ceramic techniques [1], [2] with two calcining steps, and a final sintering at 1350 °C for 24 h and subsequent furnace cooling to room temperature. The actual compositions were determined by energy dispersive X-Ray spectroscopy (EDX) in a scanning electron microscope (SEM) and were found to be close to the target compositions. SEM studies also revealed a dense, homogeneous microstructure of equiaxed grains of typically 10 μm in diameter in all samples. X-ray powder diffractometry (XRD) showed all samples to be single phase, with the cubic spinel crystal structure.

The Curie temperatures T_C of the samples were determined using a vibrating sample magnetometer (VSM) to measure magnetization versus temperature. T_C values were found to decrease linearly with Cr content, from 787 K for $CoFe_2O_4$ to 442 K for $CoCr_{0.8}Fe_{1.2}O_4$.

The temperature dependence of magnetization was measured using a superconducting quantum interference device (SQUID) magnetometer, at an applied field $\mu_0 H$ of 5 T (50 kG) for decreasing temperature from 400 to 10 K. It was found that the maximum magnetization for chromium-substituted cobalt ferrite increased with decreasing temperature as shown in Fig. 1, in a manner one might expect for a simple collinear ferrimagnetic system. The apparent decrease in magnetization for the $CoFe_2O_4$ and $CoCr_{0.2}Fe_{1.8}O_4$ samples for temperatures below about 150 K has been attributed to the applied field being no longer able to saturate the samples at these temperatures.

Major hysteresis loops at selected temperatures were measured using a SQUID magnetometer. Fig. 2 shows an example of the first and second quadrant portions of the major hysteresis loops for $CoCr_{0.4}Fe_{1.6}O_4$ at different temperatures. Coercive field H_C, which was found from the major hysteresis loops, decreased with increasing temperature for all samples over the whole range of temperatures as shown in Fig. 3. However, for a fixed temperature the $CoCr_{0.2}Fe_{1.8}O_4$ sample has the largest coercive field.

The first-order cubic anisotropy constant was determined by the following method: It was assumed that all hysteretic processes were completed when the major hysteresis loop closed (see Fig. 2), and that further increase of the magnetization

---

Digital Object Identifier 10.1109/TMAG.2006.879888

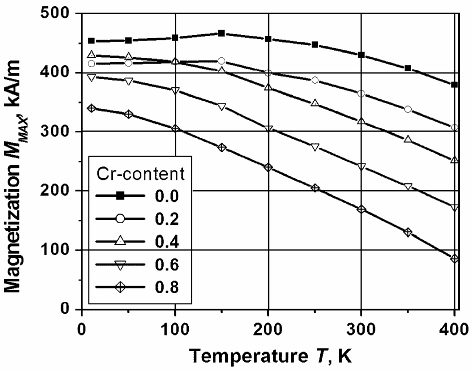

Fig. 1. Temperature dependence of measured maximum magnetization M_{MAX} at an applied field of 4×10^6 A.m^{-1}($\mu_0 H = 5$ T) for chromium-substituted cobalt–ferrite samples.

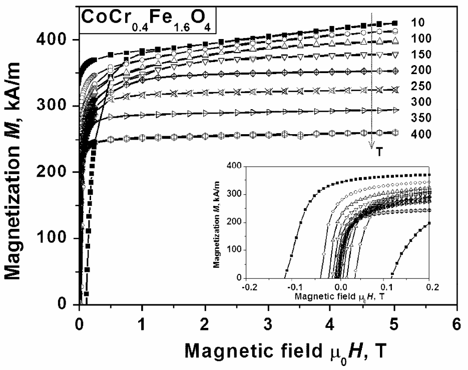

Fig. 2. Major hysteresis loops of $CoCr_{0.4}Fe_{1.6}O_4$ for different temperatures. The inset shows the second quadrant and low-field first quadrant portions of the major hysteresis loops

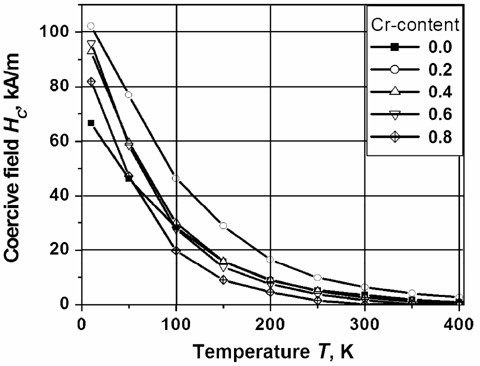

Fig. 3. Coercive field H_C as a function of temperature for chromium-substituted cobalt ferrites.

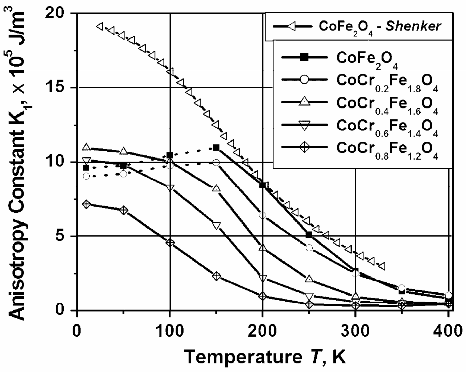

Fig. 4. Temperature dependence of the first-order cubic anisotropy coefficient K_1 determined by LoA to saturation for chromium-substituted cobalt–ferrite samples $CoCr_xFe_{2-x}O_4$ with various chromium contents ($x = 0$ to 0.8). The dotted lines for the $x = 0.0$ and 0.2 samples for temperatures lower than 150 K show that in these cases the anisotropy constant could not be determined correctly by this method when using maximum applied field $\mu_0 H = 5$ T.

was due to rotational processes, which are determined by the anisotropy. Based on the law of approach (LoA) to saturation [3], for $H >> H_C$ the dependence of magnetization M on the applied field at high-field strengths for M near the saturation magnetization M_S can be approximated by

$$M = M_S\left(1 - \frac{b}{H^2}\right) + \kappa H \qquad (1)$$

where the first term on the right-hand side is the familiar term which depends on rotation of magnetization against anisotropy, and the κH represents the forced magnetization contribution. The closed parts of the major hysteresis loops were fitted by the LoA (1) in order to determine the parameters M_S, b, and κ. For temperatures above 150 K, the best values of M_S, b and κ were determined using only the parts of the curves with fields higher than 1 T. For temperatures below 150 K, it was found that the forced magnetization term was negligible, (i.e., $\kappa = 0$), and consequently M_S and b were the only parameters used to compare (1) to the data. In these cases, only the parts of the magnetization curves with fields higher than 2.5 T were used for the fitting.

The values of saturation magnetization M_S computed by fitting (1) to the experimental data were found to be approximately the same as the measured maximum magnetization values under a magnetic field of 4×10^6 A.m^{-1} ($\mu_0 H = 5$ T), except for temperatures above 150 K where the maximum magnetization measured was larger than M_S by several percent due to the occurrence of forced magnetization.

Parameter b is related to the magnetocrystalline anisotropy of the material and to a microscopic coefficient which depends on the crystal structure. Since the samples have a cubic structure, the magnitude of the first-order cubic anisotropy coefficient K_1 can be determined from b by the following [3]:

$$K_1 = \mu_0 M_S \sqrt{\frac{105}{8} b}. \qquad (2)$$

The temperature dependence of the calculated anisotropy K_1 for different chromium contents is shown in Fig. 4.

III. DISCUSSION

The anisotropy coefficient K_1 increases with decreasing temperature as shown in Fig. 4, with the steepest increase coming at progressively lower temperatures for increasing Cr content. In general, for fixed values of temperature, anisotropy decreases with increasing Cr content. However, it appears that for temperatures less than 150 K for the pure cobalt ferrite and $x = 0.2$ Cr samples, even a field of 5 T is not enough to saturate the samples, as shown by the apparent change in the slope dK_1/dT for these compositions below 150 K. Therefore, in these cases, anisotropy cannot be computed correctly by this method. Estimation of H_k for CoFe_2O_4, for example, shows that indeed for $T < 150$ K, $\mu_0 H_K > 5$ T [5]. Experimental results on pure cobalt ferrite by Shenker, whose methods utilized torque measurements on single crystals near their easy axes [4], support our conclusions.

A comparison with a recent study on anisotropy of $\text{CoMn}_x\text{Fe}_{2-x}\text{O}_4$ with $0 \leqslant x \leqslant 0.6$ [5] shows that substitution of Cr in general decreases anisotropy faster than substitution of Mn. According to the one-ion model (see, for example, [3]), Co^{2+} ions in the octahedral sites (B-sites) of the spinel structure are responsible for high anisotropy of cobalt ferrite. As we substitute Mn^{3+} or Cr^{3+} for Fe^{3+}, they apparently tend to displace Co^{2+} from the octahedral sites (B-sites) to the tetrahedral sites (A-sites) as Mossbauer spectroscopy studies of these compositions have indicated [6], [7]. Moreover, these Mossbauer results also support the hypothesis that in general Cr^{3+} has an even stronger B-site preference than Mn^{3+}, and displaces more of the Co^{2+} from the B to the A sites. This could explain the more pronounced decrease in the magnetic anisotropy for Cr substituted than for Mn substituted cobalt ferrites which was observed.

IV. SUMMARY AND CONCLUSION

The effect of Cr substitution on the temperature dependence of the magnetic anisotropy of polycrystalline cobalt–ferrite specimens of composition $\text{CoCr}_x\text{Fe}_{2-x}\text{O}_4 (0 \leqslant x \leqslant 0.8)$ was investigated for temperatures in the range 10–400 K. First-order magnetic anisotropy coefficients were calculated from the data using fitting of the high-field parts of the major hysteresis loops to the law of approach. It was found that the anisotropy of all Cr-substituted cobalt ferrites increased substantially with decreasing temperature. It was also found that for a fixed temperature the anisotropy in general decreased with increasing Cr content and this effect was even more pronounced than for Mn substitution [5]. The possible explanation, which takes into account the one-ion anisotropy model and our interpretation of recent Mossbauer spectroscopy measurements [6], [7], states that Cr^{3+} appears to have an even stronger octahedral site preference than Mn^{3+}, and displaces more of the Co^{2+} from the octahedral to the tetrahedral sites. As in the case of Mn substitution, it was concluded that for temperatures below 150 K the anisotropy for the CoFe_2O_4 and $\text{CoCr}_{0.2}\text{Fe}_{1.8}\text{O}_4$ samples was so high that the applied magnetic field of 4×10^6 $\text{A.m}^{-1} (\mu_0 H = 5$ T) was not enough to saturate the samples and, therefore, in these cases the anisotropy coefficient cannot be computed correctly by this method.

ACKNOWLEDGMENT

This work was supported by the National Science Foundation, Division of Materials Research, under Grant DMR-0402716 and Grant OISE-0437293, and by the National Aeronautical and Space Administration under Award NAG-1-02098. This work was also supported in part by the U.S. Department of Energy (DOE), Office of Basic Energy Sciences, Materials Sciences Division. Ames Laboratory is operated for the U.S. DOE by Iowa State University (ISU) under Contract W-7405-ENG-82.

REFERENCES

[1] Y. Chen, J. E. Snyder, C. R. Schwichtenberg, K. W. Dennis, R. W. McCallum, and D. C. Jiles, "Metal-bonded Co-ferrite composites for magnetostrictive torque sensor applications," *IEEE Trans. Magn.*, pt. 2, vol. 35, no. 5, pp. 3652–3654, Sep. 1999.

[2] J. A. Paulsen, A. P. Ring, C. C. H. Lo, J. E. Snyder, and D. C. Jiles, "Manganese-substituted cobalt ferrite magnetostrictive materials for magnetic stress sensor applications," *J. Appl. Phys.*, vol. 97, pp. 044 502-1–044 502-3, 2005.

[3] S. Chikazumi, *Physics of Ferromagnetism*. London, U.K.: Oxford Univ. Press, 1997, pp. 502–504.

[4] H. Shenker, "Magnetic anisotropy of cobalt ferrite ($\text{Co}_{1.01}\text{Fe}_{2.00}\text{O}_{3.62}$) and nickel cobalt ferrite ($\text{Ni}_{0.72}\text{Fe}_{0.20}\text{Co}_{0.08}\text{Fe}_2\text{O}_4$)," *Phys. Rev.*, vol. 107, pp. 1246–1249, 1957.

[5] Y. Melikhov, J. E. Snyder, D. C. Jiles, A. P. Ring, J. A. Paulsen, C. C. H. Lo, and K. W. Dennis, "Temperature dependence of magnetic anisotropy in Mn-substituted cobalt ferrite," *J. Appl. Phys.*, 2006.

[6] K. Krieble, T. Schaeffer, J. A. Paulsen, A. P. Ring, C. C. H. Lo, and J. E. Snyder, "Mossbauer spectroscopy investigation of Mn-substituted Co-ferrite ($\text{CoMn}_x\text{Fe}_{2-x}\text{O}_1$)," *J. Appl. Phys.*, vol. 97, pp. 10F101-1–10F101-3, 2005.

[7] K. Krieble, C. C. H. Lo, Y. Melikhov, and J. E. Snyder, "Investigation of Cr substitution in Co-Ferrite ($\text{CoCr}_x\text{Fe}_{2\ x}\text{O}_4$) using Mossbauer spectroscopy," *J. Appl. Phys.*, 2006, to be published.

Manuscript received March 13, 2006 (e-mail: melikhov@cardiff.ac.uk).

JOURNAL OF APPLIED PHYSICS **101**, 023918 (2007)

Magnetic structures in $Pr_6Ni_2Si_3$ and $Pr_5Ni_2Si_3$

D. C. Jiles[a]
Wolfson Centre for Magnetics, Cardiff University, Cardiff CF24 3AA, United Kingdom

S. H. Song
Materials Science and Engineering Department, Iowa State University, Ames, Iowa 50011 and Materials and Engineering Physics Program, Ames Laboratory, Ames, Iowa 50011

(Received 27 June 2006; accepted 7 September 2006; published online 30 January 2007)

The temperature dependence of magnetization in $Pr_6Ni_2Si_3$ and $Pr_5Ni_2Si_3$ compounds has been studied with the objective of providing a theoretical understanding of the behavior of the magnetic properties of the material. The ternary Pr–Ni–Si system contains the homologous series of compounds $R_{(n+2)(n+1)}Ni_{n(n-1)+2}Si_{n(n+1)}$, where R is a rare earth element which provides a range of materials with different but related structures. The crystal structures and unit cells of $Pr_6Ni_2Si_3$ ($n=2$) and $Pr_5Ni_2Si_3$ ($n=3$) compounds are closely related consisting of an overall hexagonal structure comprising trigonal columns of atoms, in which the only difference is in the size of the triangular base of the column which depends directly on the chemical composition, specifically the index n. The calculations were based on a nearest neighbor exchange interaction approximation under two kinds of conditions: collinear and noncollinear magnetic structures. The results of these calculations show the Curie temperature, but do not yet predict quantitatively the spin reorientation transition at lower temperatures. © *2007 American Institute of Physics*. [DOI: 10.1063/1.2388043]

I. INTRODUCTION

A "model system" in materials science needs to satisfy at least three conditions: (1) the system must be simple enough that there are only a few dominant factors which influence the physical property to be studied or predicted, (2) the factors (such as composition, crystal structure, temperature, pressure, or exchange interaction) that are ultimately responsible for the physical phenomena can be controlled in a well defined way so that their effects can be studied independently, and (3) the predictions obtained from the model system should be testable. To be useful the results should be applicable to other related cases. In this respect the Pr–Ni–Si alloy system can serve as a model system for the study of structure/property relationships in magnetic materials.

The ternary Pr–Ni–Si alloy system is one member of a more general system of alloys and compounds which form a homologous series of the type $R_{(n+2)(n+1)}Ni_{n(n-1)+2}Si_{n(n+1)}$, where R is a rare earth element. Pr–Ni–Si provides a range of materials with different structures as described by Rogl.[1] Overall the alloy system exhibits a hexagonal crystal structure formed of subassemblies of trigonal prismatic columns. The number of smaller triangular arrays that fits along each side to form the basal plane of the larger trigonal prism of the unit cell is determined by the value of n in the chemical formula. Identifiable compounds "$Pr_6Ni_2Si_3$" ($n=2$), "$Pr_5Ni_2Si_3$" ($n=3$), and "$Pr_{15}Ni_7Si_{10}$" ($n=4$) have been prepared and are members of this series.

The trigonal prisms containing the local arrays of Pr atoms can be considered as "magnetic clusters." The size of these clusters can be controlled by selection of the chemical composition. As the chemical composition changes (and hence the size of the magnetic clusters changes), the number of nearest neighbors (and hence the exchange interactions) for each Pr atom site also changes systematically. Therefore the physical properties vary systematically from one member of the series to the next.

Experimental results on the magnetic properties of $Pr_5Ni_2Si_3$ and $Pr_{15}Ni_7Si_{10}$ polycrystalline samples and a $Pr_5Ni_2Si_3$ single crystal sample have recently been reported.[2–6] Each compound showed two magnetic phase transitions: a magnetic order/disorder transition at a higher temperature (41 K for $Pr_5Ni_2Si_3$, and 58 K for $Pr_{15}Ni_7Si_{10}$) and another transition, which exhibits the characteristics of spin reorientation transition, at a lower temperature (25 K for $Pr_5Ni_2Si_3$ and 31 K for $Pr_{15}Ni_7Si_{10}$).

The present paper reports on the theoretical investigation to attempt to explain the temperature dependent magnetization of $Pr_6Ni_2Si_3$ ($n=2$) and $Pr_5Ni_2Si_3$ ($n=3$) compounds. The calculations are based on a nearest neighbor exchange interaction approximation under two kinds of conditions: collinear and noncollinear magnetic structures. The crystal structures and unit cells of $Pr_6Ni_2Si_3$ and $Pr_5Ni_2Si_3$ compounds are shown in Figs. 1(a) and 1(b), respectively.

II. THEORETICAL BASIS FOR MODEL CALCULATIONS

In order to calculate the expected variation of magnetization with temperature (M vs T) in Pr–Ni–Si single crystal, the exchange interaction energy for each atomic site was determined using a nearest neighbor exchange interaction approximation. For this calculation, the following were assumed:

(1) Only the Pr atoms have a magnetic moment and therefore only these atoms contribute to magnetization.
(2) The magnetic moment per Pr atom is $3.58\mu_B$.

---

[a] Electronic mail: jilesd@cf.ac.uk

0021-8979/2007/101(2)/023918/7/$23.00

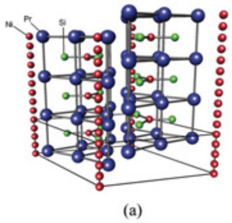

FIG. 1. (Color online) Crystal structure and unit cell of (a) $Pr_6Ni_2Si_3$ ($n=2$) and (b) $Pr_5Ni_2Si_3$ ($n=3$) showing the trigonal cells which form prismatic columnar assemblies. [Note that in the case of $Pr_5Ni_2Si_3$ there are additional Ni atoms not shown here for the purposes of simplicity. These lie at the corner of the rhombohedra containing the two trigonal prisms and amount to one extra Ni atom per trigonal plane as shown in (a).]

(3) The exchange interaction exists only between the nearest neighbors, which is expressed in terms of the exchange energy according to the following equation:

$$E_{\mathrm{ex}} = -2J_{\mathrm{NN}}\sum_{i,j} J_i J_j, \tag{1}$$

where J_{NN} is the exchange interaction coefficient between nearest neighbors and J_i and J_j are the total angular momentum at the ith and jth sites, respectively.

A. $Pr_6Ni_2Si_3$

For the purposes of calculation the arrangement of Pr atoms in the crystal structure was transformed into an orthogonal coordinate system as shown in Fig. 2(a), from which the distances between various Pr atom pairs were calculated. The results show that the distances vary between the different types of Pr atom pairs. The Pr atoms less than 0.5 nm apart were selected as "nearest neighbors" for the purposes of these calculations. The specific atomic position and the distances of nearest neighbors from each type of Pr atom are shown in Table I. The Pr atoms in the triangular base plane of the columnar structure of $Pr_6Ni_2Si_3$ compound can be classified into two groups depending on the number of nearest neighbors that they have among Pr atoms. It can be shown that Pr atoms along the edges of the triangular plane have ten nearest neighbors and those at the corners of the triangular plane have 12 nearest neighbors. The arrangement of Pr atoms in the base plane of the $Pr_6Ni_2Si_3$ compound is shown in Fig. 2(b). The three-dimensional arrangement of nearest neighbor Pr atoms is shown in Fig. 3 for (a) "edge" and (b) "corner" atoms.

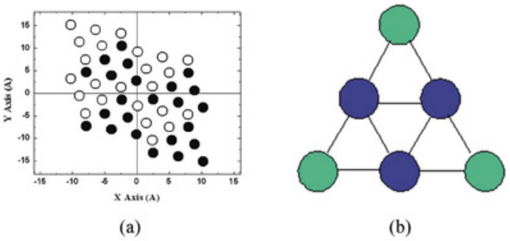

FIG. 2. (Color online) (a) The projection of Pr atoms on the base plane in the crystal structure of $Pr_6Ni_2Si_3$ compound. The solid and open circles indicate the Pr atoms in successive planes, above and below, the distance between which is half of the unit cell's height along the c axis, respectively. (b) Diagram of the trigonal base plane in $Pr_6Ni_2Si_3$ showing two types of Pr atoms—green and blue circles indicate "corner" and "edge" atoms, respectively.

The average exchange interaction energy between nearest neighbors was calculated based on the experimentally measured Curie temperature (T_C=40 K),[7]

$$E_{\mathrm{ex}}^{\mathrm{triangle}} = 3J_{\mathrm{NN}}\sum_{i,j}^{\text{edge atom}} J_i J_j + 3J_{\mathrm{NN}}\sum_{i,j}^{\text{corner atom}} J_i J_j, \tag{2}$$

where $E_{\mathrm{ex}}^{\mathrm{triangle}}$ is the total exchange energy for each triangular base plane in the unit cell, such as the one shown in Fig. 2(b). This energy corresponds to $18k_BT_C$, the thermal energy that six Pr atoms in the triangular base plane have at the Curie temperature in order to cause the transition from a ferromagnetic to a paramagnetic state (6 Pr atoms × $3k_BT_C$).

TABLE I. The atomic positions and the distances of nearest neighbors from each type of Pr atom in $Pr_6Ni_2Si_3$.

Type of Pr atom	Atomic position of nearest neighbor	Distance (Å)	Type of Pr atom	Atomic position of nearest neighbor	Distance (Å)
Corner atom (with 12 nearest neighbor Pr atoms)	Two corner atoms on neighboring columns 1/2 plane up	3.53	Edge atom (with ten nearest neighbor Pr atoms)	One corner atom on neighboring column 1/2 plane up	3.70
	Two corner atoms on neighboring columns 1/2 plane down	3.53		One corner atom on neighboring column 1/2 plane down	3.70
	One edge atom on neighboring columns 1/2 plane up	3.70		One edge atom on neighboring column 1/2 plane up	3.78
	One edge atom on neighboring columns 1/2 plane down	3.70		One edge atom on neighboring column 1/2 plane down	3.78
	Two edge atoms in the same column and plane	4.0		Two corner atoms in the same column and plane	4.0
	Two corner atoms on neighboring columns in the same plane	4.85		Two edge atoms in the same column and plane	3.64
	One corner atom in the same column, the next plane up	4.28		One edge atom in the same column, the next plane up	4.28
	One corner atom in the same column, the next plane down	4.28		One edge atom in the same column, the next plane down	4.28

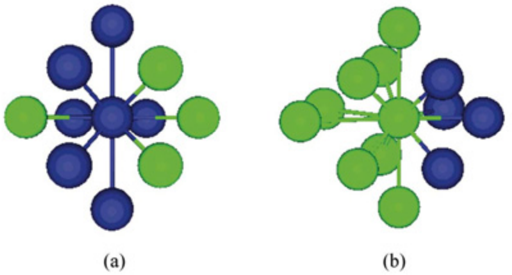

FIG. 3. (Color online) Arrangement of nearest neighbor Pr atoms around (a) edge and (b) corner atoms in $Pr_6Ni_2Si_3$. Green and blue circles indicate corner and edge Pr atoms, respectively.

Since the effective magnetic field that each atom experiences depends on the number of nearest neighbors for each site, the effective magnetic field for each atomic site can be expressed as

$$E_{\mathrm{ex}}^{\mathrm{site}} = -J_{\mathrm{NN}}\sum_{i,j}^{\mathrm{site}} J_iJ_j = m\mu_0 H_{\mathrm{eff}}^{\mathrm{site}} = m\mu_0\alpha_{\mathrm{site}}M, \tag{3}$$

where $H_{\mathrm{eff}}^{\mathrm{site}}$ is the exchange field for each site and α_{site} is the mean field coefficient for each site. Assuming that the exchange field can be rewritten in the form $H_{\mathrm{eff}}^{\mathrm{site}}=\alpha_{\mathrm{site}}M$, the total magnetic moment per triangular base plane can be expressed as the vector sum of all the edge (e) and corner or apex (a) moments in the base plane,

$$\begin{aligned} m^{\mathrm{triangle}} = m^e + m^a = 3m_0 B_J\left[\frac{m_0\mu_0(H+H_{\mathrm{eff}}^e)}{k_BT}\right] \\ + 3m_0 B_J\left[\frac{m_0\mu_0(H+H_{\mathrm{eff}}^a)}{k_BT}\right], \end{aligned} \tag{4}$$

where m^e is the sum of magnetic moments of the three Pr atoms located on the edges in the trigonal base plane, m^a is the sum of magnetic moments of the three Pr atoms located on the corners in the trigonal base plane, and $B_J(x)$ is the Brillouin function,

$$B_J(x) = \left(\frac{2J+1}{2J}\right)\coth\left[\frac{(2J+1)x}{2J}\right] - \left(\frac{1}{2J}\right)\coth\left(\frac{x}{2J}\right). \tag{5}$$

B. $Pr_5Ni_2Si_3$

Calculations for the $Pr_5Ni_2Si_3$ compound have been performed in two different ways based on two different assumptions: (a) collinear alignment and (b) noncollinear alignment of magnetic moments. The calculation procedure for collinear magnetic moments is analogous to that for the $Pr_6Ni_2Si_3$ compound, although the structure of $Pr_5Ni_2Si_3$ is more complicated than $Pr_6Ni_2Si_3$. The Pr atoms in the triangular base plane of the columnar structure of $Pr_5Ni_2Si_3$ ($n=3$) compound were classified into three groups, corner (or apex) a, edge e, and center c depending on the number of nearest neighbor Pr atoms.

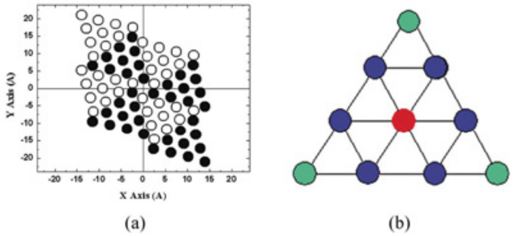

FIG. 4. (Color online) (a) The projection of Pr atoms on the base plane in the crystal structure of $Pr_5Ni_2Si_3$ ($n=3$) compound. The solid and open circles indicate the Pr atoms in the successive array of planes, above and below, the distance between which is half of the unit cell's height along the c axis. (b) Diagram of the trigonal base plane in $Pr_5Ni_2Si_3$ showing three types of Pr atoms—green, blue, and red circles indicate the corner, edge, and center atoms, respectively.

For the purposes of calculation the arrangement of Pr atoms in the crystal structure was transformed into an orthogonal coordinate system as shown in Fig. 4(a), from which the distances between various Pr atom pairs were calculated. Pr atoms at the center sites of the triangular plane have eight nearest neighbors, those along the edges of the triangular plane have ten nearest neighbors, and those at the corners of the triangular plane have 12 nearest neighbors. This is shown in Figs. 4(a) and 4(b). Figure 5 and Table II show the atomic arrangement and distances of each type of Pr atom from the nearest neighbors, respectively.

1. Collinear alignment

The exchange interaction energy is calculated from the equation

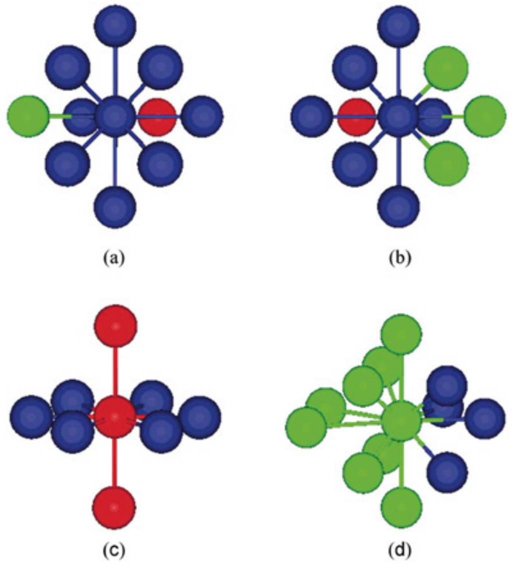

FIG. 5. (Color online) Arrangement of nearest neighbor Pr atoms around the (a) edge (A), (b) edge (B), (c) center, and (d) corner Pr atoms in $Pr_5Ni_2Si_3$ ($n=3$) compound. Green, blue, and red circles indicate corner, edge, and center, Pr atoms, respectively.

TABLE II. The atomic positions and the distances of nearest neighbors from each type of Pr atom in $Pr_5Ni_2Si_3$.

Type of Pr atom	Atomic position of nearest neighbor	Distance (Å)	Type of Pr atom	Atomic position of nearest neighbor	Distance (Å)
Corner atom (with 12 nearest neighbor Pr atoms)	Two corner atoms on neighboring columns 1/2 plane up	3.51	Center atom (with 8 nearest neighbor Pr atoms)	Six edge atoms in the same column and plane	3.82–3.88
	Two corner atoms on neighboring columns 1/2 plane down	3.51			
	One edge atom on neighboring column 1/2 plane up	3.70		One center atom in the same column, the next plane up	
	One edge atom on neighboring column 1/2 plane down	3.70			
	Two edge atoms in the same column and plane	4.05		One center atom in the same column, the next plane down	
	Two corner atoms on neighboring columns, in the same plane	4.84			
	One corner atom in the same column, the next plane up	4.25	Edge (B) atom (with ten nearest neighbor Pr atoms)	One corner atom on neighboring column 1/2 plane up	3.70
	One corner atom in the same column, the next plane down	4.25		One corner atom on neighboring column 1/2 plane down	3.70
Edge (A) atom (with ten nearest neighbor Pr atoms)	Two edge atoms on neighboring columns 1/2 plane up	3.80		One edge atom on neighboring column 1/2 plane up	3.80
	Two edge atoms on neighboring columns 1/2 plane down	3.80		One edge atom on neighboring column 1/2 plane down	3.80
	One corner atom in the same column and plane	4.05		Two edge atoms in the same column and plane	3.63/4.07
	Two edge atoms in the same column and plane	3.63/4.05		One center atom in the same column and plane	3.82
	One center atom in the same column and plane	3.88		One corner atom in the same column and plane	4.05
	One edge atom in the same column, the next plane up	4.25		One edge atom in the same column, the next plane up	4.25
	One edge atom in the same column, the next plane down	4.25		One edge atom in the same column, the next plane down	4.25

$$E_{\mathrm{ex}} = -2J_{\mathrm{NN}}\sum_{i,j} J_i J_j \cos\theta_{i,j}, \tag{6}$$

where θ is the angle between magnetic moments at ith and jth sites. The total exchange interaction energy per unit triangular plane can be obtained using the measured Curie temperature (T_C),

$$E_{\mathrm{ex}}^{\mathrm{triangle}} = 1J_{\mathrm{NN}} \sum_{i,j}^{\text{center atom}} J_i J_j + 6J_{\mathrm{NN}} \sum_{i,j}^{\text{edge atom}} J_i J_j + 3J_{\mathrm{NN}} \sum_{i,j}^{\text{corner atom}} J_i J_j = 30 k_B T_C. \tag{7}$$

Based on this equation the magnetization versus temperature curve (M vs T) was calculated following the same method as in the $Pr_6Ni_2Si_3$ case. It should be noted that the exchange energy for each atom depends on its location in the triangular plane because of the different numbers of nearest neighbors. This means that different Pr atoms in the triangular base plane will have their magnetic moments held in their orientations with different energies depending on their location in the plane.

2. Noncollinear alignment

The calculation for noncollinear magnetic moments is significantly more complicated than for collinear moments. In order to perform this calculation the Pr atoms in the lattice need to be classified into four separate groups, although the number of nearest neighbor Pr atoms per site remains the same as for the collinear case. According to neutron diffraction data,[8] the component of the magnetic moment of the corner Pr atom along the c axis is $0.72\mu_B$, which can be interpreted to mean that the magnetic moments of the corner atoms are tilted 78° away from the c axis. From this the angles between the magnetic moments for each Pr site were calculated and these were then included in the subsequent calculation of the exchange interaction energy using Eq. (6) above.

Considering these noncollinear effects on the exchange interaction energy, the edge atoms can be further classified into two subgroups based on the fact that the angle between magnetic moments of "edge-corner" atom pairs is different than that of "edge-edge" atom pairs, and that "edge (A)" and "edge (B)" atoms have different combinations of nearest neighbor Pr atoms. For edge (A) type there are eight edge/one center/one corner nearest neighbor atoms while for edge (B) type there are six edge/one center/three corner nearest neighbor atoms. Therefore for the noncollinear calculation the contribution to total exchange energy for each atom is not a simple linear function of the number of nearest neighbors for each site, but a more complicated function of two variables, N (the number of nearest neighbors) and θ (the relative angle of orientation between neighboring pairs). Figure 5 and

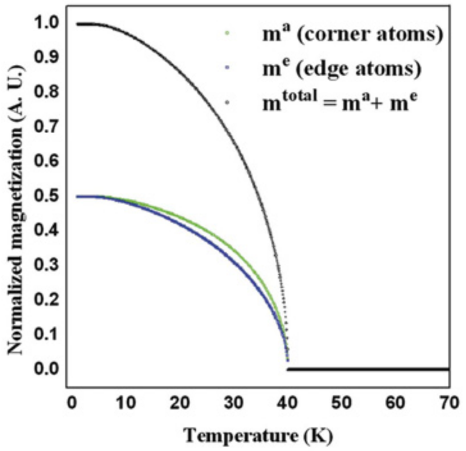

FIG. 6. (Color online) Calculated M vs T curves using Brillouin functions for the $Pr_6Ni_2Si_3$ compound. Green and blue symbols represent the magnetization due to the Pr atoms at corner and edge sites, respectively. The black symbols are the sum of these two contributions, which correspond to the total magnetization.

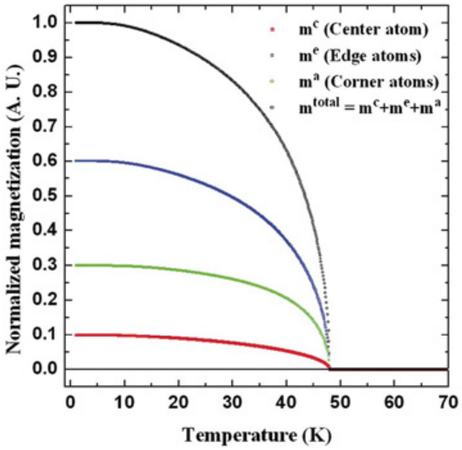

FIG. 7. (Color online) Calculated M vs T curves using Brillouin functions for the $Pr_5Ni_2Si_3$ compound with collinear magnetic moments. Red/blue/green symbols represent the magnetization due to the Pr atoms at the center/edge/corner sites, respectively. The black symbols are the sum of these three contributions, which correspond to the resultant total magnetization of this compound.

Table II were used to determine how many nearest neighbor atoms should be used in the calculation. The total exchange interaction energy per triangular base plane was then calculated as follows:

$$\begin{aligned} E_{\mathrm{ex}}^{\mathrm{triangle}} &= E_{\mathrm{ex}}^{\mathrm{center}} + E_{\mathrm{ex}}^{\mathrm{edge\ A}} + E_{\mathrm{ex}}^{\mathrm{edge\ B}} + E_{\mathrm{ex}}^{\mathrm{corner}} \\ &= 1J_{\mathrm{NN}} \sum_{i,j}^{\mathrm{center\ atom}} J_i J_j \cos\theta_{i,j} \\ &\quad + 3J_{\mathrm{NN}} \sum_{i,j}^{\mathrm{edge\ A\ atom}} J_i J_j \cos\theta_{i,j} \\ &\quad + 3J_{\mathrm{NN}} \sum_{i,j}^{\mathrm{edge\ B\ atom}} J_i J_j \cos\theta_{i,j} \\ &\quad + 3J_{\mathrm{NN}} \sum_{i,j}^{\mathrm{corner\ atom}} J_i J_j \cos\theta_{i,j} = 30k_B T_C. \end{aligned} \tag{8}$$

III. RESULTS AND DISCUSSIONS

A. $Pr_6Ni_2Si_3$

The calculated magnetization versus temperature (M vs T) curves for each type of Pr atom as well as the total resultant magnetic moment for $Pr_6Ni_2Si_3$ are shown in Fig. 6. The magnetization curve for each type of Pr atom in the triangular base plane has been presented in terms of normalized magnetization compared with the total magnetization. The calculated M vs T curve for each type of Pr atom is indicated with green (corner) and blue (edge) symbols and the total magnetization curve with black symbols. All curves show a monotonic decrease of M with T over the entire range of temperature and a Curie temperature of 40 K which is consistent with the experimentally measured value. However, the rate of decrease in magnetization with temperature is different for each type of Pr atoms. Magnetization for edge atoms decreases faster with temperature than for corner atoms. This is due to the difference in number of nearest neighbor exchange interactions for the two different types of Pr atom, ten for edge atoms and 12 for corner atoms, thus making a difference in the exchange field ($H_{\mathrm{eff}}^{\mathrm{site}}$) for the different atomic sites.

B. $Pr_5Ni_2Si_3$

1. Collinear magnetic moments

The calculated magnetization versus temperature (M vs T) curves for each of the different types of Pr atoms as well as the total magnetic moments for $Pr_5Ni_2Si_3$ compound have been calculated using the same method as with the $Pr_6Ni_2Si_3$ case, based on the assumption that all magnetic moments are collinear. The calculated M vs T curves are shown in Fig. 7, in which the red/blue/green symbols represent the contributions of center/edge/corner atoms to the magnetization, and the black symbols represent the resultant total magnetization. The results show a monotonic decrease of M with T over the entire range of temperature. This is similar to that of the $Pr_6Ni_2Si_3$ compound. The calculated Curie temperature of 48 K is consistent with the experimentally measured value. The rate of decrease in magnetization with temperature is different for each of the different types of Pr atom, which is due to the difference in the number of nearest neighbors for each of the different types of Pr site leading to a difference in the exchange field ($H_{\mathrm{eff}}^{\mathrm{site}}$) for the different atomic sites

2. Noncollinear magnetic moments

The experimentally determined magnetization versus temperature (M vs T) curves of $Pr_5Ni_2Si_3$ single crystal are shown in Figs. 8(a) and 8(b), where M was measured (a)

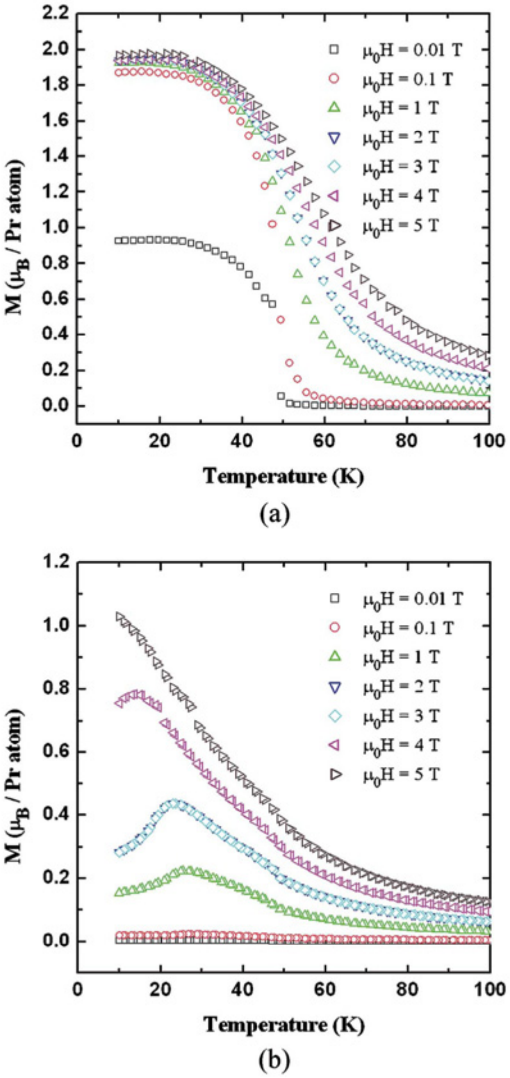

FIG. 8. (Color online) Variation of the magnetization of $Pr_5Ni_2Si_3$ single crystal with temperature, measured (a) parallel $M_{\parallel c}$ and (b) perpendicular $M_{\perp c}$ to the c axis under various strengths of applied magnetic field (Ref. 7).

parallel and (b) perpendicular to the c axis using a superconducting quantum interference device (SQUID) magnetometer.[7] These magnetizations are shown in terms of the net number of Bohr magnetons per Pr atom. The magnetic moment per Pr atom in the single ion state is 3.58 μ_B. In the condensed matter state the value of this moment is likely to be different as indicated by preliminary experimental measurements using neutron diffraction.[8] In fact it appears that the Pr atoms on each of the three different types of lattice sites have different magnetic moments.

The fact that the maximum value of magnetization under a field of $\mu_0 H=5$ T was 55% of expected saturation for the component of magnetization parallel to the c axis $M_{\parallel c}$ and 29% of expected saturation for the component of magnetization perpendicular to the c axis $M_{\perp c}$ indicates that the values of magnetization measured in both directions are not saturated even at a field of $\mu_0 H=5$ T and that the easy axis may be closer to the c axis than to the base plane. This can be explained by considering the atomic arrangement of Pr atoms. In the case of a Pr atom at the corner site, the Pr atom has 12 nearest neighbors as shown in Fig. 5(d). This also shows that the atomic arrangement of nearest neighbors around the Pr atom at the corner site is not symmetric and further suggests that the magnetic moments at the corner Pr atoms will tend to be tilted away from the c axis.

These predictions are also consistent with the neutron diffraction data which indicate that the component of magnetic moment along the c axis of the Pr atom at the corner site is $0.72\mu_B$. This could be interpreted to mean that the magnetic moment of the corner atoms is tilted 78° away from the c axis. Based on this the possible angles between the magnetic moments for each site were calculated and these were included in the calculation of the exchange interaction energy using Eq. (6).

The expected M vs T curves for each type of Pr atom were calculated. The results are shown in Fig. 9(a), which predicts a consistent Curie temperature for all sites, which agrees with the experimental results shown in Fig. 8. From results of the calculated M vs T curves shown in Fig. 9(a) the expected variation with temperature of the average angle of magnetic moment relative to the c axis for each type of Pr atom has been calculated and is shown in Fig. 9(b).

When it comes to the experimentally measured $M_{\perp c}$-T curve shown in Fig. 8(b), a local maximum in magnetization was observed around 25 K under an applied magnetic field of 1 T and the transition temperature where the local maximum occurred was lowered as the magnitude of the applied magnetic field increased. According to the understanding achieved in the present work this behavior is considered to be due to the asymmetric exchange interactions at the corner sites. Symmetry arguments show that the direction of the component of magnetic moment of the corner atom in the base plane should be along the direction of broken symmetry, which is indicated for the different corner atoms in Fig. 10. As a consequence, when the temperature decreases below a critical temperature (the spin reorientation temperature) the magnetic moments of the Pr atoms in the base plane reorient in such a way that they partially cancel each other out, thus reducing the component of resultant total magnetization in the plane.

IV. CONCLUSIONS

The variation of magnetization with temperature of $Pr_6Ni_2Si_3$ and $Pr_5Ni_2Si_3$ single crystal alloys has been calculated using a nearest neighbor exchange interaction approximation. In $Pr_6Ni_2Si_3$ two types of Pr atoms were classified, "corner" and "edge," based on the number of nearest neighbors. In $Pr_5Ni_2Si_3$ three types of Pr atoms were classified, "corner," "edge," and "center," based on the number of nearest neighbors.

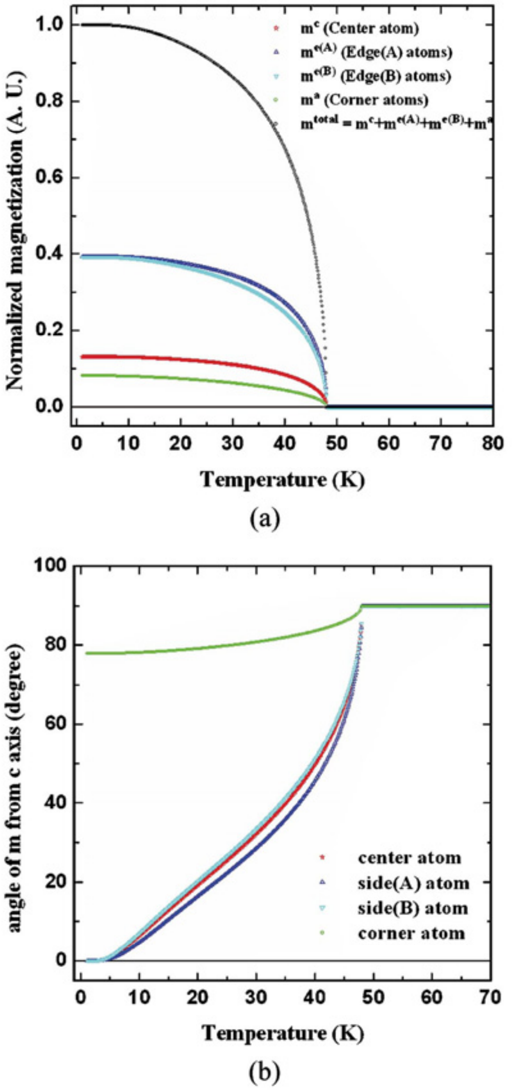

(a)

(b)

FIG. 9. (Color online) (a) Calculated *M* vs *T* curves for the $Pr_5Ni_2Si_3$ compound. Red/blue/cyan/green symbols represent the magnetization due to the Pr atoms at the center/edge(A)/edge(B)/corner sites, respectively. The black symbols are the sum of these four contributions, which correspond to the total magnetization of this compound. (b) The expected variation with temperature of the angle θ relative to the c axis of magnetic moments for each of the different types of Pr atom.

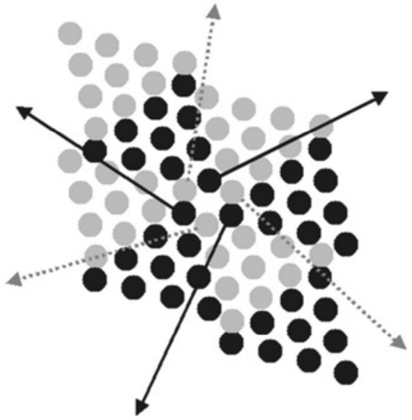

FIG. 10. Atomic arrangement of Pr atoms in the $Pr_5Ni_2Si_3$ compound. The arrows from the corner atoms indicate the direction in which the symmetry of the exchange interaction at the corner atom is broken.

Magnetization versus temperature (*M* vs *T*) curves for each type of atom were calculated as well as the average magnetization versus temperature (*M* vs *T*) curve for the whole trigonal array. The calculations predicted Curie temperatures of 40 K for $Pr_6Ni_2Si_3$ and 48 K for $Pr_5Ni_2Si_3$, which are in agreement with experimental results, but with different temperature dependences of magnetization for the different types of Pr atoms on corner, edge, and center sites. The results also showed that components of magnetic moments of Pr atoms at the corner sites have preferred orientation in the base plane with a sixfold symmetry. This sixfold preferred orientation in the base plane causes the component of magnetic moment in the base plane of each corner site to be partially canceled by the base plane components of magnetic moment of the other corner atoms, so that the resultant total magnetization was decreased. The critical temperature at which this occurs causes the second, or spin reorientation, transition to occur at about 25 K in $Pr_5Ni_2Si_3$, which has been observed experimentally.

ACKNOWLEDGMENTS

This research was supported by a Wolfson Research Fellowship from the Royal Society of the United Kingdom and by the U.S. Department of Energy, Office of Basic Energy Sciences, Materials Sciences Division. Ames Laboratory is operated for the U. S. Department of Energy by Iowa State University under Contract No. W-7405-ENG-82. The authors wish to thank Dr. R. W. McCallum for discussions concerning the results of this research.

[1] P. Rogl, in *Handbook of the Physics and Chemistry of Rare Earths*, edited by K. A. Gschneidner, Jr. and L. R. Eyring (North-Holland, Amsterdam, 1987), Vol. 7, p. 1.
[2] A. O. Pecharsky, Y. Mozharivskyj, K. W. Dennis, K. A. Gschneidner, R. W. McCallum, G. J. Miller, and V. K. Pecharsky, Phys. Rev. B **68**, 134452 (2003).
[3] S. H. Song, D. C. Jiles, J. E. Snyder, A. O. Pecharsky, D. Wu, K. W. Dennis, T. A. Lograsso, and R. W. McCallum, J. Appl. Phys. **97**, 10M516 (2005).
[4] S. H. Song, J. E. Snyder, D. Wu, T. A. Lograsso, K. W. Dennis, R. W. McCallum, Y. Janssen, and D. C. Jiles, APS March Meeting, Los Angeles, 21–25 March 2005 (unpublished)
[5] S. H. Song, J. E. Snyder, D. Wu, T. A. Lograsso, K. W. Dennis, R. W. McCallum, Y. Janssen, and D. C. Jiles, IEEE Trans. Magn. **41**, 3499 (2005).
[6] D. C. Jiles *et al.*, J. Magn. Magn. Mater. **299**, 288 (2005).
[7] R. W. McCallum (private communication).
[8] A. Llobet Megias (private communication).

JOURNAL OF APPLIED PHYSICS 97, 10M516 (2005)

Thermal expansion and Gruneisen parameters in some Pr–Ni–Si compounds

S. H. Song,[a] D. C. Jiles, and J. E. Snyder
Materials and Engineering Physics Program, Ames Laboratory, US Department of Energy, Iowa State University, Ames, Iowa 50011 and Department of Materials Science & Engineering, Iowa State University, Ames, Iowa 50011

A. O. Pecharsky, D. Wu, and K. W. Dennis
Materials and Engineering Physics Program, Ames Laboratory, US Department of Energy, Iowa State University, Ames, Iowa 50011

T. A. Lograsso and R. W. McCallum
Materials and Engineering Physics Program, Ames Laboratory, US Department of Energy, Iowa State University, Ames, Iowa 50011 and Department of Materials Science & Engineering, Iowa State University, Ames, Iowa 50011

(Presented on 11 November 2004; published online 16 May 2005)

In this study, the thermal expansion and Gruneisen parameter of polycrystalline "$Pr_5Ni_2Si_3$" and "$Pr_{15}Ni_7Si_{10}$" were investigated over the temperature range of 5–300 K. Calculations of the phonon contribution to thermal expansion were made, which allowed the magnetic contribution to thermal expansion to be calculated from the difference between the total thermal expansion and the phonon contribution. This resulted in a temperature-dependent magnetic contribution to thermal expansion that varied with the magnetic ordering of the material. The results show two magnetic transitions in each compound, the higher temperature transition corresponding to the Curie temperature and the lower temperature transition resulting from a spin reorientation. © *2005 American Institute of Physics.* [DOI: 10.1063/1.1853894]

I. INTRODUCTION

In the study of structure/property relationships in magnetic materials it is advantageous to have materials with closely related but different structures whereby systematic changes in structure can be related to magnetic properties. The ternary Pr–Ni–Si alloy system contains the homologous series $R_{(n+2)(n+1)}Ni_{n(n-1)+2}Si_{n(n+1)}$, where R is a rare earth element, in this case Pr, and provides a range of materials with different structures as described by Rogl[1] We are therefore investigating this series of alloys because it provides a suitable series of related magnetic compounds in which there are systematic changes in the crystal structure from one composition to the next. The Pr series contains the identifiable compounds "$Pr_6Ni_2Si_3$" ($n=2$), "$Pr_5Ni_2Si_3$" ($n=3$), and "$Pr_{15}Ni_7Si_{10}$" ($n=4$). An investigation of a polycrystalline sample of the $n=3$ alloy has recently been reported by Pecharsky *et al.*[2] The present paper reports on an investigation of the properties of polycrystalline $Pr_5Ni_2Si_3$ and $Pr_{15}Ni_7Si_{10}$, in which the results of thermal expansion measurement have been analyzed and compared with the expected thermal expansion contributions due to lattice vibrations in the absence of magnetic ordering. The differences have been attributed to magnetic contributions to the thermal expansion and have been used to locate the temperatures of magnetic phase transitions in these compounds.

II. EXPERIMENTAL METHODS

The polycrystalline samples of $Pr_5Ni_{1.9}Si_3$ and $Pr_{15}Ni_{6.8}Si_{10}$, which will hereafter be referred to by their idealized stoichiometries $Pr_5Ni_2Si_3$ and $Pr_{15}Ni_7Si_{10}$, respectively, were prepared by arc melting in an argon atmosphere from high purity components: Pr (99.9+ at. % pure), Ni (99.88 at. % pure), Si (99.99 at. % pure). Thermal expansion was measured using strain gauges. Measurements were carried out under applied magnetic fields of up to 9 T in the temperature range 5–300 K. A "half bridge" configuration was used to compensate for the temperature and field dependence of the strain gauge resistance which is not caused directly by strain in the sample. The second "dummy" gauge was attached to a copper reference sample, the measured strain being therefore the difference in thermal expansion between the sample and that of copper. The bulk elastic modulus was determined from measurements of acoustic velocity at a temperature of 300 K and the density of the specimens.

III. RESULTS AND DISCUSSIONS

The results of thermal expansion measurements under a zero magnetic field ($H=0$) for polycrystalline $Pr_5Ni_2Si_3$ and $Pr_{15}Ni_7Si_{10}$ are shown in Fig. 1. Anomalies in thermal expansion occurred in the temperature range below 50 K for $Pr_5Ni_2Si_3$ and below 65 K for $Pr_{15}Ni_7Si_{10}$, which are indicative of magnetic phase transitions from a higher temperature paramagnetic state to a lower temperature magnetically ordered state.

The phonon contributions to the heat capacity and thermal expansion were calculated using the Debye–Gruneisen theorem. Specifically, the Debye temperature θ_D was first calculated from the heat capacity data in the high tempera-

---

[a] Electronic mail: song73@iastate.edu

0021-8979/2005/97(10)/10M516/3/$22.50

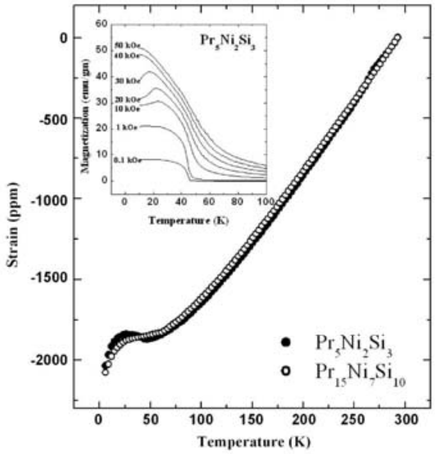

FIG. 1. Temperature-dependent thermal expansion of polycrystalline $Pr_5Ni_2Si_3$ (solid circles) and $Pr_{15}Ni_7Si_{10}$ (open circles) under zero applied magnetic field. The inset shows detailed results of the variation of magnetization with temperature over the range 10–100 K at different constant field strengths.

ture range (100–300 K) where magnetic contributions could be ignored since the material was in a paramagnetic state throughout this temperature range. For this calculation, an approximate equation for the Debye function was used at high temperatures. Values of θ_D were obtained, 201 K for $Pr_5Ni_2Si_3$ and 209 K for $Pr_{15}Ni_7Si_{10}$, respectively, and from these the expected variation of heat capacity with temperature in the absence of magnetic effects was calculated over the whole temperature range. The expected phonon contribution to thermal expansion in the absence of magnetic effects was calculated over the same temperature range as the heat capacity measurements (100–300 K) using the method of Sayetat *et al.*[3] These calculations gave a thermal expansion that varied slowly with temperature as would be expected in the absence of magnetic contributions. The results of these calculations, showing the expected temperature dependence of both heat capacity and thermal expansion coefficient in the absence of magnetic effects, are shown in Fig. 2.

Once the results of heat capacity and thermal expansion in the absence of magnetic effects were calculated the phonon contribution was subtracted from the measured total heat capacity and thermal expansion as shown in Fig. 3. Since the other electronic contributions to these properties are negligible in comparison, the differences are due to the magnetic contributions to the heat capacity and thermal expansion, which are strongly dependent on any changes in the magnetic order. The results indicated magnetic transitions at temperatures of 25 K and 41 K for $Pr_5Ni_2Si_3$, 31 K and 58 K for $Pr_{15}Ni_7Si_{10}$ where rapid changes in these properties occurred.

The variation of thermal expansion coefficient with heat capacity are shown in Fig. 4(a) for both compounds. These show behavior that is consistent with the Gruneisen assumption[4]

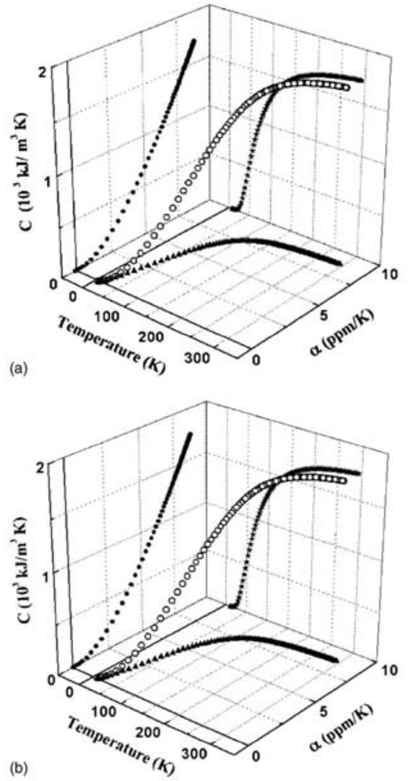

FIG. 2. The calculated phonon contribution to heat capacity and thermal expansion coefficient of polycrystalline (a) $Pr_5Ni_2Si_3$ and (b) $Pr_{15}Ni_7Si_{10}$ using the Debye-Gruneisen theorem. The symbols *, ▲, ● show the projections of the data on the C-T, α-T, and α-C planes, respectively.

$$\alpha = \gamma \frac{C}{3K}, \tag{1}$$

where α is the thermal expansion coefficient, C is the specific heat capacity, K is the bulk elastic modulus, and γ is the Gruneisen parameter. Since the Gruneisen parameter and bulk modulus are relatively insensitive to temperature, the thermal expansion coefficient and heat capacity have essentially a linear relationship.

The bulk modulus K for each compound was calculated from acoustic velocity measurements made at 300 K. The values obtained were 68.9 GPa for $Pr_5Ni_2Si_3$ and 68.6 GPa for $Pr_{15}Ni_7Si_{10}$. The Gruneisen parameter was then calculated for each compound from Eq. (1) using known values of C and α assuming no structural or magnetic changes in the alloys. The results are shown in Fig. 4(b).

Magnetostriction of polycrystalline $Pr_5Ni_2Si_3$ and $Pr_{15}Ni_7Si_{10}$ were measured. The results for these two compounds were very similar[5] and showed a positive magnetostriction at all temperatures in which the amplitude of magnetostriction under a 9 T field decreased with temperature for both samples. Inflection points on the λ-H curve were observed at low temperatures, at 10 K for $Pr_5Ni_2Si_3$ and at

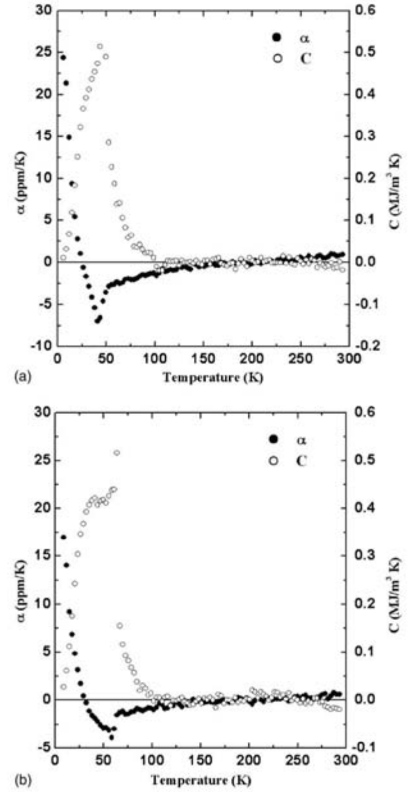

FIG. 3. The magnetic contribution to heat capacity/thermal expansion coefficient obtained from the difference between the total heat capacity/thermal expansion coefficient and the phonon contribution for (a) $Pr_5Ni_2Si_3$ and (b) $Pr_{15}Ni_7Si_{10}$ shown in Fig. 2.

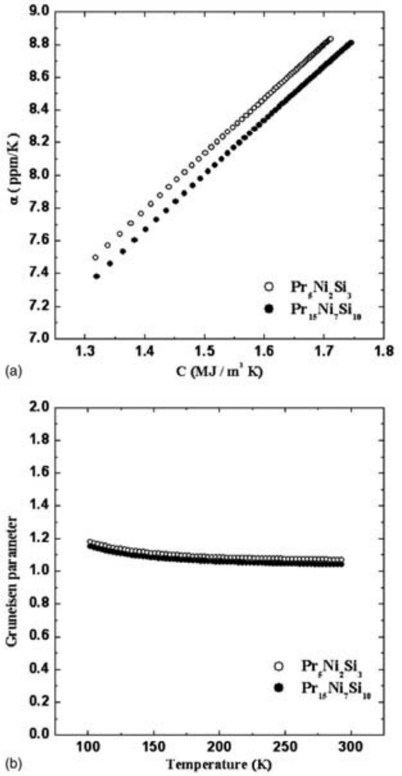

FIG. 4. (a) Comparison of the calculated phonon effect of $Pr_5Ni_2Si_3$ and $Pr_{15}Ni_7Si_{10}$. (b) Comparison of the calculated Gruneisen parameter of $Pr_5Ni_2Si_3$ and $Pr_{15}Ni_7Si_{10}$ with temperature. Bulk moduli for $Pr_5Ni_2Si_3$ and $Pr_{15}Ni_7Si_{10}$ are 68.9 and 68.6 GPa, respectively.

20 K for $Pr_{15}Ni_7Si_{10}$. These are consistent with the existence of magnetic phase transitions at these temperatures. Furthermore, the inflection points in both λ-H and M-H curves occurred under similar applied field strength of around 3 T for $Pr_5Ni_2Si_3$ and 4 T for $Pr_{15}Ni_7Si_{10}$. These results provide further confirmation of a second magnetic transition at lower temperature as suggested by the thermal expansion results.

IV. CONCLUSIONS

Theoretical calculations were used to separate the phonon and magnetic contributions to thermal expansion from experimental results on $Pr_5Ni_2Si_3$ and $Pr_{15}Ni_7Si_{10}$. The calculated magnetic contribution to thermal expansion revealed the two magnetic phase transitions for each composition: magnetic order/disorder transition at a higher temperature (41 K for $Pr_5Ni_2Si_3$, 58 K for $Pr_{15}Ni_7Si_{10}$) and spin reorientation transition at a lower temperature (25 K for $Pr_5Ni_2Si_3$, 31 K for $Pr_{15}Ni_7Si_{10}$). These results are consistent with those of magnetostriction measurements and with previously published heat capacity data and magnetic property measurements. In addition, the bulk elastic modulus was determined for each compound from acoustic velocity measurements and the Gruneisen parameter was then determined from thermal expansion, heat capacity, and the bulk elastic modulus for each compound.

ACKNOWLEDGMENTS

This research was supported by the U.S. Department of Energy, Office of Science (OS), Office of Basic Energy Sciences (BES), Materials Sciences Division. Ames Laboratory is operated for the U.S. Department of Energy by Iowa State University under Contract number W-7405-ENG-82. The authors would like to thank V.K. Pecharsky for helpful discussions concerning the results of this research.

[1] P. Rogl, in *Handbook of the Physics and Chemistry of Rare Earths*, edited by K. A. Gschneidner, Jr. and L. R. Eyring (North-Holland, Amsterdam, New York/Oxford, Tokyo, 1987), Vol. 7, p. 1.

[2] A. O. Pecharsky, Y. Mozharivskyj, K. W. Dennis, K. A. Gschneidner, R. W. McCallum, G. J. Miller, and V. K. Pecharsky, Phys. Rev. B **68**, 134452 (2003).

[3] F. Sayetat, P. Fertey, and M. Kessler, J. Appl. Crystallogr. **31**, 121 (1998).

[4] N. W. Ashcroft and N. D. Mermin, *Solid State Physics* (W. B. Saunders Company, Philadelphia, 1976), Chap. 25, p. 493.

[5] D. C. Jiles, S. H. Song, J. E. Snyder, V. K. Pecharsky, T. A. Lograsso, D. Wu, A. O. Pecharsky, Y. Mudryk, K. W. Dennis, and R. W. McCallum (unpublished).

JOURNAL OF APPLIED PHYSICS **99**, 08P304 (2006)

Theoretical calculation of magnetic structure variation in $Pr_5Ni_2Si_3$

S. H. Song,[a] J. E. Snyder, and D. C. Jiles
Materials and Engineering Physics Program, Ames Laboratory, U.S. Department of Energy, and Materials Science and Engineering Department, Iowa State University, Ames, Iowa 50011

(Presented on 2 November 2005; published online 27 April 2006)

The variation of magnetization with temperature of the $Pr_5Ni_2Si_3$ compound was calculated using a nearest neighbor exchange interaction approximation. Pr atoms, which are the only element in this compound with a net magnetic moment, were classified into three types based on the number of nearest neighbor exchange interactions. The expected magnetization versus temperature curve for each type of Pr atom was calculated using the Brillouin function, as well as the average magnetization versus temperature curve for the entire unit cell. The results show that the "corner" atoms exhibit very different behavior from that of the other types of Pr atoms on the "center" or "edge" sites. This is due to the broken symmetry in exchange interaction at the corner site due to interactions with atoms from outside the unit cell that are in closer proximity than atoms within the unit cell. This is considered to be the cause of a second magnetic phase transition observed at a lower temperature than the Curie temperature. © *2006 American Institute of Physics.*

[DOI: 10.1063/1.2173608]

A "model system" in materials science needs to satisfy at least three conditions. (1) The system must be simple enough that there are only a few key dominant factors which influence the physical property to be studied or predicted. (2) The "control variables" that are ultimately responsible for the physical phenomena (such as composition, crystal structure, temperature, pressure, or exchange interaction) should be alterable in a well defined way so that their effects can be studied independently. (3) The general ideas and predictions obtained from the model system should be applicable to other related cases. In this respect, the homologous series of Pr–Ni–Si compounds can serve as a model system for the study of structure/property relationships in magnetic materials.

The ternary Pr–Ni–Si system contains the homologous series of compounds $R_{(n+2)(n+1)}Ni_{n(n-1)+2}Si_{n(n+1)}$, where R is a rare earth element, in this case Pr. It provides a range of materials with different structures as described by Rogl.[1] The compounds $Pr_6Ni_2Si_3(n=2)$, $Pr_5Ni_2Si_3(n=3)$, and $Pr_{15}Ni_7Si_{10}(n=4)$ have been prepared and are known to be the members of this family. These compounds exhibit a hexagonal structure formed of trigonal prismatic columns in which the size of the base plane of the trigonal prismatic "cluster" is determined by the value of n in the chemical formula. As the size of the cluster changes, the number of exchange interactions for each Pr atom systematically changes, thus the physical properties are expected to vary systematically from one member of the series to the next.

Experimental investigations of $Pr_5Ni_2Si_3$ and $Pr_{15}Ni_7Si_{10}$ polycrystalline samples and a $Pr_5Ni_2Si_3$ single crystal sample have recently been reported.[2–5] According to the experimental results, each compound shows two magnetic phase transitions: a magnetic order/disorder transition at a higher temperature (41 K for $Pr_5Ni_2Si_3$ and 58 K for $Pr_{15}Ni_7Si_{10}$) and another transition, which exhibits characteristics of spin reorientation transition, at a lower temperature (25 K for $Pr_5Ni_2Si_3$ and 31 K for $Pr_{15}Ni_7Si_{10}$). The present paper reports on the theoretical investigation of temperature dependent magnetization of single crystal $Pr_5Ni_2Si_3$. The calculations are based on a nearest neighbor exchange interaction approximation. Studies of next nearest neighbor interactions would also be of interest. The inclusion of such additional interactions will require a reduction of the pair exchange energy to maintain the same Curie temperature, and should reduce the sharpness of the Curie point transition compared with the calculation based only on nearest neighbors.

The exchange interaction energy for each atomic site was determined using a nearest neighbor exchange interaction approximation. For this calculation, it was assumed that (1) only the Pr atoms contribute to magnetization and for the purposes of the calculation the magnetic moment per Pr atom was assumed to be $3.58\mu_B$, which is the theoretical value for an isolated Pr atom. In practice the moment on the Pr in condensed matter is smaller, and the Pr atoms on the different lattice sites also have different values of magnetic moment. Therefore for an attempt at such a calculation a fixed magnitude of moment was assumed. (2) The exchange interaction exists only between the nearest neighbors, which is expressed as

$$E_{\mathrm{ex}} = -2J_{\mathrm{NN}}\sum_{i,j} J_i \cdot J_j,$$

where J_{NN} is the exchange interaction constant between nearest neighbors and J_i and J_j are total angular momentum at the ith and jth sites, respectively.

The Pr atoms in the triangular base plane of the structure of $Pr_5Ni_2Si_3$ [Figs. 1(a) and 1(b)] can be classified into three groups by the number of nearest neighbors among Pr atoms: Pr atoms at the center sites, along the edges, and at the corners of the triangular plane have eight, ten, and eleven nearest neighbors, respectively [Fig. 1(b)]. The average exchange

---

[a] Electronic mail: song73@iastate.edu

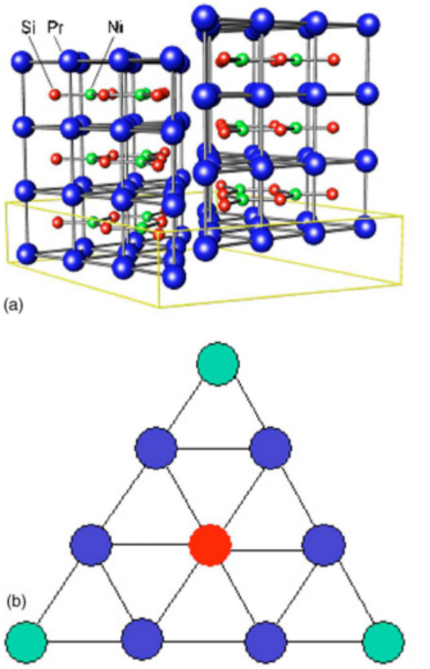

FIG. 1. (a) Crystal structure and unit cell of $Pr_5Ni_2Si_3$ showing the trigonal cells which form prismatic columnar assemblies. [Note that for the purposes of clarity there are additional Ni atoms not shown here which lie at the corner of the rhombohedra containing the two trigonal prisms and amount to one extra Ni atom per trigonal plane (Ref. 5)]. (b) Schematic picture describing three types of Pr atoms in the base plane of pristimatic columnar structure of $Pr_5Ni_2Si_3$ single crystal.

interaction energy between nearest neighbors was calculated based on the experimentally measured Curie temperature (T_c).

Since the effective magnetic field that each atom experiences depends on the number of nearest neighbors for each site, the effective magnetic field for each atomic site is determined from

$$E_{\mathrm{ex}}^{\mathrm{site}} = -J_{\mathrm{NN}} \sum_{i,j}^{\mathrm{site}} J_i \cdot J_j = m \cdot \mu_0 H_{\mathrm{eff}}^{\mathrm{site}} = m \cdot \mu_0 \alpha_{\mathrm{site}} M,$$

where $H_{\mathrm{eff}}^{\mathrm{site}}$ is the molecular field and α_{site} is the molecular field constant for that site.

The total magnetization can be expressed as the sum of the magnetic moments of the three different types of atoms,

$$m^{\mathrm{triangle}} = m^c + m^e + m^a = m_0 B_J\left[\frac{m_0\mu_0(H + H_{\mathrm{eff}}^c)}{k_B T}\right] + 6m_0 B_J\left[\frac{m_0\mu_0(H + H_{\mathrm{eff}}^e)}{k_B T}\right] + 3m_0 B_J\left[\frac{m_0\mu_0(H + H_{\mathrm{eff}}^a)}{k_B T}\right],$$

where B_J is the Brillouin function and m^c, m^e, and m^a are the

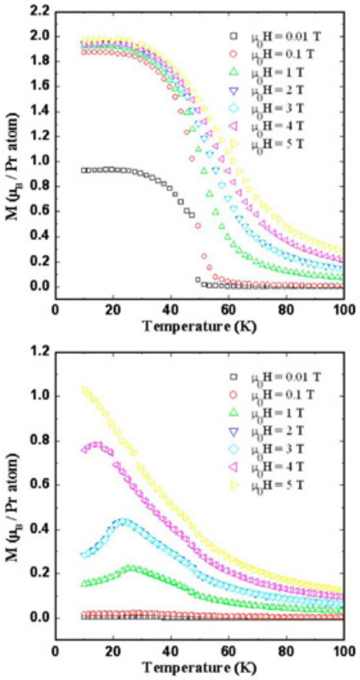

FIG. 2. Variation of the magnetization of $Pr_5Ni_2Si_3$ single crystal with temperature, measured by SQUID (a) parallel and (b) perpendicular to c axis under various magnetic fields (Ref. 6).

magnetization due to each of the Pr atoms at the center, edge, and corner of the triangular plane, respectively.

Figures 2(a) and 2(b) show M vs T curves of $Pr_5Ni_2Si_3$ single crystal, where M was measured parallel (a) and perpendicular (b) to the c axis using a superconducting quantum interference device (SQUID) magnetometer.[6] The SQUID measurements appear to show that the magnetization is not saturated in either direction even at a field of $\mu_0 H = 5$ T but that the easy axis appears tilted much closer to the c axis than to the base plane. This can be explained by considering the atomic arrangement of Pr atoms. For a Pr atom at the corner site, the Pr atom has 11 nearest neighbor Pr atoms, as shown in Fig. 3. This indicates that the sixfold symmetry in exchange interaction is broken by the lack of one Pr atom at one of the six nearest neighbor sites in the same plane. As a result the magnetic moments at the corner Pr atoms will tend to be tilted away from the c axis, as confirmed by the neutron diffraction data[7] which indicate that the magnetic moment of the Pr atom at the corner site is $0.72\mu_B$ along the c axis. Considering that the theoretical magnetic moment of Pr atom is $3.58\mu_B$, the measured magnitude of $0.72\mu_B$ along the c axis can be interpreted as the magnetic moment of the corner atoms is tilted 78° away from the c axis. Based on these results, the angles between the magnetic moments for each site were calculated and these were included in the calculation of the exchange interaction energy,

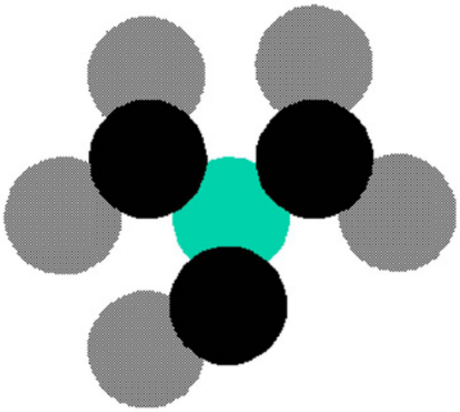

FIG. 3. Atomic arrangement of Pr atoms around the corner site (looking along the *c* axis). The central sphere is a Pr atom at the corner site which has 11 nearest neighbor Pr atoms: 5 in the same base plane, 2 in the same trigonal column and 3 in the second neighbor columns (grey spheres); 3 in neighboring trigonal columns 1/2 plane up (black spheres); and 3 in neighboring trigonal columns 1/2 plane down (not visible behind the black spheres).

$$E_{\mathrm{ex}} = -2J_{\mathrm{NN}}\sum_{i,j} J_i \cdot J_j \cos\theta,$$

where θ is the angle between magnetic moments at *i*th and *j*th sites.

Based on the calculated exchange energy the expected *M* vs *T* curves for each type of Pr atom were calculated. The results are shown in Fig. 4, which shows a consistent Curie temperature for all sites.

The measured $M_{\perp c}$-T curve [Fig. 2(b)] exhibits a local maximum in magnetization at 25 K under an applied magnetic field of 1 T and the transition temperature where the local maximum occurs is lowered as the magnitude of field increases. This behavior is also considered to be due to the asymmetric exchange interactions at the corner sites. The direction of the magnetic component of the corner atom in the base plane should tend to be along the direction of broken symmetry, which is indicated with arrows in Fig. 5, because thermal agitation encounters no competing influence from exchange interaction in this direction, thus making it easy for the magnetic moment to tilt to this direction. Therefore the magnetic components of the corner atoms on the base plane tend to turn to their own locally preferred directions (arrows in Fig. 5). As a consequence, when the temperature decreases below a critical temperature the total magnetic moments on the base plane will be compensated, meaning that the moments of the corner atoms are aligned in such a way that they partially cancel each other out, thus reducing the component of magnetization in the plane.

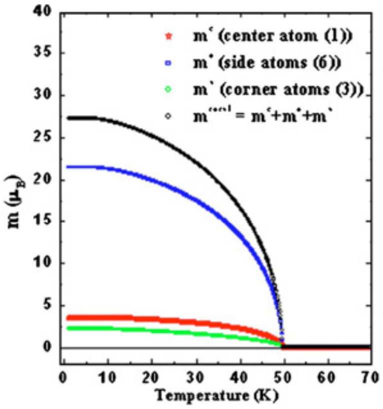

FIG. 4. Simulated *M* vs *T* curves using Brillouin functions for the $Pr_5Ni_2Si_3$ compound. Red, blue, and green symbols represent the magnetization due to the Pr atoms at the center, edge, and corner sites, respectively. The black symbols are the sum of these three contributions, which is the total magnetic moment of the ten Pr atoms in the triangular plane.

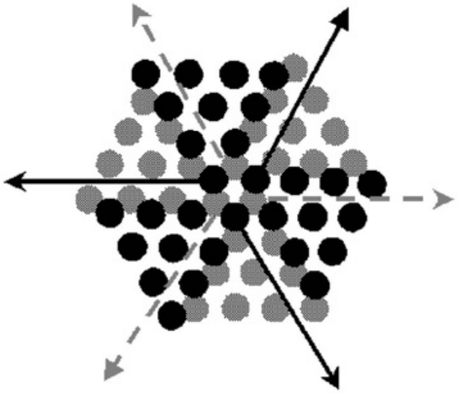

FIG. 5. Atomic arrangement of Pr atoms. Each arrow from the corner atoms indicates the direction in which the symmetry of the exchange interaction at the corner atom is broken.

This research was supported by the U.S. Department of Energy, Office of Science (OS), Office of Basic Energy Sciences (BES), Materials Sciences Division. Ames Laboratory is operated for the U.S. Department of Energy by Iowa State University under Contract No. W-7405-ENG-82. The authors wish to thank Dr. R. W. McCallum for the access to unpublished single crystal $Pr_5Ni_2Si_3$ measurements and for helpful discussions concerning the results of this research.

[1] P. Rogl, in *Handbook of the Physics and Chemistry of Rare Earths*, edited by K. A. Gschneidner, Jr. and L. R. Eyring (North-Holland, Amsterdam, 1987), Vol. 7, p. 1.
[2] A. O. Pecharsky, Y. Mozharivskyj, K. W. Dennis, K. A. Gschneidner, R. W. McCallum, G. J. Miller, and V. K. Pecharsky, Phys. Rev. B **68**, 134452 (2003).
[3] S. H. Song, D. C. Jiles, J. E. Snyder, A. O. Pecharsky, D. Wu, K. W. Dennis, T. A. Lograsso, and R. W. McCallum, J. Appl. Phys. **97**, 10M516-1 (2005).
[4] S. H. Song, J. E. Snyder, D. Wu, T. A. Lograsso, K. W. Dennis, R. W. McCallum, Y. Janssen, and D. C. Jiles, IEEE Trans. Magn. **41**, 3499 (2005).
[5] D. C. Jiles *et al.*, J. Magn. Magn. Mater. **299**, 288 (2006).
[6] R. W. McCallum (private communication).
[7] A. Llobet Megias (private communication).

IEEE TRANSACTIONS ON MAGNETICS, VOL. 41, NO. 10, OCTOBER 2005

Thermal Expansion and Magnetostriction in $Pr_5Ni_2Si_3$ Compounds

S. H. Song[1], J. E. Snyder[1], *Senior Member, IEEE*, D. Wu[2], T. A. Lograsso[2], K. W. Dennis[2], R. W. McCallum[2], Y. Janssen[2], and D. C. Jiles[2], *Fellow, IEEE*

[1]Materials and Engineering Physics Program, Ames Laboratory, U.S. Department of Energy, and
the Material Science and Engineering Department, Iowa State University, Ames, IA 50011, USA
[2]Ames Laboratory, Iowa State University, Ames, IA 50011 USA

The thermal expansion and magnetostriction of polycrystalline and single-crystal $Pr_5Ni_2Si_3$ were investigated over the temperature range 5–300 K. The results show two magnetic phase transitions, one corresponding to the Curie temperature and the other at a lower temperature exhibiting characteristics of a spin reorientation transition. In the temperature range below the Curie temperature, the thermal expansion in single-crystal samples exhibited a temperature dependent anisotropy. Specifically negative and positive magnetic contributions to the thermal expansion were observed along the directions parallel and perpendicular to the c axis respectively.

***Index Terms*—Magnetostriction, rare earth, spin reorientation, single crystal, thermal expansion.**

I. INTRODUCTION

THE TERNARY Pr–Ni–Si system contains an unusual and interesting homologous series $Pr_{(n+2)(n+1)}Ni_{n(n-1)+2}Si_{n(n+1)}$ that has recently been discovered to be magnetic [1]. This alloy system exhibits a hexagonal structure formed of trigonal prismatic columns in which the number of small trigonal prisms that fit along each side of the basal plane of the larger trigonal prism of the unit cell is determined by the value of n in the chemical formula. Therefore, the size of the trigonal prismatic magnetic "cluster" can be controlled by adjustments of chemical composition, providing a model system for systematic investigation of magnetic properties which vary with the size of the cross section of the trigonal columns, with the other structural conditions remaining the same.

This series includes the identifiable compounds $Pr_6Ni_2Si_3$ ($n = 2$), $Pr_5Ni_2Si_3$ ($n = 3$), and $Pr_{15}Ni_7Si_{10}$ ($n = 4$). Investigations of crystal structure, magnetization, specific heat capacity, and magnetocaloric effects of polycrystalline $Pr_5Ni_2Si_3$ have been reported by Pecharsky *et al.* [1]. Thermal expansion investigations of polycrystalline $Pr_5Ni_2Si_3$ and $Pr_{15}Ni_7Si_{10}$ have recently been reported, in which theoretical calculations have been used to extract the magnetic contribution to thermal expansion [2].

This paper reports on an investigation of the properties of both polycrystalline and single-crystal $Pr_5Ni_2Si_3$, in which the magnetic phase transitions were examined by measurements of thermal expansion and magnetostriction. Two magnetic phase transitions have been observed in this compound at 48 K and 25 K. The higher temperature transition is known to be the magnetic order/disorder transition.

Single-crystal samples of $Pr_5Ni_2Si_3$ have recently been produced for the first time. These enabled us to investigate the directional dependence of thermal expansion and magnetostriction. Since the quantity measured for polycrystalline samples is the average value over randomly distributed local anisotropies, investigating single-crystal samples is essential for understanding its anisotropic characteristics.

II. EXPERIMENTAL METHODS

The polycrystalline samples of $Pr_5Ni_{1.9}Si_3$ were prepared by arc melting in an argon atmosphere from high purity components: Pr (99.9+ at. % pure), Ni (99.88 at. % pure), and Si (99.99 at. % pure). The single-crystal samples of $Pr_5Ni_2Si_3$ were synthesized using a vertical gradient freeze method. Thermal expansion and magnetostriction were measured using strain gauges. Measurements were carried out under applied magnetic fields of up to 9 T in the temperature range 5 K–300 K. Thermal expansion and magnetostriction of single-crystal samples were measured in parallel and perpendicular to the c axis under an applied magnetic field along the same direction as the strain was measured.

III. RESULTS AND DISCUSSIONS

A. Polycrystalline Samples

The results of thermal expansion measurements under zero magnetic field and under a field of 9 T ($\mu_0 H = 9$ T) are shown in Fig. 1. Two kinds of anomalies in thermal expansion are observed around 50 K and 25 K, indicating magnetic phase transitions.

To extract the magnetic contribution from the total thermal expansion, the phonon contribution to thermal expansion was calculated using the Debye–Gruneisen theory. This is indicated as a solid line in Fig. 1. This phonon contribution was then subtracted from the measured total thermal expansion. Details of the theoretical calculations have been reported elsewhere [2]. Fig. 2 shows the resultant magnetic contribution to thermal expansion, in which positive strains are observed above the Curie temperature, indicating the magnetovolume effect due to

Digital Object Identifier 10.1109/TMAG.2005.854765

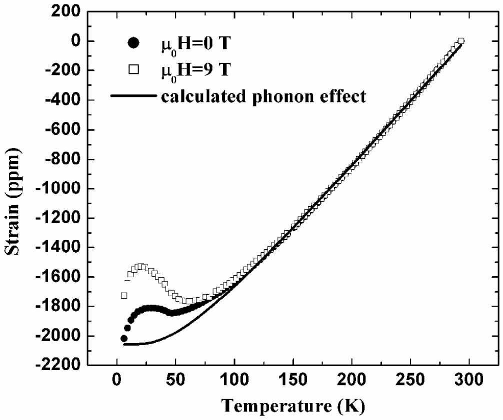

Fig. 1. Temperature-dependent thermal expansion of polycrystalline $Pr_5Ni_2Si_3$ under zero field (solid symbols) and under a field of 9 T (open symbols). Calculated phonon contribution to strain is indicated as a solid line for comparison.

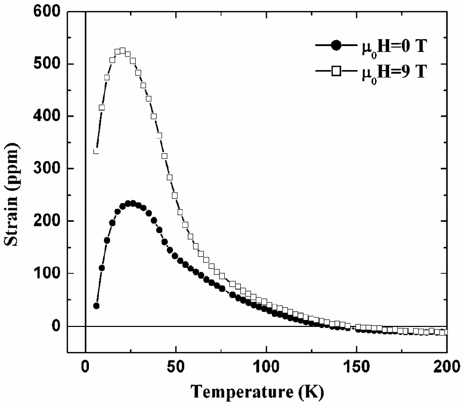

Fig. 2. Magnetic contribution to thermal expansion obtained from the difference between the total thermal expansion and the phonon contribution.

local short range order of magnetic moments which does not disappear immediately at the Curie temperature as long-range order does [3]. The transition temperatures were determined from locations at which distinct changes occur in the slope of the thermal expansion curve. Thus, magnetic transitions were observed at 48 K and 25 K.

B. Single-Crystal Samples

Fig. 3 shows thermal expansion measured in parallel and perpendicular to the c axis under zero magnetic field, with the thermal expansion and calculated phonon contribution for polycrystalline samples shown for comparison. Thermal expansion curves for polycrystalline and single-crystal samples are consistent with each other in the high-temperature region where the magnetic effect is not present. This indicates that the lattice contribution to thermal expansion is isotropic.

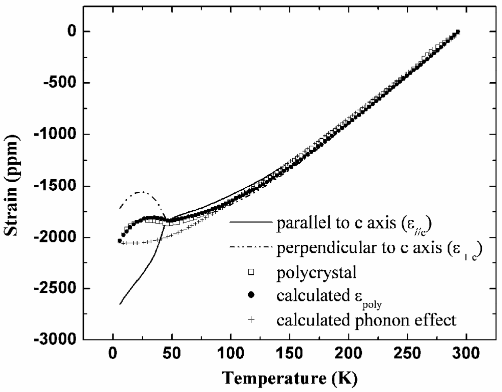

Fig. 3. Variation of thermal expansion of single-crystal $Pr_5Ni_2Si_3$ with temperature measured in parallel and perpendicular to c axis under zero magnetic field. Experimental data of polycrystalline samples are included for comparison with the calculated values for polycrystalline samples using the measured data of single-crystal samples.

The thermal expansion data measured from single-crystal samples were used for calculations of thermal expansion expected for polycrystalline samples by averaging the total local anisotropies over all directions under the assumption that all the grains are randomly distributed inside the polycrystalline samples. Since this compound has a hexagonal structure, the averaged strain in the polycrystal is given by

$$\varepsilon_{\text{poly}} = \frac{1}{3}\varepsilon_{//c} + \frac{2}{3}\varepsilon_{\perp c}$$

where $\varepsilon_{\text{poly}}$ is average thermal expansion for the polycrystalline sample, $\varepsilon_{//c}$ is thermal expansion measured parallel to the c axis, and $\varepsilon_{\perp c}$ is thermal expansion measured perpendicular to the c axis. The results of this calculation have been compared with the experimental results in Fig. 3, which shows excellent agreement between measured and calculated values of strain for a randomly oriented polycrystalline sample.

The single-crystal thermal expansion data below the Curie temperature in Fig. 3 show anisotropy, with different behavior depending on the direction of measurement of strain, whether parallel or perpendicular to the c axis. It seems reasonable to conclude that this anisotropy in thermal expansion is due to the magnetic ordering and that the nonmagnetic phonon contribution remains isotropic below the Curie temperature.

The magnetic contribution to thermal expansion along different directions was calculated from the total thermal expansion in the directions parallel and perpendicular to the c axis by applying the same procedure as described above for the polycrystalline samples. Specifically, the isotropic phonon contribution to thermal expansion was subtracted from the total thermal expansion along different directions. The results of these calculations are shown in Fig. 4, in which the polycrystalline data have been included for comparison. The same value of strain, irrespective of the direction of measurement, was observed at the Curie temperature and above. The magnetic contribution to this thermal expansion in directions parallel and perpendicular to the c axis, which correspond to spontaneous magnetostriction

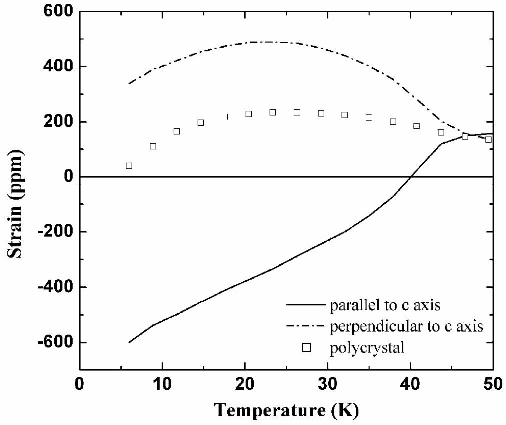

Fig. 4. Variation of the magnetic contribution to thermal expansion of single-crystal $Pr_5Ni_2Si_3$ with temperature measured parallel and perpendicular to c axis under zero magnetic field, which is obtained from the difference between the total thermal expansion and the phonon contribution. Data obtained from polycrystalline samples using the same procedures are included for comparison.

$\lambda_{//c}$ and $\lambda_{\perp c}$, respectively, show different behavior as the temperature decreases below the Curie temperature. $\lambda_{\perp c}$ increases as T decreases from 50 K down to 25 K, then decreases below 25 K, making a local maximum in the graph, while $\lambda_{//c}$ decreases monotonically. In this respect, the second transition at the lower temperature (25 K) is considered to be associated with the variation of the distribution of preferred orientation of magnetic moments along directions perpendicular to the c axis.

IV. CONCLUSION

Two kinds of magnetic phase transitions were observed in $Pr_5Ni_2Si_3$ from the results of thermal expansion and magnetostriction measurements, using both polycrystalline and single-crystal samples. The magnetic order/disorder transition was observed at 48 K and the spin reorientation transition at 25 K.

Anisotropy in thermal expansion was observed from single-crystal samples below the Curie temperature, where the strain perpendicular to the c axis, $\varepsilon_{\perp c}$, increases as the temperature decreases from the Curie point down to 25 K, then decreases below 25 K. On the other hand, the strain parallel to the c axis, $\varepsilon_{//c}$, decreases monotonically as temperature is reduced. Assuming that the phonon contribution to thermal expansion remains isotropic below the Curie point, this feature indicates that this compound shows negative and positive spontaneous magnetostriction in directions parallel and perpendicular to the c axis, respectively (i.e., $\lambda_{//c} < 0, \lambda_{\perp c} > 0$) below the Curie temperature.

Below the second transition temperature (25 K), the thermal expansion behavior perpendicular to the c axis exhibits characteristics of a spin reorientation transition, which is associated with a change in anisotropy energy with temperature.

The expected thermal expansion for polycrystalline samples was calculated from the measured single-crystal data and the results were consistent with the experimental measurements for polycrystalline samples.

From the comparison of the results from polycrystalline and single-crystal samples, it can be seen that the second magnetic transition causes the anomaly in thermal expansion perpendicular to the c axis that was observed below 25 K.

ACKNOWLEDGMENT

This work was supported by the U.S. Department of Energy, Office of Science, Office of Basic Energy Sciences, Materials Sciences Division. Ames Laboratory is operated for the U.S. Department of Energy by Iowa State University under Contract W-7405-ENG-82.

REFERENCES

[1] A. O. Pecharsky, Y. Mozharivskyj, K. W. Dennis, K. A. Gschneidner, R. W. McCallum, G. J. Miller, and V. K. Pecharsky, "Preparation crystal structure, heat capacity, magnetism, and the magnetocaloric effect of $Pr_5Ni_{1.9}Si_3$ and PrNi," *Phys. Rev. B, Condens. Mater.*, vol. 68, p. 134 452, Oct. 2003.

[2] S. H. Song, D. C. Jiles, J. E. Snyder, A. O. Pecharsky, D. Wu, K. W. Dennis, T. A. Lograsso, and R. W. McCallum, "Thermal expansion and Gruneisen parameters in some Pr-Ni-Si compounds," *J. Appl. Phys.*, vol. 97, pp. 1–3, 2005.

[3] R. C. O'Handley, *Modern Magnetic Materials Principles and Applications*. New York: Wiley, 2000, pp. 218–220.

Manuscript received February 7, 2005.

Available online at www.sciencedirect.com

SCIENCE DIRECT®

Journal of Magnetism and Magnetic Materials 299 (2006) 288–299

Journal of magnetism and magnetic materials

www.elsevier.com/locate/jmmm

Thermal expansion and magnetostriction in $Pr_{(n+2)(n+1)}Ni_{n(n-1)+2}Si_{n(n+1)}$ compounds

D.C. Jiles[a,b,*], S.H. Song[a,b], J.E. Snyder[a,b], V.K. Pecharsky[a,b], T.A. Lograsso[a,b], D. Wu[a], A.O. Pecharsky[a], Ya. Mudryk[a], K.W. Dennis[a], R.W. McCallum[a,b]

[a]*Materials and Engineering Physics Program, Ames Laboratory, Iowa State University, Ames, IA 50011, USA*
[b]*Department of Materials Science and Engineering, Iowa State University, Ames, IA 50011, USA*

Received 9 March 2005; received in revised form 18 April 2005
Available online 17 May 2005

Abstract

Thermal expansion and magnetostriction of members of a homologous series of compounds based on the alloy series $Pr_{(n+2)(n+1)}Ni_{n(n-1)+2}Si_{n(n+1)}$ have been measured. The crystal structures of these compounds are closely interrelated because they form trigonal prismatic columns in which the number of trigonal prisms that form the base of the trigonal columns is determined by the value of n in the chemical formula. Two compositions were investigated, $Pr_5Ni_2Si_3$ and $Pr_{15}Ni_7Si_{10}$, corresponding to $n = 3$ and $n = 4$, respectively. The results were analyzed and used to determine the location of magnetic phase transitions by calculating the magnetic contribution to thermal expansion using the Gruneisen–Debye theory. This allowed more precise determination of the magnetic transition temperatures than could be achieved using the total thermal expansion. The results show two phase transitions in each material, one corresponding to the Curie temperature and the other at a lower temperature exhibiting characteristics of a spin reorientation transition.

Keywords: Thermal expansion; Magnetostriction; $Pr_5Ni_2Si_3$ compound; $Pr_{15}Ni_7Si_{10}$ compound

1. Introduction

In the ternary alloy series $Pr_{(n+2)(n+1)}Ni_{n(n-1)+2}Si_{n(n+1)}$ the crystal structure is an assembly of prismatic columns consisting of stacks of trigonal cells. These are particularly interesting because the size of the trigonal cells is a simple function of the chemical composition. In these cases n is the number of small trigonal cells that fits along the side of the prismatic columns, so increasing n increases the width of the prismatic columns. This systematic variation of the crystal structure with composition allows detailed studies to be made of the effects of structure on magnetic

---

[*] Corresponding author. Materials and Engineering Physics Program, Ames Laboratory, Iowa State University, Ames, IA 50011, USA. Tel.: +1 515 294 9685; fax: +1 515 294 8727.

doi:10.1016/j.jmmm.2005.04.015

properties of the compounds. As these compounds have well ordered crystallographic structures, their magnetic properties are, at least in principle calculable, which allows detailed comparison of theory and experiment as the size of the unit cell is varied.

Thermal expansion and magnetostriction measurements have been made of two representative samples of this series $Pr_5Ni_2Si_3$ and $Pr_{15}Ni_7Si_{10}$. The objective was to provide the first definitive measurements of these properties for these materials and to locate the temperatures of any phase transitions from anomalies or discontinuities in the thermal expansion. In this respect, we extracted the magnetic contribution to the thermal expansion from the total thermal expansion by calculating the expected thermal expansion in the absence of any magnetic effects using the Gruneisen Debye theory and then subtracting the calculated from the measured thermal expansion to obtain the magnetic contribution. This gave a clear indication of the location of anomalous features in the strain due to phase transitions and therefore we consider that we have made a more precise determination of the transition temperatures than has been achieved previously, using for example heat capacity or magnetization, because we have been able to isolate the magnetic contributions from the non-magnetic contributions to a measured physical property (in this case the thermal expansion) and located the magnetic anomalies.

The Pr Ni Si alloy system has many different structures in which approximately 20 individual ternary phases have been reported. A summary of the reported ternary intermetallic compounds in the Pr-Ni-Si system has been given by Rogl [1]. Many of these phases exhibit closely related crystal structures. As a result, their physical properties are expected to change systematically from one compound to the next. However, the physical properties of most of the compounds have not been investigated. One exception is $Pr_5Ni_2Si_3$ ($n = 3$) from the series $Pr_{(n+2)(n+1)}Ni_{n(n-1)+2}Si_{n(n+1)}$. The magnetization measurements, heat capacity measurements and calculations of the magnetocaloric effect of this material by Pecharsky et al. [2] showed that the material is paramagnetic for temperatures above 50 K. Upon cooling below this temperature it undergoes an order disorder transition to a ferromagnetic phase. A second magnetic transition was indicated from heat capacity measurements at around 25 K.

The crystal structures of the two compounds $Pr_5Ni_2Si_3$ ($n = 3$), and $Pr_{15}Ni_7Si_{10}$ ($n = 4$) are shown in Fig. 1. In fact, these chemical formulae represent idealized stoichiometries without taking

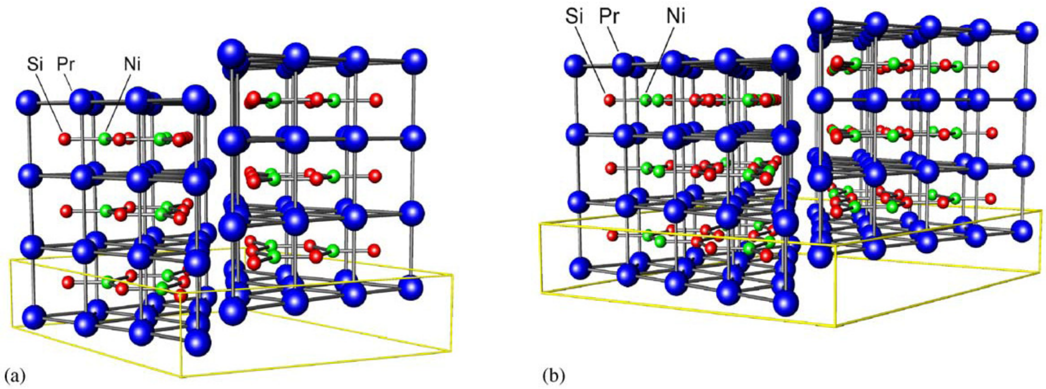

Fig. 1. Crystal structures and unit cells of (a) $Pr_5Ni_2Si_3$ and (b) $Pr_{15}Ni_7Si_{10}$ showing the trigonal cells which form prismatic columnar assemblies. The length of the sides of the prismatic columns is determined by the value of n in the chemical formula for the compound in the series. (Note that for the purposes of simplicity there are additional Ni atoms not shown here. These lie at the corner of the rhombohedra containing the two trigonal prisms and amount to one extra Ni atom per trigonal plane. See, for example, Fig. 4 of Y.M. Prots and W. Jeitschko, Inorg Chem. 37 (1998) 5431.

into account the defects on some of the Ni sites which lead to deviations from the theoretical or ideal stoichiometry [2].

Magnetization and heat capacity measurements, and calculations of the magnetocaloric effect of polycrystalline samples of the $n = 4$ alloy, have recently been completed by Pecharsky et al. [3]. The magnetic behavior of this material is similar to the $n = 3$ compound. The plot of inverse susceptibility χ^{-1} against temperature above T_c gave a straight line that is typical of Curie Weiss-type behavior. The Curie temperature for the compound with $n = 4$ was higher than that of the compound with $n = 3$ by about 10 K. Below T_c there was also evidence of a second spin reorientation transition at a lower temperature in the $n = 4$ compound, which was similar to the behavior observed in the $n = 3$ compound.

2. Experimental methods

2.1. Sample preparation

Polycrystalline samples of $Pr_5Ni_2Si_3$ ($n = 3$) and $Pr_{15}Ni_7Si_{10}$ ($n = 4$) were prepared by arc melting in an argon atmosphere from high-purity components; Praseodymium (99.9+ at%) was prepared by the Materials Preparation Center at Ames Laboratory. Nickel (99.88 at% pure) and Silicon (99.999 at%) were purchased from commercial vendors. Selected samples were drop cast after arc melting.

The samples were heat treated at different temperatures for different periods of time ranging from 5 days to 4 weeks. One sample was conventionally arc-melted and then annealed at 870 K for 5 days. The other sample was arc-melted and drop cast followed by an annealing schedule that consisted of 1120 K for 2 weeks and then 1170 K for 2 weeks. Comparison of the microstructures of these two samples showed significant differences. The first sample contained large grains which were needle shaped and appeared in colonies This raises the possibility of significant crystallographic texture on the sample face under the strain gauge. The needle-shaped grains probably resulted from the temperature gradients present in the arc-melted button during solidification. In the second sample, not only was the solidification rate higher but also the temperature gradients were smaller and more symmetric about the cylindrical axis. The result was a finer, equiaxed grain structure. Although the low-temperature anneal did not modify the grain morphology of the arc-melted sample some refining of the microstructure of the drop cast sample took place during the high-temperature anneal.

Chemical compositions of the samples were determined using X-ray diffraction (XRD) and energy dispersive spectroscopy (EDS). Phase identifications of these samples were performed by X-ray powder analysis using Scintag powder diffractometer. The Rigaku TTRAX powder diffractometer was used for analyzing temperature-dependent lattice parameters in the temperature range from 5 to 294 K. The actual chemical composition of the $n = 3$ compound was found to be $Pr_5Ni_{1.9}Si_3$, while the $n = 4$ compound was found to be $Pr_{15}Ni_{6.7}Si_{10}$. Although the compounds did not form at the exact stochiometric compositions, they will nevertheless be identified hereafter in this paper by the nominal stochiometric compositions $Pr_5Ni_2Si_3$ and $Pr_{15}Ni_7Si_{10}$. X-ray powder diffraction analysis of the heat treated materials indicated that, within the sensitivity of the technique, they were single-phase alloys.

2.2. Property measurements

Thermal expansion and magnetostriction were measured using Micro Measurements low-temperature strain gauges type WK-06-031CF-350. These were bonded on to the specimens using M Bond 610 low-temperature strain gauge adhesive . Measurements were carried out under applied magnetic fields of up to $H = 7.2 \times 10^6$ A/m ($\mu_0 H = 9$ T) in the temperature range 5 300 K. A "half bridge" configuration was used to compensate for the temperature and field dependence of the strain gauge resistance not caused directly by strain in the sample. The second "dummy" gauge was attached to a copper reference sample, the measured strain being therefore the difference in thermal expansion between the sample and that of copper. The temperature dependence of the unit cell dimensions and thus the anisotropy in the thermal expansion was measured over the temperature range 5 310 K using in situ X-ray powder diffraction. Magnetization was measured using a Quantum Design magnetometer under applied magnetic fields ranging from 0 to 5 T.

3. Results

3.1. Thermal expansion

The thermal expansion results for one sample of $Pr_5Ni_2Si_3$ are shown in Fig. 2. These reveal an anomaly in thermal expansion at about 50 K which, in combination with results reported previously [2], is indicative of a magnetic phase transition from a high-temperature disordered paramagnetic structure to a low-temperature ordered magnetic structure.

Thermal expansion results under fields of $H = 0$ and 7.2×10^6 A/m ($\mu_0 H = 0$ and 9 T) are compared in Fig. 2. The minimum in strain in the vicinity of 50 K is indicative of the Curie temperature. The strain then reduced in amplitude until about 25 K when the material underwent a second transition below which temperature the strain amplitude began to increase again as the temperature was further reduced. The application of a magnetic field widens the temperature range between these transitions as shown in Fig. 2.

The difference between the thermal expansion curves under zero field and under a field of $\mu_o H =$ 9 T can be attributed to magnetic contributions to strain. Assuming that these features are largely due to magnetic contributions to the thermal expansion, it indicates the presence of one or more magnetically ordered phases at lower temperatures.

The derivative of strain λ with respect to temperature is shown in Fig. 3. This shows that the changes in sign of $d\lambda/dT$ occur at 29 and 48 K under zero magnetic field, and at 20 and 61 K under a magnetic field of $\mu_0 H = 9$ T. These results suggest that the magnetic phase which exists in this intermediate temperature range between these transition temperature, is stabilized by the presence of an applied magnetic field.

The thermal expansion of $Pr_{15}Ni_7Si_{10}$ and its derivative with respect to temperature are also

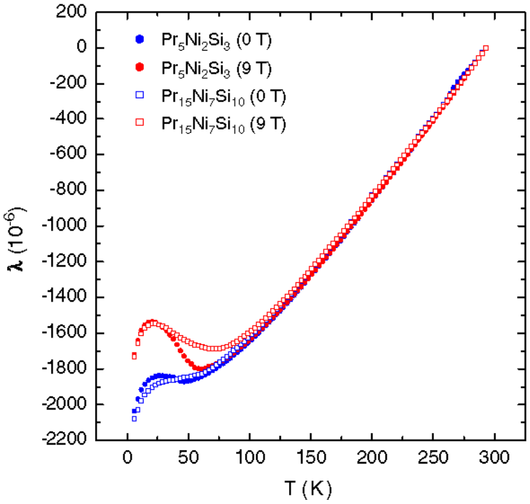

Fig. 2. Thermal expansion results for $Pr_5Ni_2Si_3$ (which was annealed at 1120 K for 2 weeks and then 1170 K for 2 weeks) and $Pr_{15}Ni_7Si_{10}$ under zero applied magnetic field and under a field of $H = 7.2 \times 10^6$ A/m ($\mu_0 H = 9$ T).

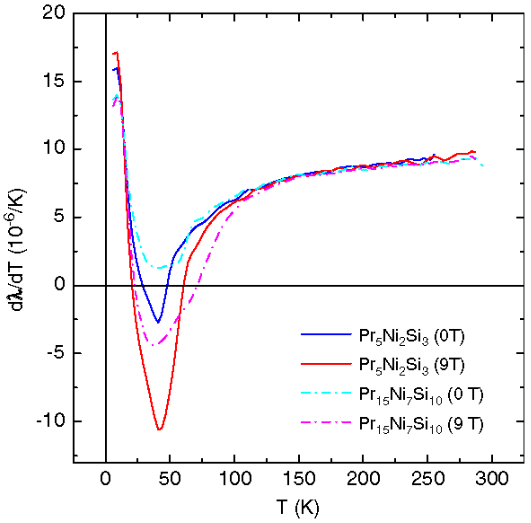

Fig. 3. Derivatives of the strain with respect to temperature $d\lambda/dT$ for $Pr_5Ni_2Si_3$ and $Pr_{15}Ni_7Si_{10}$ under zero applied magnetic field and under a field of $H = 7.2 \times 10^6$ A/m ($\mu_0 H = 9$ T).

shown in Figs. 2 and 3. The results under zero applied field reveal an anomaly in thermal expansion below 60 K, which is similar to the behavior of $Pr_5Ni_2Si_3$ with the exception that it occurs at a slightly higher temperature. It can be seen that the presence of the magnetic field broadens the anomaly in thermal expansion below about 80 K, in particular the difference in thermally induced strain at these temperatures compared with room temperature was smaller when under the action of an applied field than under zero field. This suggests that the difference between these curves is due to changes in the magnetic order, and as in the $Pr_5Ni_2Si_3$ alloy this indicates the presence of one or more magnetically ordered phases at lower temperatures.

A comparison of the thermal expansion data for two different samples of the $Pr_5Ni_2Si_3$ alloy are shown in Fig. 4. The two samples exhibited significant differences in their behavior, which are attributed to the different microstructures resulting from differences in sample preparation, as described in Section 2.1.

3.2. Determination of lattice and magnetic contributions to thermal expansion

To identify the location of magnetic phase transitions from the measured data, the lattice (phonon) contributions to the thermal expansion were calculated from the heat capacity data using the Gruneisen Debye model [6]. The resulting thermal expansion from this calculation was then subtracted from the total thermal expansion to leave the magnetic contribution to the thermal expansion. In order to make such calculations, the Debye temperature was first calculated from the heat capacity data shown in Fig. 5. In normal (non magnetic) metals the Debye temperature θ_D is usually calculated from the low temperature equation [7]

$$C_v \; \frac{12\pi^4}{5} N_o k_B \left(\frac{T}{\theta_D}\right)^3 + AT,$$

where C_v is the specific heat capacity at constant volume, N_o is Avogadro's number, k_B is Boltzmann's constant, T is the thermodynamic temperature and A is an empirically determined coefficient that relates the electronic contribution to heat capacity. The term depending on T^3 is the lattice contribution and the term that is linear in T is the electronic contribution. This equation is valid in the range $T < 0.1\theta_D$. However in the case of $Pr_5Ni_2Si_3$ the magnetic contributions to the heat capacity, which arise in the low-temperature regime where this equation is usually applied, preclude the use of this equation for accurately

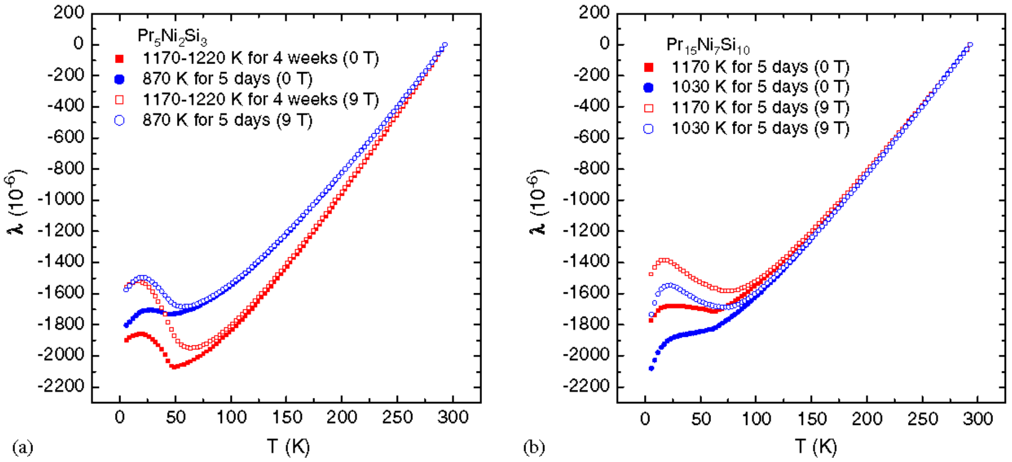

Fig. 4. Thermal expansion under zero field and under a field of $H = 7.2 \times 10^6$ A/m ($\mu_0 H = 9$ T) for (a) $Pr_5Ni_2Si_3$ and (b) $Pr_{15}Ni_7Si_{10}$, which had been given different heat treatments, as described in the text.

determining θ_D. Therefore an alternative procedure was developed.

The magnetic effects are negligible at temperatures well above the ordering temperature, which in $Pr_5Ni_2Si_3$ is in the vicinity of 50 K. Therefore, the heat capacity of the material should obey the Debye model at temperatures higher than this. An extrapolation procedure was developed to determine the locus of values of $C_v(T)$ which will give a limiting value of $C_v = 3N_0k_B$ as T tends to infinity. This extrapolation was achieved by plotting C_v against $1/T$ and determining the intercept at $1/T = 0$ as shown in Fig. 5 using an approximate equation for the Debye function at high temperatures. The entire heat capacity curve was normalized to ensure that the data extrapolated to the correct value of the high-temperature asymptote of the heat capacity. The value of θ_D was obtained by finding the temperature at which $C_v(\theta_D) = 0.952C_v(\infty)$ [4].

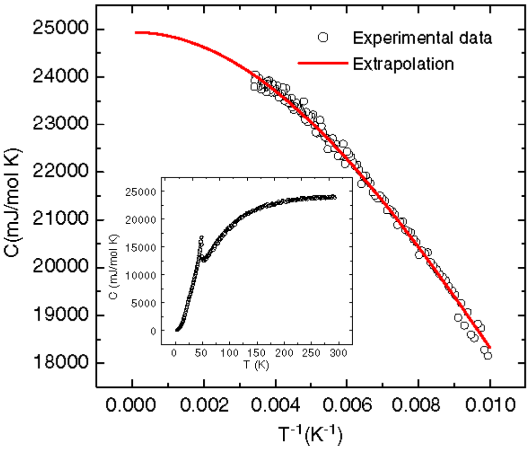

Fig. 5. Heat capacity plotted against $1/T$, with extrapolation of data to $1/T = 0$. This allows the high-temperature asymptote of C_v (at $T = \infty$) to be determined. The heat capacity data as shown in the figure were normalized to this limiting value (Inset: Variation of the heat capacity of $Pr_5Ni_2Si_3$ with temperature. In the low-temperature regime the λ-type anomaly around 50 K and the weaker feature around 25 K show evidence of magnetic phase transitions [2]).

Once θ_D was obtained the expected lattice contribution to the thermal expansion was calculated theoretically from the heat capacity data at different temperatures using the method of Sayetat et al. [5]. It is possible to perform this calculation without knowing θ_D, however θ_D then becomes a variable that is calculated as part of the procedure, and consequently there is a likelihood of greater error in the results. This method does not account for magnetic contributions to thermal expansion and so the calculations were performed over the temperature range 100 300 K which were sufficiently far from any magnetically ordered phases that magnetic contributions could be ignored. This calculation gives a slowly varying background contribution to thermal expansion that would be expected in the absence of magnetic contributions.

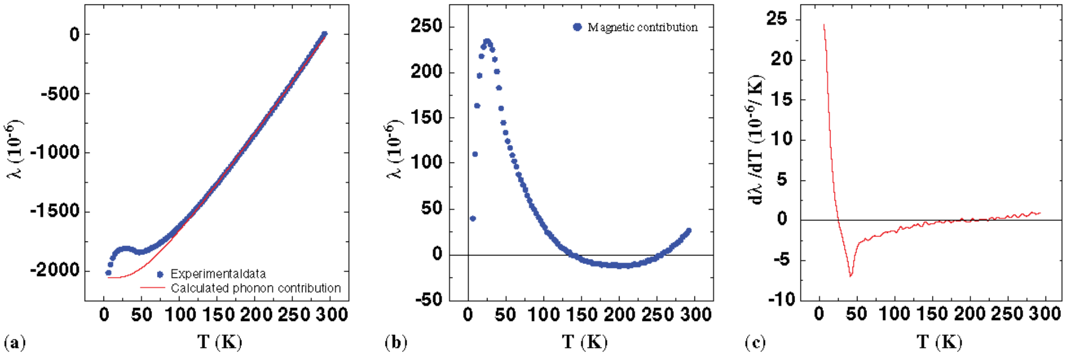

(a) (b) (c)

Fig. 6. (a) Comparison of experimental results on $Pr_5Ni_2Si_3$ in zero field with expected thermal expansion as calculated from the heat capacity data using the Gruneisen–Debye model and the equations of Sayetat et al. [5]. The calculated Debye temperature was 201 K. (b) The magnetic contribution to thermal expansion obtained from the difference between the total thermal expansion and the phonon contribution. (c) Derivative of the magnetic contribution to thermal expansion with respect to temperature.

The results were then extended to lower temperatures using the same equation to determine the expected thermal expansion in the absence of magnetic effects. This is shown in Fig. 6(a) together with the experimental data. The differences between the two curves are attributed to magnetic contributions to thermal expansion.

The phonon contribution has been subtracted from the measured thermal expansion as shown in Fig. 6(b). Since the other electronic contributions to thermal expansion are negligible in comparison with the magnetostrictive component, the resultant is the magnetic contribution to the thermal expansion. The derivative with respect to temperature of this resultant magnetic contribution to the thermal expansion is shown in Fig. 6(c). This derivative will be strongly dependent on any changes in the magnetic structure and it can be seen that magnetic transitions are indicated where distinct changes occurred in the slope of the curve of the magnetic component of thermal expansion against temperature.

Applying the same procedure as described above for $Pr_5Ni_2Si_3$ the phonon contribution to the thermal expansion of $Pr_{15}Ni_7Si_{10}$ was calculated and then subtracted from the total thermal expansion to give the magnetic contribution. The results are shown in Fig. 7. From this, the magnetic transition temperatures were found to occur at 58 and 31 K.

Analysis of the features in the magnetic contribution to thermal expansion indicates the existence of magnetic transitions at temperatures of 48 and 27 K in $Pr_5Ni_2Si_3$ and 59 and 33 K in $Pr_{15}Ni_7Si_{10}$ corresponding to the order/disorder and spin reorientation transitions, respectively.

A summary of the transition temperatures and other features in these two materials is shown in Table 1.

3.3. Comparison with X-ray diffraction results

The temperature dependences of the linear and volume strains obtained from X-ray diffraction are shown in Fig. 8. The anomaly that was observed in the thermal expansion below 50 K in Fig. 2 correlates with a similar feature observed in the lattice parameters and hence also in the calculated volume thermal expansion observed in the XRD analysis.

3.4. Magnetostriction

The magnetostriction of $Pr_5Ni_2Si_3$ is shown in Fig. 9(a). Magnetostriction was measured at temperature intervals of ten degrees from 10 to 70 K under an applied magnetic field up to $\mu_0 H = 9$ T. The results show a positive magnetostriction at all temperatures. This is consistent with the results of calculations of thermal expansion in

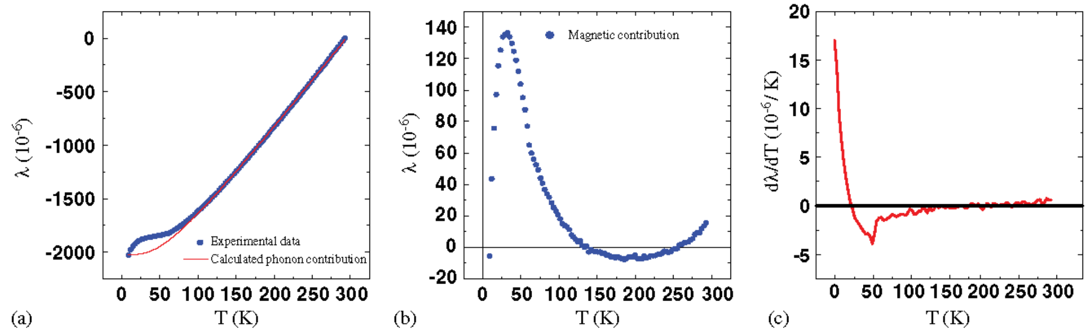

Fig. 7. (a) Comparison of the thermal expansion of $Pr_{15}Ni_7Si_{10}$ in zero field with the calculated phonon contribution to thermal expansion. The calculated Debye temperature was 209 K. (b) The magnetic contribution to thermal expansion obtained from the difference between the total thermal expansion and the phonon contribution. (c) The derivative of the magnetic contribution to thermal expansion.

Table 1
Phase transition temperatures and temperatures of other features obtained from thermal expansion, magnetization and magnetostriction data

Magnetic property	$Pr_5Ni_2Si_3$	$Pr_{15}Ni_7Si_{10}$
Upper magnetic transition temperature[a] (Curie point–order/disorder transition) (K)	48±2	59±2
Lower magnetic transition temperature[a] (Spin reorientation transition) (K)	27±2	33±2
Inflection point[b] at 10 K (from magnetization curve) (T)	3.0	3.9
Inflection point[b] at 10 K (from magnetostriction curve) (T)	3.0	3.8

[a] Magnetic transition temperatures determined from thermal expansion curves with background phonon contributions subtracted.
[b] Inflection points determined from first derivatives with respect to magnetic field of magnetization and magnetostriction curves.

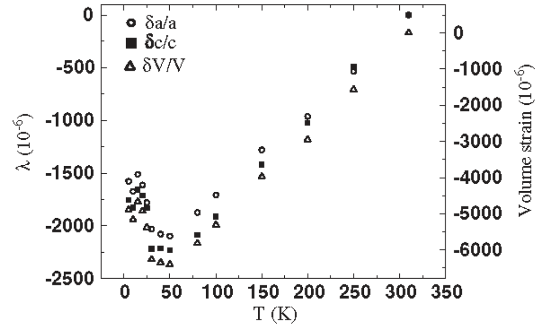

Fig. 8. Linear and volume thermal expansion of lattice strains $\delta a/a$, $\delta c/c$ and $\delta v/v$ calculated from X-ray diffraction data.

Fig. 6, which showed a positive contribution to strain from the magnetic ordering.

The magnetostriction amplitude under a $\mu_0 H = 9\,T$ field decreased from 360×10^{-6} at 10 K to 130×10^{-6} at 50 K, but note that even in the paramagnetic regime a field-induced strain of 30×10^{-6} was observed at $\mu_0 H = 9\,T$ which is higher than the magnetostriction observed in many ferromagnetic materials. This suggests, but does not necessarily by itself prove, a large stress-dependent anisotropy in the paramagnetic phase. An inflection point on the $\lambda-H$ curve, meaning a maximum in $d\lambda/dH$, was observed around $H = 2.4 \times 10^6\,A/m$ ($\mu_0 H = 3\,T$) at lower temperatures (10 and 20 K) but was not seen at 30 K and higher temperatures. This feature may be related to behavior seen in the magnetization data as discussed below.

The magnetostriction of $Pr_{15}Ni_7Si_{10}$ is shown in Fig. 9(b). Magnetostriction was measured at constant temperature at intervals of ten degrees from 10 to 70 K under an applied magnetic field of up to $\mu_0 H = 9\,T$. The results show similar behavior to $Pr_5Ni_2Si_3$ in which the amplitude of magnetostriction was always positive but decreased with increasing temperature. An inflection point on $\lambda-H$ curve, meaning a maximum in $d\lambda/dH$, was observed around $H = 3.0 \times 10^6\,A/m$ ($\mu_0 H = 3.8\,T$) at low temperatures (10 and 20 K), which was not seen at higher temperatures.

3.5. Magnetization

The magnetization curves of $Pr_5Ni_2Si_3$ are shown in Fig. 10. These have been calculated in terms of the net number of Bohr magnetons per Pr atom. The magnetic moment per Pr atom in a solid such as $Pr_5Ni_2Si_3$ was expected to be 3.2 Bohr magnetons, which corresponds to a bulk magnetization of $M = 0.635 \times 10^6\,A/m$ if all Pr moments are aligned parallel. The fact that the value of magnetization at a field $H = 4.0 \times 10^6\,A/m$ ($\mu_0 H = 5\,T$) is only 50% of this value is due to the Pr atoms on some of the lattice sites having a reduced magnetic moment because not all Pr sites are equivalent, as can be seen from Fig. 1. In fact there are three types of Pr sites: those in the corners of the triangular planes with two nearest neighbors in the plane, those along the edges with four nearest neighbors in the plane and those at the center with six nearest neighbors in the plane.

The inflection point that was observed around $H = 2.4 \times 10^6\,A/m$ ($\mu_0 H = 3\,T$) in M H curves below 25 K may be compared to the existence of an inflection point in the magnetostriction curve (peak in $d\lambda/dH$) in Fig. 10 at lower temperatures (10 and 20 K), which is not present at higher

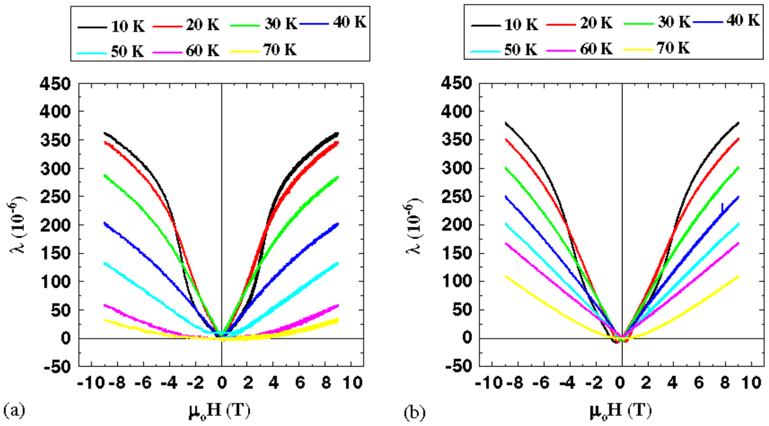

Fig. 9. Magnetostriction of (a) $Pr_5Ni_2Si_3$ and (b) $Pr_{15}Ni_7Si_{10}$ in fields of up to $H = 7.2 \times 10^6$ A/m ($\mu_0 H = 9$ T) at different temperatures over the range 10–70 K.

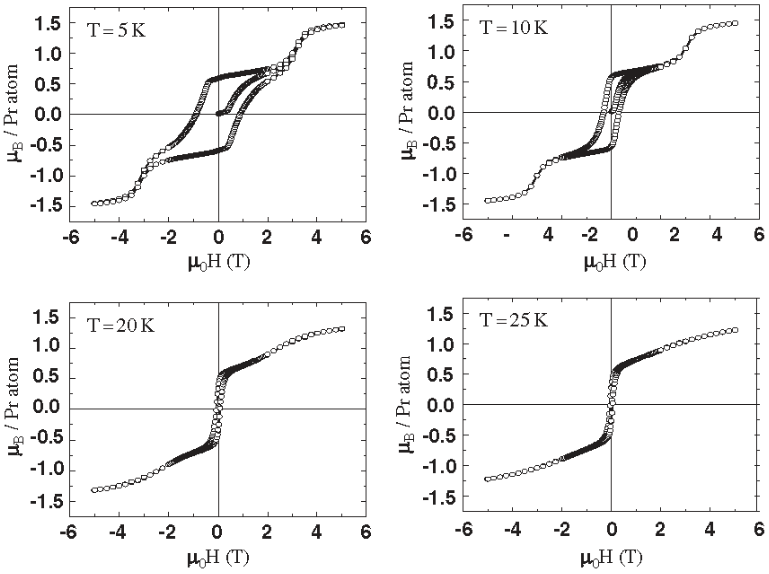

Fig. 10. Variation of magnetization of $Pr_5Ni_2Si_3$ (calculated as the number of Bohr magnetons per Pr atom) with magnetic field at different temperatures over the range 5–25 K.

temperatures. This seems to provide supporting evidence for the existence of an additional magnetic transition in the vicinity of 25 K.

Magnetization versus field curves are shown in Fig. 11 for $Pr_{15}Ni_7Si_{10}$ at various temperatures. As in the case of the $Pr_5Ni_2Si_3$ results in Fig. 10, the net magnetic moment per Pr atom is much lower than would be expected if the moments were aligned parallel. The reasons for this are the same as discussed above for $Pr_5Ni_2Si_3$. These data show

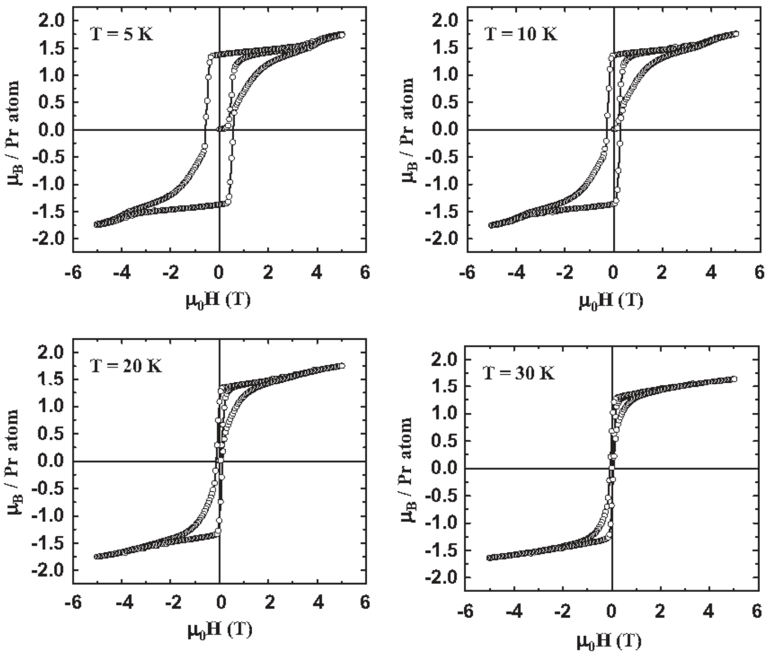

Fig. 11. Variation of magnetization of $Pr_{15}Ni_7Si_{10}$ (calculated as the number of Bohr magnetons per Pr atom) with magnetic field at different temperatures over the range 5–30 K.

a decrease in coercivity H_c with increasing temperature. The minimum in magnetostriction showed similar behavior with increasing temperature, although it should be noted that the field value at which this minimum occurs does not necessarily correspond to the coercivity.

3.6. *Comparison of magnetization and magnetostriction curves*

The magnetization data have been compared with magnetostriction curves measured at the same temperatures as shown in Fig. 12. The "reversible magnetization" plotted in this figure is an artificial construct, obtained by extrapolating to $H = 0$ the linear, high field region of the magnetization curve as the field is reduced from its maximum. This intercept gives the remanent magnetization that would be expected if all the magnetization processes occurring as the field is removed were reversible. The resulting magnetization curve at 10 K suggests a possible spin reorientation transition at a field of $H = 2.4 \times 10^6$ A/m ($\mu_0 H = 3$ T), which is not apparent at temperatures of 25 K and above.

4. Conclusions

The compounds with composition $Pr_5Ni_2Si_3$ and $Pr_{15}Ni_7Si_{10}$ are members of a homologous series in which each member of the series has the form $R_{(n+2)(n+1)}Ni_{n(n-1)+2}\,Si_{n(n+1)}$, where R is a rare earth element and n ranges from 2 to 4. Magnetic properties of these two members of the series have been measured. For both compounds there is evidence in thermal expansion, magnetostriction and magnetization data for two magnetic transitions. The temperature of these transitions was found to depend on the size of the trigonal prismatic columns. The exchange coupling increased, and hence the Curie temperature

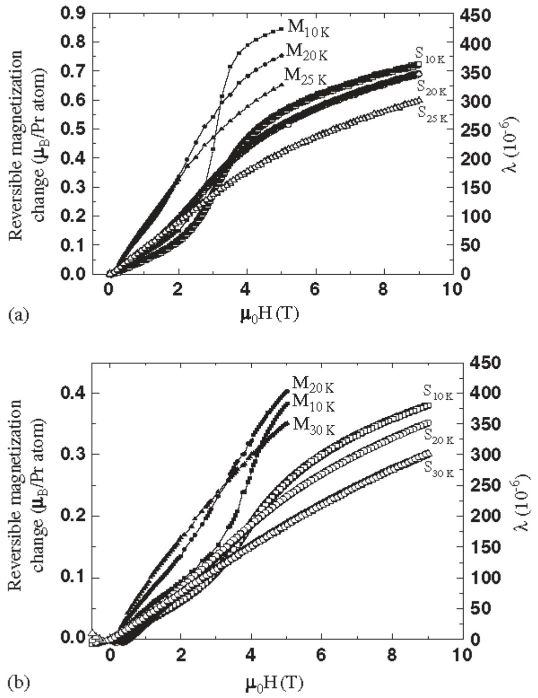

Fig. 12. Comparison of the variations of magnetostriction λ for (a) $Pr_5Ni_2Si_3$ and (b) $Pr_{15}Ni_7Si_{10}$ with magnetic field at constant temperatures with the extrapolated intercept on the M-axis of the linear region of the recoil magnetization. This is the value of magnetization that would be expected at $H = 0$ if all the magnetization processes occurring as the field is removed were reversible.

increased, with more atoms within the prismatic cells. Therefore, we expect T_c to increase with n in this series of compounds. In both cases, the higher temperature transition was the order disorder transition at the Curie point. The lower-temperature transition is believed to be due to a spin reorientation transition, which lowers the net magnetic moment per unit cell as the temperature is reduced.

It is interesting to note that both compounds exhibit significant magnetostriction in the paramagnetic state indicative of a large anisotropy in the susceptibility of that state. Both the magnetization versus field and magnetostriction versus field curves indicate that at low temperature there is a field-induced magnetic transition. As may be expected, the magnetostriction is determined largely by the extent of the reversible rotation away from the easy magnetization axis. Neither the magnetization nor the magnetostriction appeared to approach saturation in fields of $H = 4.0 \times 10^6$ and 7.2×10^6 A/m ($\mu_0 H = 5$ T and 9 T), respectively.

A calculation based on both the high-temperature specific heat and thermal expansion data yielded Debye temperatures of 201 and 209 K for $Pr_5Ni_2Si_3$ and $Pr_{15}Ni_7Si_{10}$ compounds, respectively. These values are considerably higher than those obtained by a simple evaluation of the low-temperature behavior of the specific heat in terms of the Debye model which does not adequately account for the magnetic contributions to the specific heat. The treatment of the high-temperature data allows the determination of the lattice (phonon) contribution to the thermal expansion so that the magnetic contribution can be determined from the difference between the total thermal expansion and the value expected solely on the basis of lattice contributions. For $Pr_5Ni_2Si_3$ the thermal expansion measurements have been validated using low-temperature X-ray diffraction. From these data phase transition temperatures have been identified at 48 and 27 K in $Pr_5Ni_2Si_3$ and 59 and 33 K in $Pr_{15}Ni_7Si_{10}$.

Acknowledgments

This work was supported by the US Department of Energy, Office of Basic Energy Science, Materials Science Division. The research was performed at Ames Laboratory. Ames Laboratory is operated for the US Department of Energy by Iowa State University under Contract no. W-7405-ENG-82.

References

[1] P. Rogl, in: K.A. Gschneidner Jr., L.R. Eyring (Eds.), Handbook on the Physics and Chemistry of Rare Earths, vol. 7, North-Holland Physics Publishing, Amsterdam, New York, Oxford, Tokyo, 1987, p. 1.

[2] A.O. Pecharsky, Y. Mozharivskyj, K.W. Dennis, K.A. Gschneidner, R.W. McCallum, G.J. Miller, V.K. Pecharsky, Phys. Rev B 68 (2003) 134452.
[3] A.O. Pecharsky et al., Unpublished data.
[4] N.W. Ashcroft, N.D. Mermin, Solid State Physics, W.B. Saunders Company and Holt Rinehart and Winston, New York, 1976, p. 461.
[5] F. Sayetat, P. Fertey, M. Kessler, J. Appl. Crystallogr. 31 (1998) 121.
[6] D.C. Jiles, Introduction to the Electronic Properties of Materials, Second Ed, Nelson Thornes, Cheltenham, 2004, p. 33.
[7] N.W. Ashcroft, N.D. Mermin, Solid State Physics, Holt Rinehart and Winston, New York, 1976, pp. 458–464.

IEEE TRANSACTIONS ON MAGNETICS, VOL. 41, NO. 7, JULY 2005

Magnetooptic Sensor for Remote Evaluation of Surfaces

S. J. Lee[1], S. H. Song[1], D. C. Jiles[1], *Fellow, IEEE*, and H. Hauser[2]

[1]Center for Nondestructive Evaluation, Iowa State University, Ames, IA 50011 USA
[2]Institute for Industrial Electronics and Materials Science, Vienna University of Technology, A-1040 Vienna, Austria

A new magnetooptic (MO) detection method utilizing changes in the optical path through a transparent MO thin film has been developed and studied for evaluation of surface deformation created by subsurface or internal defects in materials. Investigation of defects cannot be performed on nonconducting and nonmagnetic materials using conventional electromagnetic techniques such as eddy-current or magnetic flux leakage. The new method utilizes the controlled periodic displacement of a domain wall in the MO thin film and can be used to measure remotely mechanical deformation of a surface of any type of material by measuring the changes of width of the shoulder in the intensity versus time waveform.

***Index Terms*—Faraday rotation, magnetooptic Kerr effect, remote sensor, surface deformation.**

I. INTRODUCTION

SURFACE deformation caused by subsurface and internal defects can cause failure in structural components. When the magnitude of surface deformation is of the order of micrometers, it is difficult to find a suitably sensitive nondestructive evaluation technique for remote detection of such deformation. This is particularly problematic when the mechanical components under evaluation are made of nonmagnetic or nonconducting materials, because existing evaluation techniques such as magnetic particle inspection, magnetic flux leakage, and eddy-current techniques, which rely on the magnetic or electrical conducting properties of the test sample, are not suitable [1]–[4].

In the standard magnetooptic imaging (MOI) technique [5], [6], a magnetooptic (MO) film is placed in close proximity to the surface of a test sample having a surface defect. Magnetic leakage fields from a surface defect cause rearrangement of domain structure in the MO film giving rise to contrast in the domain images of the MO film which are indicative of defects in the sample.

In this paper, we report a new MO nondestructive evaluation method based on the ac modulated Faraday effect for detecting surface deformation created by subsurface or internal defects. This magnetooptic technique provides a remote method for investigation of material surfaces. The magnetooptic sensor system consists of a He–Ne laser, a MO garnet film, an ac excitation coil, two permanent magnets, an analyzer, and a photodetector. The deformed surfaces can be detected by monitoring the changes of the signal from those of an undeformed surface. The new technique was found to provide sufficient sensitivity for detection of small amounts of deformation that amounted to a rotation of 0.01° of the surface. Remote evaluation of microscopic surface deformation is possible because this technique does not require close contact between the sample surface and the magnetooptic sensor film. The new technique can be used to evaluate surface deformation in materials. The limitation of the technique is that the specimen under investigation should be sufficiently reflective for the reflected light beam intensity to be detected at the photodetector.

Domain-wall motion in a transparent MO film has been utilized before for development of a variety of sensors: A magnetooptic sensor measuring the light beam positions by means of the magnetooptical spatial light modulation in a plate of yttrium orthoferrite [7], a magnetooptical current sensor measuring optical current based on the direct registration of the domain-wall motion under action of the magnetic field of the measured current [8], a magnetooptic switch based on domain-wall motion in yttrium orthoferrite crystals [9], a mechanical sensor based on the domain-wall nucleation process [10], and a magnetooptical rotational speed sensor measuring angular velocities using the domain-wall motion in the orthoferrite plate [11]. A detailed description of domain-wall motion in these cases has been given by Didosyan *et al.* [12].

II. MODULATION OF FARADAY ROTATION

The new technique depends on a new use of the magnetooptic Faraday effect which occurs when a linearly plane polarized light beam interacts with a transparent magnetic material, such as a garnet [13], [14]. The magnitude of the Faraday rotation is dependent on the magnetooptic properties of the MO material, the magnetization in the material, and the path length of the light through the MO material. In the polar geometrical configuration, where directions of the applied magnetic field B and incident linearly plane polarized light beam are perpendicular to the surface of the film, the magnitude of Faraday rotation is given by $\Phi_F = V\ell B$, where V is the Verdet coefficient of the film, ℓ is the thickness of the film, and B is the magnetic flux density in the film. The magnetooptic film has a magnetic anisotropy with its easy axis of magnetization normal to the film surface. Therefore, a small magnetic field perpendicular to the surface of the film causes rearrangement of domain structures in the film.

A stable two-domain structure in the MO film with a single domain wall (DW) is generated by two permanent magnets with opposite polarities that are placed near the MO film [7] as shown in Fig. 1. The two permanent magnets produce a magnetic field

---

Digital Object Identifier 10.1109/TMAG.2005.851858

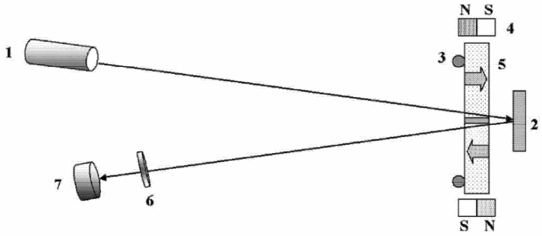

Fig. 1. Schematic of the new remote magnetooptic sensor for evaluation of surface deformation: (1) He–Ne laser, (2) sample, (3) ac excitation coil, (4) permanent magnets, (5) MO sensor film, (6) analyzer, and (7) photodetector.

$H_{\rm PM}$ with a uniform field gradient between the magnets. When there is no applied ac magnetic field, the equilibrium position of the DW is at the center of the film halfway between the two permanent magnets. An ac magnetic field is applied perpendicular to the surface of the MO film using an excitation coil to which a sinusoidal current is applied. The ac magnetic field generated in the film has the form $H_{\rm AC}(\omega {\rm t}) = H_{\rm o}{\rm sin}(\omega {\rm t})$, where ω is the frequency. The addition of $H_{\rm AC}$ to $H_{\rm PM}$, the equilibrium position of the domain wall shifts to where the sum of the two magnetic fields is zero and this causes magnetic domains walls in the MO film to oscillate. The resulting Faraday rotation has the form

$$\Phi_F(\omega t) = V\ell B_o{\rm sin}(\omega t)$$

where V is the Verdet coefficient, ℓ is the path length in the magnetooptic material, B_o is the amplitude of the magnetic field, ω is the frequency, and t is time. This leads to an ac modulated signal detected by the photodetector. As a result, the ac modulated output signal is sensitive to deviations of the reflected light beam path.

III. EXPERIMENT

The components of the new magnetooptic sensor system are: a He–Ne laser, a MO film, an ac excitation coil, two permanent magnets, an analyzer, and a photodetector as shown in Fig. 1. A polarized light beam generated by the He–Ne laser passes through the MO film. The film employed in this experiment was bismuth-doped iron garnet $({\rm Bi,Tm})_3({\rm Fe,Ga})_5{\rm O}_{12}$ with thickness 3 μm, grown on a thin substrate of gadolinium gallium garnet (GGG). The thickness of the GGG substrate was 0.5 mm. The bismuth-doped iron garnet film had a large specific Faraday rotation, $\theta_{\rm F}$ up to 2.3°/μm of thickness. The domain walls in the film are activated by a threshold magnetic field of 0.1–0.3 mT. A 50 Hz frequency ac field $H_{\rm AC}(\omega t)$ was applied to the surface of the MO film using the coil. This caused the domain wall between oppositely magnetized domains to oscillate. Consequently when a sinusoidal ac voltage was applied to the solenoid coil, the signal detected at the photodetector was also sinusoidal.

Two hard ferrite magnets (remanence $B_r = 0.350$ T and coercivity $H_c = 260$ kA/m) with opposite polarity were positioned closed to the MO film as shown in Fig. 1, and these generated a uniform magnetic field gradient within the film. The distance between the two permanent magnets was 15 mm and the distance between sample and the MO sensor was 100 mm. As a result of this field gradient, a two-domain structure with opposite directions of magnetization was formed. The equilibrium position of the domain wall, which varied sinusoidally with time, was at the location where the strengths of the $H_{\rm PM}$ and the ac field, $H_{\rm AC}$ were equal and opposite, that is $H_{\rm PM} + H_{\rm AC} = 0$. When $H_{\rm PM} = 0$ the intensity of light detected by the photodetector was sinusoidal in time, but when a dc field $H_{\rm PM}$ was introduced this caused a distinctive "shoulder" region to occur in the middle of the output voltage range as shown in Fig. 2.

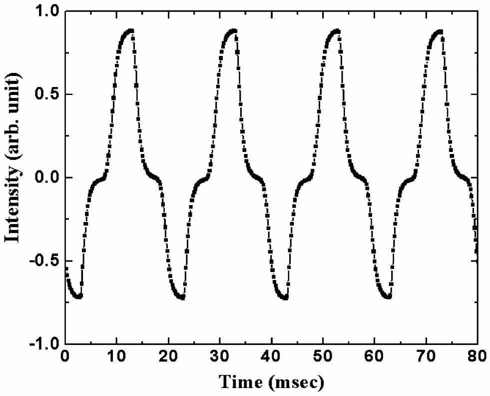

Fig. 2. Intensity of the detected light beam without surface rotation. The waveform consists of a sinusoidal output signal separated by an intermediate "shoulder" region.

The variation in the detected intensity originated from the Faraday rotation occurring when the light beam passed through the magnetooptic garnet film with a linear gradient dc magnetic from two oppositely oriented permanent magnets (which created "up" and "down" domains) and an ac sinusoidal current from an ac excitation solenoid coil (which created an ac oscillation of the domain wall).

When the incident and reflected light beam paths were in the "up" domain, the magnitude of Faraday rotation doubled due to the transmission of light beam twice through the film and the upper output signal occurred. When the incident and reflected light beam paths were in the "down" domain, the magnitude of Faraday rotation doubled as the case for "up" domain, but the direction of Faraday rotation was opposite to that of "up" domain. This led to a lower output signal. The "shoulder" region between the two opposite signals appeared when the incoming light beam path was in one domain and the reflected light beam path was in the other.

Constant background intensity was detected along with the real signals of interest. We subtracted this constant background intensity and set the reference output voltage where Faraday rotations canceled out.

For the purposes of this study, surface deformation was simulated by mounting an aluminum mirror on a rotator providing pure rotational motion of 7×10^{-3} degrees per graduation. Rotations of 0.02° and 0.04° of a sample were made and the intensity of the detected light beam for each rotation was measured.

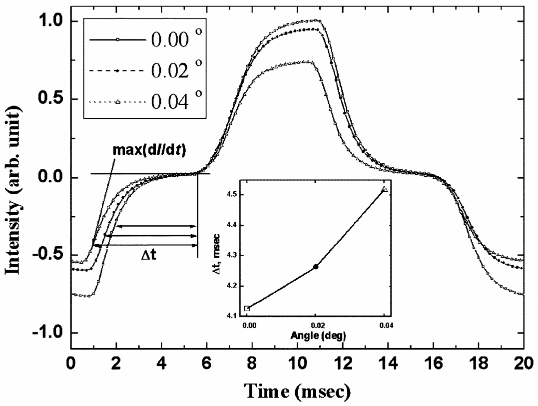

Fig. 3. Measured intensities of the reflected light beam for rotations of the surface of aluminum of 0.00° (solid line), 0.02° (dashed line), and 0.04° (dotted line), respectively. The width of the "shoulder" region changes with the angle of reflection. Changes in the angle of reflection could be caused by surface defects. Inset: Increase of "shoulder width" as the angle of rotation increases.

IV. RESULTS AND DISCUSSION

The intensity of the light detected by the photodetector had the waveform of a distorted sinusoidal output signal as shown in Fig. 2. The upper output signal occurred while the "up" domain moved to the position where it covered both the incident and reflected light beam paths. The lower output signal occurred while the "down" domain covered both the incident and reflected light beam paths. The "shoulder" region between the two opposite signals appeared when the incoming light beam path was in one domain and the reflected light beam path was in the other.

Measured intensities for rotations of the surface of aluminum by 0.00°, 0.02°, and 0.04° are shown in Fig. 3. The solid line is the intensity of the signal without rotation of the sample; the dashed line is the intensity of the detected signal with sample rotation of 0.02°; and the dotted line is the intensity of the signal with sample rotation of 0.04°. We defined the "width" of the shoulder region as a time interval between times at which zero and maximum of the first derivative of the intensity occurred as shown in Fig. 3 with Δt. From the measured data, it was found that a systematic increase of the width of the "shoulder" region occurred as the angle of deflected light beam increased as shown in the inset of Fig. 3. Therefore, measurement of the angle of reflection of the light beam has been converted into measurement of the temporal length of the distinctive "shoulder" region of the signal relative to the rest of the detected signal. A change in the intensity due to off-centered laser beam can alter the magnitude of the measured maximum intensity level, but this change does not provide any pattern useful for surface rotation detection since any background intensity changes could alter the maximum intensity level. Compared to this, the measurement of the width of the "shoulder" region is independent on variations in reflected intensity from the surface of the material and can be made with high accuracy. By measuring the changes of width of the shoulder in the intensity versus time waveform, we can obtain information on surface deformation.

V. CONCLUSION

A new MO sensor technique has been developed which allows for the evaluation of a wide variety of surface deformations for all types of materials: magnetic, nonmagnetic, conducting, and nonconducting materials. This technique remotely detects surface deformation. The modulated ac output signals specifically the width of the distinctive "shoulder" region, were found to be very sensitive to the change in angle of reflected light due to defects in the surface. The technique can also be used to detect internal defects that are not directly visible on the surface by measurement of the associated surface deformation.

ACKNOWLEDGMENT

This work was supported by the National Aeronautical and Space Administration (NASA) under Award NAG-1-02098.

REFERENCES

[1] P. Ripka, *Magnetic Sensors and Magnetometers*. Boston, MA: Artech House, 2001.

[2] J. Y. Lee, S. J. Lee, D. C. Jiles, M. Garton, R. Lopez, and L. Brasche, "Sensitivity analysis of simulations for magnetic particle inspection using the finite element method," *IEEE Trans. Magn.*, vol. 39, no. 6, pp. 3604–3606, Nov. 2003.

[3] W. Lord, S. Nath, Y. K. Shin, and Z. You, "Electromagnetic methods of defect detection," *IEEE Trans. Magn.*, vol. 26, no. 5, pp. 2070–2075, Sep. 1990.

[4] G. S. Park and E. S. Park, "Improvement of the sensor system in magnetic flux leakage-type nondestructive testing," *IEEE Trans. Magn.*, vol. 38, no. 2, pp. 1277–1280, Mar. 2002.

[5] G. L. Fitzpatrick, D. K. Thome, R. L. Skaugset, W. C. L. Shih, and E. Y. C. Shih, "Magneto-optic/eddy current imaging of aging aircraft: A new NDI technique," *Mater. Eval.*, vol. 51, pp. 1402–1407, Dec. 1993.

[6] V. Brechling and F. Spencer, "The validation process as applied to the magneto-optic/eddy current imager," *Mater. Eval.*, vol. 53, pp. 815–818, Jul. 1995.

[7] Y. S. Didosyan, H. Hauser, J. Nicolics, and F. Haberl, "Application of orthoferrites for light spot position measurements," *J. Appl. Phys.*, vol. 87, pp. 7079–7081, May 2000.

[8] Y. S. Didosyan, H. Hauser, J. Nicolics, V. Y. Barash, and P. L. Fulmek, "Magneto-optical current sensor by domain wall motion in orthoferrites," *IEEE Trans. Instrum. Meas.*, vol. 49, pp. 14–18, Feb. 2000.

[9] Y. S. Didosyan, H. Hauser, and G. A. Reider, "Magneto-optic switch based on domain wall motion in orthoferrites," *IEEE Trans. Magn.*, vol. 38, no. 5, pp. 3243–3245, Sep. 2002.

[10] E. Hristoforou and D. Niarchos, "Mechanical sensors based on reentrant flux reversal," *IEEE Trans. Magn.*, vol. 28, no. 5, pp. 2190–2192, Sep. 1992.

[11] Y. S. Didosyan, H. Hauser, H. Wolfmayr, J. Nicolics, and P. L. Fulmek, "Magneto-optical rotational speed sensor," *Sens. Actuators A*, vol. 106, pp. 168–171, Sep. 2003.

[12] Y. S. Didosyan, V. Y. Barash, N. A. Bovarin, H. Hauser, and P. L. Fulmek, "Magnetic field sensor by orthoferrites," *Sens. Actuators A*, vol. 59, pp. 56–60, Apr. 1997.

[13] K. B. Rochford, A. H. Rose, and G. W. Day, "Magneto-optic sensors based on iron garnets," *IEEE Trans. Magn.*, vol. 32, no. 5, pp. 4113–4117, Sep. 1996.

[14] M. Klank, O. Hagedorn, M. Shamonin, and H. Dötsch, "Sensitive magneto-optical sensors for visualization of magnetic fields using garnet films of specific orientations," *J. Appl. Phys.*, vol. 92, pp. 6484–6488, Dec. 2002.

Manuscript received November 16, 2004; revised February 15, 2005.

REFERENCES

1. R.C.O'Handley, *Modern Magnetic Materials Principles and Applications* (John Wiley & Sons, Inc., New York, 2000) Chap. 3-4, 6-7.
2. Barth, T. F. W., and E. Posnjak, Z. Krist. **82**, 325 (1932).
3. Verwey and E. L. Heilman, J. Chem. Phys. **15**, 181 (1947).
4. A.E.Clark, *Ferromagnetic Materials, E.P. Wohlfarth(Ed.), Vol.1*, North-Holland Publishing Co., Amsterdam, (1980)
5. Y. Chen, J. E. Snyder, C. R. Schwichtenberg, K. W. Dennis, R. W. McCallum, and D. C. Jiles, IEEE Trans. Magn. **35**, 3652 (1999).
6. Y. Chen, J. E. Snyder, K. W. Dennis, R. W. McCallum, and D. C. Jiles, J. Appl. Phys. **87**, 5789 (2000).
7. J. A. Paulsen, A. P. Ring, C. C. Lo, J. E. Snyder, and D. C. Jiles, J. Appl. Phys. **97**, 044502 (2005).
8. K. Krieble, T. Schaeffer, J. A. Paulsen, A. P. Ring, C. C. H. Lo, and J. E. Snyder, J. Appl. Phys. **97**, 10F101 (2005).
9. C. C. H. Lo, P. N. Matlage, Y. Melikhov, J. E. Snyder, S. H. Song, and D. C. Jiles, IEEE International Magnetics Conference, San Diego (2006)
10. K. Krieble, C. C. H. Lo, Y. Melikhov, and J. E. Snyder, J. Appl. Phys. **99**, 08M912 (2006).
11. A. Navrotsky and O. J. Kleppa, J. inorg. Nucl. Chem. **29**, 2701 (1967).
12. E. W. Gorter, Philips Res. Rep. **9**, 294 (1954).
13. F. C. Romeijn, Philips Res. Rep. **8**, 304 (1953).
14. W. Heisenberg, Z. Phys. 49, **619** (1928).
15. P. Langevin, Ann. Chim. Phys. **5**, 70 (1905).
16. P. Weiss, J. de Phys. Rad. **6**, 661 (1907).
17. L. Brillouin, J. de Phys. **8**, 74 (1927).

18. A. Arrot, Phys. Rev. **108**, 1394 (1957).
19. F. Bloch, Z. Physik **61**, 206 (1930).
20. E. Ising, Z. Phys. **31**, 253 (1925).
21. J.M. Yeomans, *Statistical Mechanics of Phase Transitions* (Oxford Science Publications, Clarendon Press, Oxford, 1992).
22. L. Onsager, Phys. Rev. **65**, 117 (1944).
23. D. Mermin and H. Wagner, Phys. Rev. Letters **17**, 1133 (1966).
24. N. Akulov, Z. Phys. **57**, 249 (1929).
25. D.C. Jiles, *Introduction to Magnetism and Magnetic Materials* (Second Edition Chapman, & Hall, New York 1998) Chap. 5.
26. H.B. Callen and N. Goldberg, J. Appl. Phys. **36**, 976 (1965).
27. R.J. Hill, J.R. Craig & G.V. Gibbs, Phys. Chem. Miner. **4**, 317 (1979).
28. E. W. Gorter, Philps Res. Rep. **9**, 321 (1954).
29. T. Tsushima, T. Teranishi, and K. Ohta, *Handbook on magnetic substances* (Asakura Publishing Co., Tokyo, 1975)
30. G.A. Sawatzky, F. Woude, and A.H. Morrish, J. Appl. Phys. **39**, 1204 (1968).
31. M. McGuire, R.C. O'Handley, and G. Kalonji, J. Phys. Appl. **65**, 3167 (1989).
32. Y. Yafet and C. Kittel, Phys. Rev. **87**, 290 (1952).
33. Etienne du Tremolet de la Cheisserie, Damien Gignoux, and Michel Schlenker, *Magnetism I-Fundamentals* (Kluwer Academic Publishers Group, 2002) Chap. 7.
34. L. Neel, Ann. de Physiq. **3**, 137 (1948).
35. S. Chikazumi, *Physics of Ferromagnetism*, 2nd ed. (Oxford University Press Inc., New York, 1997) Chap. 7, 19.

36. Alex Goldman, *Modern Ferrite Technology*, 2nd ed. (Springer Science+Business Media, Inc., 2006) Chap. 4.

37. J. A. Dean, *Lange's Handbook of Chemistry*, 16th ed. (McGraw-Hill, New York, 2005)

38. A. R. Denton and N. W. Ashcroft, Phys. Rev. A **43**, 3161 (1991).

39. S. S. Shinde and K. M. Jadhav, Journal of Materials Science Letters 17, 849 (1988).